UNIVERSITY OF CALIFORNIA, SAN DIEGO

Microfluidic Advantage: Novel Techniques for Protein Folding and Oxygen Control in Cell Cultures

A dissertation submitted in partial satisfaction of the
requirements for the degree
Doctor of Philosophy

in

Physics (Biophysics)

by

Mark E. Polinkovsky

Committee in charge:

Professor Alex Groisman, Chair
Professor Terrence Hwa
Professor Patricia Jennings
Professor Judy Kim
Professor David Kleinfeld

2012

The Dissertation of Mark E. Polinkovsky is approved, and it is acceptable in quality and form for publication on microfilm and electronically:

Chair

University of California, San Diego

2012

DEDICATION

This dissertation is dedicated to my parents, Edward and Zhanna. Thank you for always supporting me and showing me that we cannot give up and must always strive to be the very best.

Я Вас люблю

עם ישראל חי

TABLE OF CONTENTS

LIST OF FIGURES

LIST OF TABLES

ACKNOWLEDGEMENTS

The work presented in this dissertation would not have been possible without a great deal of help from many people, whom I would like to thank.

Chief among these is my advisor, Professor Alex Groisman. He not only provided support and guidance in my work, but also helped me to develop my experimental and analytical skills. Whenever I had a question or difficulty with an experiment, Alex had solutions and patient explanations ready. Moreover, Alex is responsible for my continuing enjoyment of experimental science: the lab's projects are invariably interesting and scientifically beneficial.

Working with Dr. Yann Gambin has really been a privilege. His positive attitude is infectious, as is his determination for a project to succeed. Yann's inventiveness and creativity are incredible, and sometimes it seems that experiments succeed due to his will power alone.

Dr. Edgar Gutierrez is a veritable dynamo in the lab. Edgar always found time to help with my work, even in the midst of fabricating and collecting data for multiple other projects. Meanwhile, his shockingly vast knowledge and expertise in microfluidics, materials, and biochemistry saved the day many times.

Professor Ashok Deniz's help has also been instrumental. He warmly welcomed me into his lab at the Scripps Research Institute, and provided the resources and guidance we needed to complete the temperature jump experiment. Whenever I became overconfident and misaligned the single-molecule FRET setup, Ashok was there to fix it.

Dr. Priya Banerjee also deserves credit for the success of the temperature jump project. His contributions resulted in the only time I have seen an experiment work correctly on the first attempt. I also appreciate his tenacity and interest in all aspects of the experiment.

Dr. Matthew Pamenter and Professor Gabriel Haddad of the UCSD Medical School were crucially involved in the mammalian cell culture project. Many mammalian cells were sacrificed in the name of science, and Matt was always prepared to provide me with more of them. Dr. Eugene Tkachenko was also very helpful in experiments with mammalian cell cultures.

I would like to thank the other graduate students in the lab, with whom it has been such a pleasure to work. Everyone has been invariably friendly and positive, and I could not have asked for better co-workers. Dr. Virginia Vandelinder was always happy to discuss and help with any difficulties. Micha Adler has always been very thoughtful and provided wise counsel. Finally, Michael Erickstad has been amazing to work with. His conscientiousness and attention to detail have improved the

experiments we have worked on specifically, and my understanding of science generally.

Other students who deserve mention for their help are Chih-Te Zee, as well as Crystal Moran-Gutierrez and the other members of the Deniz Lab.

Many thanks go to the members of my committee for their patience and encouragement.

I am grateful to my friends for their unquestioning support. They always know how to lift my spirits and it is invariably a relief to be in their presence. Especially, I must acknowledge my roommates throughout graduate school: Daniel Minsky, Pavel Tseytlovskiy, Paul Ricketts, Michael Conry, Timothy Tirrell, and Andrew Kwok. They are heroes for putting up with my silly stories and rants about Moldova.

My relatives have also been very motivational during my time in graduate school. My uncles, aunts, and cousins flattered me with their constant well-wishes and interest in my progress. My grandparents, Sarra and Leonid, have always shown their love for me and I hope that I will continue to make them proud.

Many thanks go to my little sister, Lyuba, for her confidence in me. She has honored me by asking for my help and advice, and has returned the favor many times over.

Finally, I would like again to thank my parents for all their love. Whenever I have needed moral support, they have been close by with a kind word. Their material and financial support has been unwavering, even when it was a sacrifice for them. My father, always quick with a joke or an anecdote, has taught me the importance of a positive attitude, no matter the situation. My mother – who had to work for years to become a physician again in a new land, while raising a family – illustrated for me the power of perseverance. Most notably, my parents have shown me the importance of education and instilled in me the notion that I must do everything with the highest quality. These principles have driven me through all the challenges I have faced, and I can only hope to impart them on future generations.

Chapter 2.1, in full, is a reprint of the journal article "Fine temporal control of the medium gas content and acidity and on-chip generation of series of oxygen concentrations for cell cultures", *Lab on a Chip*, 2009. Polinkovsky, Mark; Gutierrez, Edgar; Levchenko, Andre; and Groisman, Alex. The dissertation author was the first author and a leading contributor of this paper.

Chapter 2.2.2, in full, is a reprint of the "Supplementary Information" from the journal article "Generation of oxygen gradients with

arbitrary shapes in a microfluidic device", *Lab on a Chip*, 2010. Adler, Micha; Polinkovsky, Mark; Gutierrez, Edgar; and Groisman, Alex. The dissertation author was a participating investigator of this paper.

Chapter 2.3, in full, is in preparation for publication as "Precise control of oxygen concentration in 24-well cell culture plates for hypoxia studies", Polinkovsky, Mark*; Pamenter, Matthew*; Haddad, Gabriel; and Groisman, Alex. The dissertation author is a co-first author and a leading contributor to this paper.

Chapter 3, in full, is in preparation for publication as "Novel temperature jump system for studying conformation changes of biological molecules on a microsecond timescale", Polinkovsky, Mark*; Gambin, Yann*; Banerjee, Priya; Erickstad, Michael; Deniz, Ashok; and Groisman, Alex. The dissertation author is a co-first author and a leading contributor to this paper.

VITA

2006	Bachelor of Science, California Institute of Technology
2006 - 2007	Graduate Teaching Assistant, Physics Department, University of California, San Diego
2008	Master of Science in Physics, University of California, San Diego
2007 - 2012	Graduate Research Assistant, Physics Department, University of California, San Diego
2012	Doctor of Philosophy in Physics (Biophysics), University of California, San Diego

PUBLICATIONS

M. Polinkovsky, E. Gutierrez, A. Levchenko, and A. Groisman. "Fine temporal control of the medium gas content and acidity and on-chip generation of series of oxygen concentrations for cell cultures". *Lab on a Chip*, 2009, **9**, 1073-1084.

M. Adler, M. Polinkovsky, E. Gutierrez, and A. Groisman. "Generation of oxygen gradients with arbitrary shapes in a microfluidic device". *Lab on a Chip*, 2010, **10**, 388-391.

ABSTRACT OF THE DISSERTATION

Microfluidic Advantage: Novel Techniques for Protein Folding and Oxygen Control in Cell Cultures

by

Mark E. Polinkovsky

Doctor of Philosophy in Physics (Biophysics)

University of California, San Diego, 2012

Professor Alex Groisman, Chair

The young field of microfluidics has been growing due to its utility in chemical and biological applications. Microfluidic devices can be rapidly and inexpensively fabricated from silicone elastomers, making them ideal for prototyping and subsequent production. Further, the behavior of fluid flows in micrometer-diameter channels can be accurately predicted – due to the properties of laminar flow and purely diffusive mixing – decreasing experimental uncertainties, while allowing access to a wide range of experiments impossible with traditional methods. The projects presented here fall into two separate areas of biophysics, although they are all facilitated by microfluidics.

Chapter 2 deals with the control of the gas content in the medium of cell cultures. This is an important consideration, as the oxygen concentration, [O_2], available to cells has been shown to affect their metabolism, growth, and gene expression. The first project is a microfluidic chemostat supplying nine different [O_2] to bacteria growing in chambers beneath the gas channels. Here, we compared the growth rates of *E. coli* growing at nine different [O_2] simultaneously. Section 2.2 introduces a multi-channel, computer-controlled gas mixer that can provide up to ten arbitrary gas mixtures to a microfluidic device. Finally, Section 2.3 describes gas control strips for use with mammalian cell cultures in standard multiwell culture plates. These gas control strips allow cell culture media in different rows of wells to contain different [O_2].

Chapter 3 describes a novel system to rapidly heat and cool a small volume of solution of biological macromolecules using time-controlled deposition of heat into a small volume with a focused infrared laser beam. By fluorescently labeling the molecules, their conformational changes due to temperature shifts can be observed. This system improves the time resolution of the cooling transition over traditional methods by at least two orders of magnitude, down to one microsecond. Further, the temperature change from the laser heating pulse is several times larger than with other techniques. We used this system to measure the kinetics of fast DNA hairpin folding and unfolding under varying salt concentrations.

Chapter 1: Introduction

Microfluidics, as its name implies, makes use of fluids flowing through micrometer-size channels. At this scale, fluid flows have properties not usually observed at the macroscopic scales to which we are accustomed. However, these properties make microfluidics useful for biological, chemical, and medical applications. These advantageous characteristics include a steady, laminar character of the flow and mixing solely by molecular diffusion, allowing fluid behavior in microfluidic devices to be accurately modeled and precisely controlled. Further, the sample volumes in microfluidic experiments are orders of magnitude smaller than in traditional assays, allowing researchers to use smaller amounts of expensive reagents. Finally, many modern microfluidic devices are easy, fast, and inexpensive to make, allowing assays to be based on single-use, disposable chips instead of large, expensive fluid-handling systems. Even so, microfluidics is a young field and has not yet seen widespread commercial adoption.[1] Part of the reason is the lack of familiarity in the general scientific and engineering communities to its methods and capabilities. Further, microfluidics would require a change in already standardized procedures, making its implementation hard to justify, unless it offers overwhelming advantages. That is, a "killer app" has not been found for microfluidics yet.[1,5] One area where microfluidics

could play a leading role is in the diagnosis of infectious agents in developing countries. This application, in particular, highlights the strengths of microfluidic devices: they are cheap, disposable, provide rapid results, and all without the need for expensive equipment.[1, 2]

Although the commercial success of microfluidics has been limited so far, it has been widely applied in research, as evidenced by the proliferation of microfluidics-themed journals such as *Lab on a Chip, Microfluidics and Nanofluidics,* and *Biomicrofluidics*. Moreover, microfluidics has made many novel experiments possible. For example, in one of our laboratory's collaborations, a detailed two-dimensional histogram of the conformations of the protein *α*-synuclein was obtained in a single experiment, with a small amount of sample (several microliters). Traditional methods would have required countless samples with varying reagent concentrations in the media.[3] Similarly, a microfluidic array was used to screen drug candidates for their effectiveness against the Hepatitis C virus. Again, traditional assays would have required much more protein sample and over a thousand separate experiments to test each compound individually.[4] This illustrates the capabilities of microfluidics – it can be applied to a wide variety of problems, making biophysical experiments simpler, more robust, and more quantitative. To quote a review on the rising influence of microfluidics: "many developers are starting to view

microfluidics as an important enabling technology for a growing number of products and applications – a potentially 'killer idea'."[5]

The work presented here takes the same general approach. Often, our skills in microfluidics and soft materials are complementary to those of biologists and chemists, resulting in successful collaborations in diverse areas. Indeed, the projects to be discussed, although different in scope, have one thing in common – they are facilitated by microfluidics.

1.1: Microfluidic Theory

1.1.1: Flow in Microfluidic Channels

This section generally follows the excellent exposition given in Bruus's *Theoretical Microfluidics*. For a more in-depth treatment of the concepts, the reader is referred to this book.[6]

The properties of microfluidics, so unusual on the macroscopic scale to which we are accustomed, are well-developed mathematically. Only a few (reasonable) assumptions are necessary for successfully calculating the properties of the flow and modeling it.

First, the fluids we work with are considered incompressible. This is true to a large degree for aqueous solutions, except under the most extreme conditions, which we never approach. Even when using compressed gases, as in Chapter 2, the flows in the region of interest behave similarly to incompressible fluids – the resistance of the channels keeps the flow speed low, and the pressure drop is small, ensuring that the gas flows are well-behaved. Starting from mass conservation and restricting the fluid density from changing (the incompressible flow condition), the continuity equation is simply $\nabla \cdot \vec{v} = 0$, where $\vec{v}$ is the flow velocity.

Our second assumption about the fluids is that they are Newtonian. This means that the shear stress and the strain rate are linearly related by

a coefficient of proportionality called viscosity: $\tau = \eta\,(\partial_i v_j + \partial_j v_i)$. Further, the viscosity, η, is taken to be a constant as a function of the forces acting on the fluid, although it can change with temperature and pressure.

Next, we would like to have the equation of motion of the fluid, so that we may calculate the fluid behavior. In its general form, the equation of motion for fluids is known as the Navier-Stokes equation. Because of our two assumptions, this equation simplifies to the following:

$$\rho\,[\partial_t \vec{v} + (\vec{v}\cdot\vec{\nabla})\vec{v}] = -\vec{\nabla}p + \eta\nabla^2\vec{v} \qquad (1\text{-}1)$$

where ρ is the fluid density and p is the pressure exerted on the fluid. We also assume that no external forces (such as gravity, or electromagnetism) are applied to the fluid.

It is possible to make the Navier-Stokes equation dimensionless by expressing all the physical quantities in terms of characteristic scales. We then obtain:

$$\mathrm{Re}\,[\hat{\partial}_t \hat{\vec{v}} + (\hat{\vec{v}}\cdot\hat{\vec{\nabla}})\hat{\vec{v}}] = -\hat{\vec{\nabla}}\,\hat{p} + \hat{\nabla}^2\hat{\vec{v}} \qquad (1\text{-}2)$$

where the caps above the variables denote them as being dimensionless, and *Re* is the famous Reynolds number:

$$\mathrm{Re} \equiv \frac{\rho V_0 L_0}{\eta} \qquad (1\text{-}3)$$

Here, V_0 is the characteristic velocity and L_0 is the characteristic length. These are chosen as the constraints on the system or the order-of-

magnitude estimates of the values. From eq. 1-2, we can see that if $Re >> 1$, the left side of the equation (the convective terms) dominates. In this regime, the fluid can exhibit many non-linear effects (such as turbulence) due to the non-linear term $(\hat{\vec{v}} \cdot \hat{\vec{\nabla}})\hat{\vec{v}}$, which makes flows at high *Re* difficult to simulate and predict.

However, if $Re << 1$, the right side of eq. 1-3 dominates instead. This simplified equation is called the Stokes equation:

$$-\vec{\nabla}p + \eta\nabla^2\vec{v} = 0 \tag{1-4}$$

The regime given by eq. 1-4 is termed viscous flow, where the velocity is driven by pressure, and, as it turns out, is generally characteristic of microfluidic flows. For example, in a large microfluidic channel with relatively fast flow, $L_0 \sim 100$ μm and $V_0 \sim 1$ cm/s, respectively. For water, $\rho = 1000$ kg/m^3, and $\eta \sim 10^{-3}$ Pa·s = 10^{-3} kg/(m·s). This gives $Re \approx 1$, still too small for inertial effects to become significant ($Re \approx 30$). In general, it is usually safe to assume a negligible role for inertia in microfluidic flows, although some of our gas flows have $Re \approx 60$. Still, the flows remain laminar, so the general results hold even in such cases.

The Stokes equation implies that low *Re* flows are driven by pressure differences (or boundary conditions). Our goal becomes to find a solution for laminar, steady-state fluid flow in long channels, as these are

the conditions encountered in microfluidic devices. Such fluid flow is known as Poiseuille flow.

We consider an infinitely long, rectangular pipe oriented along $\hat{x}$, with width w and height h ($w > h$ by convention). Since there is no force along $\hat{y}$ or $\hat{z}$, and consequently no pressure differences along either of these directions, the flow can only be directed along $\hat{x}$. Further, because the pipe is uniform and infinitely long, the velocity cannot be a function of x. (These arguments assume that the flow is laminar, or there would be local flows in $\hat{y}$ and $\hat{z}$). In this case, the left-hand side terms of the Navier-Stokes equation (eq. 1-1) are 0, and it again reduces to the Stokes equation (eq. 1-4). The equation to solve is:

$$\eta[\partial_y^2 + \partial_z^2]v_x(y,z) = \partial_x p(x) \tag{1-5}$$

Since the two sides of eq. 1-5 depend on different variables, but are equal, the gradient of pressure must be a constant along the length (where we choose L to be a characteristic length). Moreover, we have the standard no-slip boundary conditions at the walls of the channel. So, eq. 1-5 becomes:

$$[\partial_y^2 + \partial_z^2]v_x(y,z) = -\frac{\Delta p}{\eta L} \tag{1-6a}$$

$$\text{for } -w/2 < y < w/2,\ 0 < z < h$$

$$v_x(y,z) = 0 \text{ for } y = \pm w/2,\ z=0, \text{ and } z=h \tag{1-6b}$$

Unfortunately, there is no analytical solution, but a solution based on Fourier series can be found:

$$v_x(y,z) = \frac{4h^2\Delta p}{\pi^3 \eta L} \sum_{n,odd}^{\infty} \frac{1}{n^3} \left[1 - \frac{\cosh(n\pi \frac{y}{h})}{\cosh(n\pi \frac{w}{2h})} \right] \sin(n\pi \frac{z}{h}) \qquad (1\text{-}7)$$

From eq. 1-7, we can integrate over y and z to find the volumetric flow rate, Q. Although the exact solution is again a Fourier sum, an approximation exists:

$$Q \approx \frac{h^3 w \Delta p}{12 \eta L} \alpha \text{, where } \alpha = \left[1 - 0.630 \frac{h}{w} \right] \qquad (1\text{-}8)$$

Even when $h = w$, this equation gives an error of 13%, and the error drops sharply thereafter, giving almost exact solutions for even modest aspect ratios. Since microfluidic channels usually have aspect ratios of at least 2-to-1 in width to height, this approximation is very accurate. Eq. 1-8 is useful in allowing us to calculate the flow rate through a channel as a function of pressure difference between its inlet and outlet.

To calculate the flow rate in a microfluidic network, we can develop an analogy with electric circuits. The volumetric flow rate through a channel is akin to a current that flows through a wire. The pressure difference between the ends of the channel driving the flow is comparable to the electric potential difference driving the current. So, we can define a

fluidic resistance for the channel, which is analogous to the electrical resistance in Ohm's Law, $R_e = V / I$:

$$R_f = \frac{\Delta p}{Q} = \frac{12 \eta L}{h^3 w \alpha} \tag{1-9}$$

The rules for calculating the resistances of multiple channels are just as in electric circuits: channels connected in series have additive resistances, while the resistances of parallel channels combine as $R_{tot} = \left(\frac{1}{R_1} + \frac{1}{R_2} + ... \right)^{-1}$.

Notably, the resistance increases linearly with the length of the channel, and, approximately, as the inverse of the cube of the height (the smaller cross-sectional dimension). Therefore, a simple way to reduce the flow rate at a given pressure difference is to make the channels shallower. If the device design constrains the channel height, the channels can instead be made longer, which in microfluidic devices is often accomplished by folding channels into multi-segment serpentine lines. As long as *Re* remains small (so inertial effects can be neglected), the turns in the channel do not affect the laminar character of the flow, although their contribution to the total fluidic resistance is somewhat difficult to calculate. An important caveat regarding these results is that the Poiseuille flow solution assumes an infinite-length channel. For it to be practically applicable, channel lengths must be much larger than their widths.[6]

1.1.2: Diffusion

As we saw in Section 1.1.1, microfluidic flows are essentially non-inertial, laminar, and steady. Therefore, the patterns of flow in the microfluidic channels directly reflect the channel profiles, and if the channel is rectilinear, so is the flow in it. This fact has significant implications for various processes, mixing in flows being the most important. In the macroscopic regime, a paintbrush can be used to mix red and blue watercolor paints into purple. The paint particles suspended in the water are mixed by convection, meaning that the paintbrush actively drives the motion of the water and the paint molecules, rapidly making a uniform mixture. In contrast, when streams of two solutions enter a microfluidic channel with a uniform cross-section from opposite sides, the streams merge and flow side-by-side. For example, two streams of water, colored red and blue and flowing into a common channel, would travel down the channel next to each other with mixing occurring only by the random motion of molecules through the interface between them. This motion is known as diffusion.

Modeled as a random walk, the characteristic time for a molecule to move a distance r is given by the relation:

$$t_{diff} = \frac{r^2}{2nD} \tag{1-10}$$

where n is the number of dimensions in which the diffusion occurs (1, 2, or 3), and D is the diffusion coefficient. In order to ensure good mixing for two side-by-side streams, their residence time in the channel must be several times the t_{diff}, with r equal to half of the channel width. This relation is important, for example, in designing microfluidic devices. The mixing channels need to be long enough, and the flow velocities in them sufficiently low, to provide adequate time for diffusive mixing. Some relevant diffusion coefficients are listed in Table 1-1.

Table 1-1: Diffusion coefficients of selected substances.

Molecules	**Diffusion coefficient (cm^2/s)**
N_2, O_2 in air	≈ 0.2 cm^2/s
N_2, O_2 in water	$\approx 2 \times 10^{-5}$ cm^2/s
N_2, O_2 in PDMS [7]	$\approx 3 \times 10^{-5}$ cm^2/s
Small molecules in water	$\approx (0.5 \text{ to } 1) \times 10^{-5}$ cm^2/s

1.2: Microfluidic Device Design and Fabrication

In order to perform specific functions, microfluidic devices must be designed and fabricated with particular channel layouts. In many cases, the task dictates what depth or width certain channels of the device require. The horizontal dimensions of the device are generally limited to the size of a standard microscope cover slip (24 × 50 mm). Also, the inlet and outlet holes must be located at least 3 mm from the edges and from each other. The final global limit on the device complexity is that channels with a maximum of three different depths can be fabricated reliably on the same device. The channel dimensions are often dictated by other practical issues. Chief among these is to ensure that the desired range of flow rates in the device is achieved with a reasonable range of driving pressures applied between its inlets and outlets. If more resistance is required, serpentine resistance channels may be added, but their placement could be constrained by the permissible footprint of the chip.

Since we prefer to generate the driving pressures, Δp, hydrostatically, our ideal operating range is a Δp of 5 to 27 inches of water, equivalent to 0.2 to 1.0 psi or 1.3 to 7 kPa, although our microfluidic devices can normally withstand pressures of up to 4 psi.

The fabrication process also imposes some design limits on the channel dimensions. Channels, especially very shallow ones ($h < 2$ μm), are

susceptible to collapse when their aspect ratios (w/h) are larger than approximately 20. At the same time, channels with aspect ratios < 2 are prone to breaking during fabrication. When devices have channels of multiple depths, the precision of their mutual alignment is limited by the fabrication tolerances. Specifically, it is difficult to align to better than ±10 μm, and often, with large features, safety margins of at least 20 μm are preferable between channels to prevent their overlap and to ease the removal of unexposed photoresist. On the other hand, if channels of different depths are meant to join, it is important for the photomask features defining them to overlap by at least 10 μm.

The intended application of the device often imposes strict requirements on the channel dimensions and flow rates. For example, in bacterial chemostats (Section 2.1), the feeding capillaries connecting the bacterial culture chambers with the medium flow-through channels need to be shallower than 0.8 μm to prevent bacteria from escaping. At the same time, the culture chambers must be several micrometers deep to provide unrestricted growth to the bacteria for several generations. The width of both of these features must be such that they do not spontaneously collapse. For diffusive mixing of solutes or gases in a channel network (see Section 1.1.2), the mixing channel must be long enough, and the flow rate low enough, for the fluids to spend several diffusion times in the channel,

so that their mixture will be sufficiently homogeneous at the end of its transit through the channel.

Even with all of these considerations, the channel dimensions may not be fully constrained. In this case, channels with depths between 15 and 75 μm, with correspondingly appropriate widths, are the easiest to fabricate. Still, care should be taken to ensure that the driving pressures and flow rates of the solutions through the device are reasonable.

Our laboratory uses several software packages for device design. In general, any vector graphics software can be used, but we prefer Macromedia Freehand, which although obsolete, provides all the necessary functionality with a convenient user interface. A popular alternative is CAD software, such as AutoCAD, but it is often more difficult to use. Another promising package is SolidWorks (Dassault Systemes), which can also be used to create 3-dimensional models of the device. These can be directly imported into COMSOL Multiphysics, the finite element simulation software we use for modeling various physical phenomena in our devices.

Once the device design is finalized, photomasks of the different layers need to be laid out and ordered. The layout is made again in Freehand, and often several different versions of the device are placed together on the same mask. This is done to provide different capabilities or to test various configurations in one batch of microfabricated chips.

Photomasks are usually received from photo plotting companies on large plastic sheets. The limitations for these photomasks is their graininess and the smallest feature sizes that can be reliably plotted, approximately 1-3 μm and 6-20 μm, respectively. If smoother or smaller features are necessary, chrome masks can be ordered, although these have longer lead times and are significantly more expensive.

The main fabrication techniques we use are contact photolithography for creating a master mold and soft lithography for casting the devices with the mold. Contact photolithography, a process borrowed from microchip manufacturing, uses a photomask to selectively expose areas of photoresist to ultraviolet light. First, a silicon wafer is spin-coated with a desired thickness of photoresist. We normally use the SU-8 2000 series of UV-curable epoxies as the photoresists. SU-8 can be applied in thicknesses from approximately 500 nm to hundreds of micrometers (members of our laboratory have had success with ~ 1 mm thick layers). After baking on a hot plate (the "pre-bake"), the wafer with photoresist is put in contact with the photomask and exposed to ultraviolet light through the photomask. After exposure, the wafer is baked again in the "post-bake" to complete the cross-linking of the UV-exposed SU-8. Finally, the unexposed photoresist is developed off the wafer. If the desired master mold has relief features of multiple heights, this process is repeated with SU-8 coatings of increasing thicknesses. The photomasks for

the second and third layers are accurately aligned with respect to the existing pattern of cured SU-8 using a home-built mask aligner. The result is a wafer with a pattern of channels protruding above it that serves as a master mold for the microfluidic devices.

The devices are cast from the mold in a silicone elastomer called polydimethylsiloxane or PDMS. First, the wafer surface is exposed to chlorotrimethylsilane (TMCS) for 2 to 5 minutes to inactivate the surface so PDMS does not stick to it. Then, the two liquid components of the PDMS pre-polymer – the base and the cross-linker – are mixed in a certain proportion. The mixture is quickly poured onto the wafer, degassed to remove bubbles, and baked at 80 °C for one hour. During this time the PDMS solidifies into a flexible silicone rubber and its bottom surface becomes a replica of the SU-8 relief on the wafer. Care must be taken when peeling the PDMS cast off the wafer so that the photoresist relief is not damaged, especially when the relief has low-aspect-ratio features. Once it is safely detached, the PDMS is cut into separate microfluidic chips. Inlet and outlet holes are punched through the PDMS chips with a sharpened Luer stub. Then, the chips are cleaned with ethanol and masking tape. To complete assembly of the microfluidic devices, the PDMS chips are sealed against glass cover slips, which form the bottom of the microfluidic channels. Finally, the devices are left to bake at 80 °C overnight. This casting process of PDMS chips has many variations. Multi-layer devices,

with microchannels in different planes, can be assembled by bonding the PDMS layers together before they completely cure. Also, the PDMS devices can be irreversibly bonded to glass cover slips by exposing both surfaces to air plasma for a few seconds before they are brought into contact, and baking at 80 °C for five minutes afterwards.

Our laboratory has extensively experimented with different commercially available formulations of PDMS. These formulations differ in such properties as viscosity, hardness, tear resistance, opaqueness, and index of refraction. In addition, for a given commercial formulation, the ratio of base to cross-linker can be varied to yield a harder or softer final product, and sometimes, mixtures of two different PDMS formulations are used, similar to alloying metals.

Once the devices are sealed, they can be used for experiments. After an experiment, the glass cover slip can be detached from a PDMS chip if they are not bonded permanently. The PDMS chip can then be cleaned, bonded to a new cover slip, and used again.

The standard formulations of PDMS, from which we cast the microfluidic chips, have several properties important for our experiments. They are transparent in the visible spectrum, allowing bright field illumination of the channels from the top, through the bulk of the chips, and have a very low auto-fluorescence background, making the chips compatible with fluorescence microscopy. Fully cured PDMS is non-toxic

and cell-compatible. Finally, PDMS is porous and approximately 6 times more oxygen-permeable than water. We use this property of PDMS to impose and control the gas content of cell culture media in microchannels by flowing customized gas mixtures through nearby void channels on the same device.

1.3: Standard Experimental Setup

Microfluidic devices are generally built to be used with optical detection techniques. To that end, most of our devices are designed to work on inverted fluorescence microscopes. In our laboratory, we use Nikon TE2000 and TE300 inverted microscopes with high-power light-emitting diode (LED) light sources in modified lamp housings for fluorescence excitation. We use LEDs instead of mercury lamps because their output light power is very stable, varying only by 0.1% over 20 minutes. Also, LEDs have much longer lifetimes and are much cheaper, compared to mercury lamps.

Flexible plastic tubing is inserted into the device inlet and outlet holes to connect microfluidic devices to liquid reservoirs. Usually, these reservoirs, which contain liquids fed to, and drawn off from, the devices, are microcentrifuge tubes closed with PDMS plugs having two holes. A Luer stub is inserted into one hole and the plastic tubing is in the other. A syringe or source of pressurized air (or vacuum) can be connected to the Luer stub to control the flow into or out of the microcentrifuge tube through the plastic tubing. A reservoir feeding a device inlet is usually placed at a designated height above the outlet reservoir to drive the flow in the device by a difference in hydrostatic pressure. The outlet reservoir itself is placed higher than the device to create a positive ambient pressure

in the microchannels, preventing the formation of air bubbles. If a pressure difference > 1 psi is required, additional pressure from compressed air is usually applied to the inlet reservoir. In most cases, this pressure should not exceed 4 psi (28 kPa) or there is a risk of detaching the PDMS chip from the cover slip. If the device features gas channels, the gas sources are connected to the device through flexible plastic tubing, in the same way as the liquid medium reservoirs, with the gas flow through the device controlled by pressures at the gas inlets.

A camera attached to the microscope's side port records the data, using one of several software packages: Unibrain Fire-i, Micro-Manager (UCSF), or National Instruments LabVIEW. For automated control of the bright-field and fluorescence light shutters, the microscope stage, or gas mixer valves, LabVIEW routines are written and used in conjunction with control boxes connected to the control computer's serial or USB port.

To prepare a microfluidic device for an experiment, it needs to be filled with the desired solution. Care must be taken to fill the device completely and remove all air bubbles, which are the bane of microfluidics. Usually, this can be done by pressurizing both the inlet and outlet, forcing air to diffuse out of the channels through the porous PDMS.

1.4: Fluorescence Microscopy

Fluorescence microscopy is a useful optical technique for studying a variety of phenomena. Fluorescence occurs because certain molecules, called fluorophores, absorb light at one wavelength and emit it at a longer wavelength. When an electron of the fluorophore center absorbs an excitation photon, and is promoted to a higher energy level. It then returns to the ground state by one of several pathways, some of which involve releasing a photon. Due to numerous applications of fluorescence microscopy, many different fluorophores have been developed, with a wide variety of properties that make them advantageous for certain applications. For example, a ruthenium-based dye (RTDP) is used in the projects in Chapter 2 to measure oxygen content of aqueous media in a spatially resolved fashion, while Alexa dyes, TMR, and HPTS are used in the project described in Chapter 3 for labeling DNA and for measuring temperature under an infrared laser beam. A recent advance in the application of fluorescence microscopy to life science has been the isolation and improving of "green fluorescent protein" (GFP). The DNA sequence for GFP and other biologically based fluorophores can be coupled to DNA sequences encoding other proteins and expressed in live cells. This technology has made possible a whole range of experiments, from

highlighting cell localization during tissue development to measuring gene expression levels in individual cells.

Optics for fluorescence microscopy have become a standard feature of scientific microscopes. Our microscopes use an epi-fluorescent configuration (Fig. 1-1). The excitation light, derived from a dedicated source (arc lamp or LED in our setup), passes through an excitation filter, is reflected by a dichroic filter toward the objective, and is focused onto the sample. The objective collects a fraction of the fluorescent light, which is emitted by the sample in all directions, and directs it through the same dichroic filter and an emission filter toward the detector (video camera or eyepieces).

When performing an experiment with fluorescence measurements, it is important to choose an excitation light source with the appropriate excitation wavelength and a filter set for optimal signal strength and minimal background. For example, for GFP, the peak excitation is at a wavelength around 488 nm (blue light) and the emission peak is near 510 nm (green). So, a laser, LED, or mercury lamp outputting light between 470 nm and 495 nm can be used. The filter set consists of excitation, dichroic, and emission filters to optimize the illumination power and the efficiency of light collection, while preventing the excitation light from reaching the detector, thus achieving maximum contrast. Consequently, the excitation filter might have a center wavelength of 480 nm and a 20

nm bandwidth (passing the wavelengths in the range from 470 nm to 490 nm). The dichroic filter would reflect wavelengths below 500 nm and transmit wavelength above 500 nm, and the emission filter might have a center wavelength of 535 nm and a bandwidth of 40 nm. This configuration, in separating the filters' transmission bands prevents virtually all of the excitation light from reaching the detector. Moreover, by choosing an appropriately narrow emission filter, the contribution of other background light can be reduced, increasing the signal-to-noise ratio.

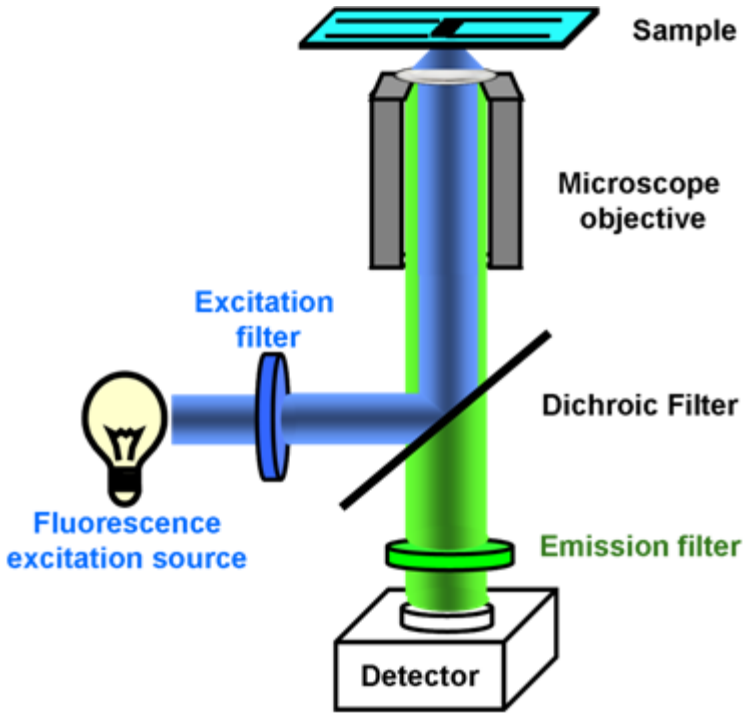

Figure 1-1: Diagram of an epi-fluorescence microscope light path. The fluorescence excitation and emission light both pass through the microscope objective. The dichroic and emission filters remove the excitation light and other background signals from the beam directed toward the detector. The dichroic filter reflects the excitation light toward the objective, while letting the emission light pass through it.

A particular problem in fluorescence experiments, especially fluorescence microscopy, is called photobleaching. Although the process is not well-understood, part of the photobleaching is oxygen-dependent. A fluorophore in its excited state can react with oxygen atoms in its environment and be chemically converted to a non-fluorescent molecule. This loss of fluorescence can significantly affect the measured signal over time and is particularly problematic for single-molecule fluorescence measurements. Therefore, care must be taken to reduce the photobleaching of the sample. The standard precautions are to reduce the intensity of the excitation light or the time of exposure to it.[8] Another method is to de-oxygenate the medium to reduce the possibility of the fluorophores encountering reactive oxygen atoms. Deoxygenation is a standard procedure in single-molecule experiments where a sufficient number of photons must be collected from a small number of fluorophores.[9]

A fluorescence spectroscopy technique that has been increasingly used in biology, biophysics, and biochemistry is Förster Resonance Energy Transfer (FRET). An application of FRET involves exciting a fluorophore, called the donor, and allowing it to transfer the excitation energy to a nearby fluorophore, called the acceptor. Although this energy transfer is non-radiative, the emission spectrum of the donor must overlap with the excitation spectrum of the acceptor, with a higher overlap resulting in a higher probability of energy transfer. One possible FRET pair, as described

in Chapter 3, is Alexa 488 and Cy 5. Alexa 488 is excited by blue light, with a wavelength around 488 nm, and emits in the green, around 520 nm, with a long tail up to approximately 600 nm. This makes it useful for exciting Cy 5, which has appreciable excitation above 550 nm and a maximum emission at ~670 nm.

Importantly, FRET is effective at distances of up to approximately 100 Å, and its probability has a $1/r^6$ dependence. Experimentally, FRET presents itself as a decrease in the donor fluorescence and a corresponding increase in the acceptor fluorescence when the two dyes are brought closer.[8] This property of FRET has made it a powerful tool for testing conformations of biological macromolecules. In a FRET spectroscopy experiment, two fluorescent molecules making a FRET pair, such as Alexa 488 and Cy 5, are chemically attached to two monomers of a biopolymer (two nucleotides of a DNA or RNA molecule or two amino acids of a protein). The monomers are selected such that changes in the conformation of the biopolymer are likely to lead to changes in the distances between the monomers and thus to changes in the spectrum of fluorescence of the FRET pair. Chapter 3 describes how FRET is used to measure the dynamics of DNA hairpin unfolding and refolding due to fast temperature changes.

The ratio of fluorescent signals between the two dyes is termed the FRET efficiency (E_{FRET}) and is the quantity used to report changes in distance between the dyes.

$$E_{FRET} = \frac{I_A}{I_A + \gamma I_D} \tag{1-11}$$

where I_D and I_A are the measured fluorescence intensities of the donor and acceptor, and γ is a correction factor that depends on the quantum yield of the dyes and the detection efficiency of the instrument. If certain properties of the dyes and their relative orientation in the molecule are known, E_{FRET} can be used to measure the distance between the dyes and, correspondingly, between the monomers to which they are attached.[10]

Fluorescence microscopy has been a very important tool for biological and biophysical experiments, judging by its wide-spread applications.[8] The confined volumes in microfluidic devices and advantageous optical properties of the substrates make microfluidics a natural complement to fluorescence microscopy, allowing phenomena to be observed and quantified in higher detail. The simplest advantage of applying microfluidics to FRET studies of biomolecules is in limiting the amount of sample necessary for an experiment. Samples of biomolecules are expensive, and generally available in small amounts. For FRET studies, these samples are dual-labeled with fluorescent dyes, a labor-intensive process that further constrains the yield. Microfluidic devices

also facilitate single-molecule experiments by providing small interrogation volumes that can be observed with high-NA objectives. Other features of microfluidic devices useful to fluorescence microscopy include the ability to scan a wide range of conditions in a single device, quickly expose the sample to a different environment, and deoxygenate the sample on-chip to prevent photobleaching.[9,11]

1.5: Organization of the Dissertation

This dissertation describes the major projects I have been involved in as a graduate student. The work is divided into two areas: controlling the gas content in the medium of cell cultures, the focus of Chapter 2, and using fast temperature jumps to observe transitions in biological molecules, the subject of Chapter 3. My contribution for all the projects was to fabricate and characterize the microfluidic devices, help to set-up and run the experiments, and to perform parts of the data analysis.

Chapter 2 presents a series of projects that use microfluidics to control the gas content in cell culture medium. The amount of oxygen available to cells is known to affect their metabolism, growth rate, and gene expression. The projects are shown in chronological order, since the later techniques depend on lessons from the earlier experiments. Section 2.1 describes a microfluidic chemostat with a gas control layer above it, which allows bacteria to be cultured at different oxygen concentrations in a single microfluidic device. I am the first author of the published paper describing this device. In Section 2.2, a stand-alone, multi-channel gas mixer is presented. I am the second author of the paper where the gas mixer is introduced and I built and characterized the mixer. The gas mixer's development led to the work in Section 2.3, which introduces microfluidic gas control strips for use with mammalian cell cultures in

standard multiwell cell culture plates. This project was done in collaboration with Matthew Pamenter and Gabriel Haddad of the UCSD Medical School. I am the equal-contribution author on the paper being prepared.

Chapter 3 describes a system to perform fast heating and cooling of small volumes of solutions of biological macromolecules in a microfluidic channel, so their conformational transitions triggered by the temperature changes can be observed with a microsecond resolution. This project was done in collaboration with Ashok Deniz's Laboratory at the Scripps Research Institute. I am the equal-contribution author on the paper being prepared.

Chapter 2: Microfluidics for Controlling the Gas Content in Cellular Environments

In the biological laboratory, cells are usually cultured in well-controlled environments, where the media has a certain pH, temperature, and nutrient content, ensuring maximal reproducibility and consistency across different experiments. Another parameter of the cellular environment is its gas content, most importantly the concentration of oxygen in the medium. Because cells may have different metabolic pathways activated at normoxic, hypoxic, and anaerobic conditions, cell cultures at different oxygen concentrations, [O_2], may exhibit differences in growth and gene expression. Moreover, the normal [O_2] around cells in mammalian tissues is 2 to 9%, not the 21% found in the atmosphere. Therefore, even the emulation of native oxygen tension (normoxia) requires the ability to control [O_2] in the mammalian tissue culture medium.

This chapter describes a series of techniques developed in our laboratory to control the gas content of cell culture media and the applications of these techniques to cell culture experiments. We started with a microfluidic device made of PDMS, with an integrated gas mixing network to simultaneously culture bacteria at nine different [O_2] in a single experiment. Later, we built a stand-alone multichannel gas mixer

that can generate up to 10 different gas mixtures from two source gases and supply these mixtures to a variety of devices. More recently, we made gas distribution strips to control the gas content of mammalian cell cultures in multiwell plates. Notably, these gas control methods utilize micro-flow techniques to mix small volumes of gases in precise proportions. Their advantage is in providing multiple mixtures with desired [O_2] from just two source gases: air and N_2.

2.1: Gas Control in the Medium of Bacterial Cultures in a Microfluidic Chemostat

Abstract

We describe the design, operation, and applications of two microfluidic devices that generate series of concentrations of oxygen, [O_2], by on-chip gas mixing. Both devices are made of polydimethylsiloxane (PDMS) and have two layers of channels, the flow layer and the gas layer. By using in-situ measurements of [O_2] with an oxygen-sensitive fluorescent dye, we show that gas diffusion through PDMS leads to equilibration of [O_2] in an aqueous solution in the flow layer with [O_2] in a gas injected into the gas layer on a time scale of ~1 sec. Injection of carbon dioxide into the gas layer causes the pH in the flow layer to drop within ~ 0.5 sec. Gas-mixing channel networks of both devices generate series of 9 gas mixtures with different [O_2] from two gases fed to the inlets, thus creating regions with 9 different [O_2] in the flow layer. The first device generates nitrogen-oxygen mixtures with [O_2] varying linearly between 0 and 100%. The second device generates nitrogen-air mixtures with [O_2] varying exponentially between 0 and 20.9%. The flow layers of the devices are designed for culturing bacteria in semi-permeable microchambers, and the second device is used to measure growth curves of *E. coli* colonies at 9 different [O_2] in a single experiment. The cell division rates at [O_2] of 0,

0.2, and 0.5% are found to be significantly different, further validating the capacity of the device to set [O_2] in the flow layer with high precision and resolution. The degree of control of [O_2] achieved in the devices and the robustness with respect to oxygen consumption due to respiration would be difficult to match in a traditional large-scale culture. The proposed devices and technology can be used in research on bacteria and yeast under microaerobic conditions and on mammalian cells under hypoxia.

Introduction

Live cells can be exquisitely sensitive to the gas content of the medium, as they depend on consuming oxygen and other gases for survival and appropriate function. Therefore, to avoid misregulation of cell homeostasis, growth, and death due to low oxygen content in the medium (hypoxia) in cultures of mammalian cells and aerobic bacteria, it is important to continually replenish oxygen and to maintain its concentration in the medium at a sufficiently high level. In contrast, the presence of oxygen in the medium can be harmful or even lethal for anaerobic organisms. Appropriate maintenance of a cell culture may also require provisions for evacuation of gases produced as a result of cell metabolism or for maintaining an elevated level of CO_2 in the medium. Mammalian cells, for instance, are often cultured in media saturated with a mixture of air and 5% CO_2 in specialized incubators.

There is wide variation in the adaptation of organisms to different concentrations of oxygen, [O_2], found in terrestrial environments. In addition to obligate aerobes and anaerobes, there are microaerophilic organisms, which are most comfortable at [O_2] lower than the 21% found in the atmosphere. Moreover, many life forms, including two of the commonly used single cell model organisms, *Escherichia coli* and Baker's yeast, *Saccharomyces cerevisiae*, are facultative anaerobes. They can switch between aerobic and anaerobic metabolism depending on the nutrient concentrations (*i.e.*, the presence of carbon sources in the medium) and [O_2] in the cell microenvironment. Aerobic respiration is generally more efficient, but requires the more extensive metabolic apparatus of the Krebs cycle, and is thus more 'costly' for the cell. The switch between aerobic and anaerobic modes of metabolism is therefore tightly controlled. High-throughput studies of gene expression profiles indicated that the expression of dozens of *E. coli* operons is switched on or off by the aerobic shift.[1] The extensive re-wiring of the gene regulation network implies that the global regulators sense oxygen levels independently and that the sensing can lead to a cell decision that precisely evaluates the cost to benefit ratio of the potential metabolic and gene transcription switch.[2] These precise sensing capabilities, potentially coupled with sensing of other medium conditions, can allow cells to perform complex 'computation' of its gene expression profile and ensuing functional response.[3]

Because of the multitude of regulators and sensing mechanisms involved, the transition between aerobic and anaerobic metabolism and gene expression patterns in facultative anaerobes is likely to occur over an extended range of [O_2]. Therefore, a detailed quantitative study of the transition would require setting a desired [O_2] in the medium and maintaining it with a sufficient degree of accuracy. By Henry's law, when a liquid is in equilibrium with a gas mixture, the concentrations of gases in the liquid is proportional to their partial pressures (and molar concentrations) in the mixture. Therefore, a standard method of setting the gas content of a growth medium is the perfusion (bubbling) of the medium with a gas mixture of the desired composition. The bubbling is often combined with agitation of the medium to ensure its efficient exposure to gas in the mixture.

This simple method is appropriate for culturing cells in well-aerated ([O_2] = 20.9% as in the air) or anaerobic conditions ([O_2] = 0), with the medium bubbled through with atmospheric air or a non-reactive gas (*e.g.*, argon or nitrogen), respectively. However, the preparation of customized gas mixtures with different [O_2] and accurate monitoring of [O_2] in them, as required for a study of the aerobic-anaerobic transition, is a more difficult task. Whereas certified O_2/N_2 mixtures with a broad range of [O_2] are available commercially, low levels of [O_2] (< 1%), at which some components of the anaerobic machinery may be activated, present an

additional technical challenge. The actual [O_2] in the medium is always lower than [O_2] in the gas mixture because cellular respiration leads to consumption of oxygen in the medium. If the target value of [O_2] is low, the respiration may lead to rapid depletion of oxygen in the medium, thus making the difference between [O_2] in the gas and medium unacceptably large. In theory, a nearly uniform [O_2] in the medium can be achieved by sufficiently fast bubbling and agitation. For practical cell cultures in a chemostat or a flask, however, high rates of gas bubbling may be costly, excessive rates of agitation may cause cell rupture, and the local levels of [O_2] may be difficult to monitor. Therefore, it is difficult to ensure that [O_2] is sufficiently uniform everywhere, especially near walls and in the corners, where the agitating flow is relatively slow and where cells may accumulate, reaching particularly high density.

Microfluidic devices made of polydimethylsiloxane (PDMS) were applied previously to culturing bacteria and yeast under thermostatic and chemostatic (constant medium content) conditions.[4,5] The microfluidic chemostat did not have any specific provisions for efficiently supplying oxygen to growing cell colonies or for monitoring of [O_2] in the medium and relied on the high porosity and gas permeability of PDMS.[4] The diffusivity of O_2 in PDMS was reported at 3.4×10^{-5} cm^2/s versus 2×10^{-5} cm^2/s in water,[6] and the O_2 solubility in PDMS (effective porosity of PDMS) was reported at 0.18. Therefore, when at equilibrium with pure oxygen at 1

atm, the concentration of O_2 in PDMS is 0.18/22.4 M = 8.04 mM, which is ~6 times higher that the concentration of O_2 in water at the same conditions (1.3 mM at 25 °C). The efficiency of the diffusive gas exchange through a PDMS layer increases as the layer becomes thinner. Gas-permeable PDMS membranes have been used to study the rate of respiration of *E. coli* [7] and to build fuel cells [8] and an oxygen sensor.[9] Thin PDMS membranes can be easily incorporated in monolith PDMS devices with two layers of microchannels.[10] Two-layer PDMS devices have been used for exchanging the gas content of an aqueous solution in one layer by flow of a gas through the other layer.[11] Multi-layer PDMS devices with some of the channel layers perfused by oxygen have been applied for culturing hepatocytes.[12]

The small depth of microchannels and relatively high diffusivity of O_2 in water result in short diffusive mixing times (~1 s for 50 μm deep channels), making [O_2] nearly uniform along the vertical direction. Therefore, the local level of [O_2] can be accurately measured using a film of an oxygen -sensitive luminescent dye at the bottom of the channels[11] or a fluorescent dye dissolved in the liquid in the channels.[13,14] The fluorescence of ruthenium tris(2,2′-bipyridyl) dichloride hexahydrate (RTDP) is quenched by oxygen, such that the intensity of fluorescence decreases as [O_2] increases. Consequently, it was used to monitor the rate of respiration of cells in culture.[14]

The laminar character of flow and small channel diameters in microfluidic devices combined with the high diffusivity of molecules in the gas phase (four orders of magnitude higher for oxygen in air than in water) make it possible to mix gases in a controlled and efficient way and to create [O_2] gradients in the gas phase.[15] The techniques of microfluidic mixing in liquid phase enable on-chip generation of solutions with concentrations following linear, polynomial,[16] or exponential series.[17] The series and gradients of concentrations have been applied to culturing cells under different medium conditions on the same chip[18] and to studies of chemotaxis.[19,20]

Here we present two microfluidic devices (Fig. 2-1), each of which is made of two layers of PDMS and has two layers of channels, the flow layer and the gas layer. In each device, the flow layer channel network is a modification of the microfluidic chemostat,[4] and the gas layer has a gas-mixing channel network generating a series of nine O_2/N_2 mixtures. The values of [O_2] in the mixtures vary linearly in device 1 and exponentially in device 2. Molecular diffusion across thin PDMS membranes separating the two layers equilibrates the O_2 content of aqueous solutions in the flow layer (monitored in-situ by measuring the fluorescence of RTDP) with the on-chip generated gas mixtures in the gas layer. We use device 2 to study cultures of *E. coli* in microchambers with [O_2] varying exponentially between 0% (pure N_2) and 20.9% (air) at room temperature. We find that

the dependence of the *E. coli* division rate on [O_2] has a sigmoidal shape. Importantly, we observe a significant difference in the growth rates between colonies at [O_2] = 0, 0.2%, and 0.5%. We argue that in addition to its capacities to generate a range of gas mixtures and to enable testing cellular behavior in a range of [O_2] in a single experiment, the proposed technology offers a degree of control of [O_2] that would be difficult to match in a flask or conventional chemostat. We also show that the same devices can be used to change the O_2 content of an aqueous solution in a flow channel on a scale of 0.8 sec and to reduce the pH of a buffered solution by 2.5 points within ~0.5 sec by injecting CO_2 into the gas channels.

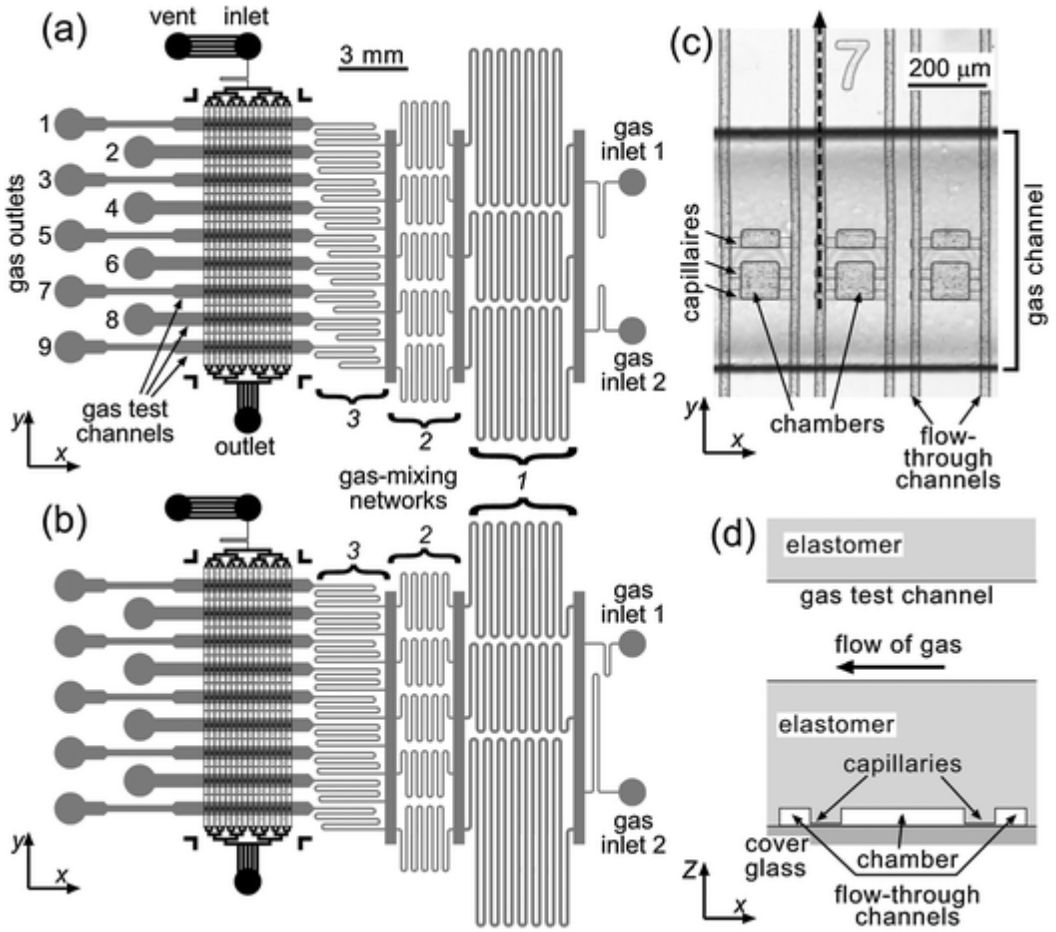

Figure 2-1: Microfluidic devices. (a) and (b) Drawings of the devices 1 and 2, respectively. Flow channels are shown in black and gas channels are shown in semi-transparent gray. The functional region of a device is the area where the flow and gas channels overlap. The gas test channels are numbered the same as their outlets, 1–9 from top to bottom. Three stages of the gas mixing networks are labeled 1–3 in italic. (c) A micrograph of a fragment of the functional region of the device, showing gas test channel 1 with three sets of growth chambers under it (three nodes of the growth chamber grid with 100 × 100 and 100 × 50 µm chambers, both 6 µm deep), each flanked by two 25 µm wide, 6 µm deep flow-through channels. 0.7 µm deep capillaries connect the chambers and channels. The dashed line indicates the line along which the distribution of fluorescence in a flow-through channel was measured (*cf.* Fig. 2-3 and Fig. 2-8). (d) Schematic drawing of a fragment of the *xz*-cross-section of the functional region of a device, showing channels in the two layers of the device. (*x*- and *z*-directions, as well as the depths of flow and gas channels are not to scale).

Experimental

Design and fabrication of microfluidic devices

The two microfluidic devices used in the project share the same general layout (Fig. 2-1). They are made of two layers of PDMS and have two layers of channels: a flow layer for liquids and cell cultures and a gas layer for gas mixtures. The flow channel network is the same in devices 1 and 2, whereas the gas channel networks are different and are designed to generate a linear and an exponential series of O_2 concentrations, respectively. The flow channel network is a modified version of the microfluidic chemostat introduced in Ref. 4. It has an inlet, an outlet, a vent, and channels of two depths, 6 and 0.7 μm (Fig. 2-1). The vent, which is connected to the inlet by low resistance channels, was added for fast exchange of solution in the inlet well and was normally blocked. The functional region of the flow channel network is an area where it overlaps with the gas channel network. It is an array of 32 parallel 25 μm wide flow-through channels (vertical strips in Fig. 2-1 a–c) and 288 growth chambers (Fig. 2-1 c). The channels and growth chambers are 6 μm deep. The growth chambers are arranged in a 16 × 9 grid in the *xy*-plane with 240 and 1200 μm steps along the *x*- and *y*-directions, respectively, (Fig. 2-1 a–c) with a 100 × 100 μm and a 100 × 50 μm chamber ($x \times y$ dimensions) in each node of the grid (Fig. 2-1 c). Each of the 16 rows of chambers along the *y*-axis is flanked by two dedicated flow-through channels, and each of

the 9 rows along the *x*-axis is situated under a specific gas test channel (Fig. 2-1 a–d). The gas test channels are all 600 µm wide with 600 µm wide partitions (Fig. 2-1), and the edges of the growth chambers are at distances of >200 µm from the edges of the gas test channels (Fig. 2-1 c). The gas channels are separated from the flow channels by a 50 µm thick layer of PDMS (Fig. 2-1 d).

The growth chambers are connected to the flow-through channels by 0.7 µm deep 25 × 25 µm capillaries (two and one on each side of the 100 × 100 and 100 × 50 µm chambers, respectively; Fig. 2-1 c, d) that are normally impassable for *E. coli* cells but enable efficient diffusive exchange of nutrients and metabolites between the channels and growth chambers.[4] Therefore, continuous perfusion of the flow-through channels with fresh medium, which is fed into the inlet and drawn off from the outlet, maintains the medium in the chambers nearly identical to the medium in the channels.[4] To load *E. coli* cells into the chambers, pressure at both the inlet and outlet is raised causing the capillaries to bulge up and their depth to increase to >1.5 µm and making them passable for cells.[4]

The gas channel network of each of the devices has 150 µm deep channels with two inlets (gas inlets 1 and 2 in Fig. 2-1 a, b) and 9 outlets and consists of two parts, a gas-mixing network and an array of 9 parallel gas test channels (also called “gas channels” further in the text) in the functional area of the device. The purpose of the gas-mixing network is to

generate a series of 9 different gas mixtures from two gases fed to the gas inlets and to direct these mixtures to the gas test channels (Fig. 2-1 a, b). The gas-mixing networks of both devices are of the type introduced in Ref. 17 (called "gradient-making network" in Ref. 17) and consist of long serpentine channels (intended for mixing of gases by diffusion) and wide redistribution channels (called horizontal channels in Ref. 17), which are arranged in three separate stages of mixing (labeled in italic as 1–3 in Fig. 2-1 a, b). Mixing stages 1, 2, and 3 have, respectively, 3, 5, and 9 serpentine channels of non-equal lengths. The serpentine channels of stages 2 and 3 are 100 μm wide, and the serpentine channels of stage 1 are 150 μm wide. The lengths of the shortest serpentine channels of the three stages are chosen to provide nearly equal ratios of the gas residence times (channel length divided by the gas flow velocity) to the diffusive mixing times (channel width squared divided by the gas diffusivity).

Device 1 used pure N_2 and pure O_2 fed to gas inlets 1 and 2, respectively, to generate a series of O_2/N_2 mixtures with $[O_2]$ varying linearly between 0 to 100% in the gas test channels 1–9. The viscosity of O_2 is ~16% higher than the viscosity of N_2, and the viscosity of O_2/N_2 mixtures is a linear function of $[O_2]$.[21] Therefore, to account for the variations in viscosity between O_2/N_2 mixtures, the design rules stated in Ref. 17 were modified for both gas-mixing networks by dividing the calculated lengths of the serpentine channels by factors of 1 +

0.16[O_2]/100%, where [O_2] are the intended concentrations of O_2 in the respective channels. The gas-mixing network of device 2 was designed to generate an exponential series of [O_2],[17,20] with the fraction of O_2 in the gas mixtures varying by a factor of $3^{½}$ between consecutive test channels and spanning a range from 1 to 81 in relative units, when [O_2] in gas inlet 2 was 81 times higher than in gas inlet 1. In practice, however, gas inlet 1 was fed with pure N_2 ([O_2] = 0), thus shifting the exponential series of concentrations by 1 in the relative units, with [O_2] = 0 in test channel 1 and [O_2] in channel n equal to $(3^{(n-1)/2} - 1)/(81 - 1)$ parts of [O_2] in the gas fed to gas inlet 2. (Because $(3^{(9-1)/2} - 1)/(81 - 1) = 1$, [$O_2$] in gas test channel 9 is always the same as in gas inlet 2.) The gas-mixing network in device 2 was specifically designed to be fed with N_2 and air, generating gas mixtures with [O_2] = 0, 0.2, 0.5, 1.1, 2.1, 3.8, 6.8, 12.1, and 20.9% in the gas test channels 1–9, respectively. Importantly, because of the non-linear variation of [O_2] with the gas test channel number in device 2, the step in [O_2] was substantially reduced near 0, enabling an increased resolution in the microaerobic regime.

The devices were fabricated using two separate master molds, silicon wafers with rectangular relief on them made by SU8 photolithography, as described in detail elsewhere.[4] The mold with the flow channel relief was spin-coated with a 50 μm layer of PDMS pre-polymer (13:1 mixture of base and curing agent of Sylgard 184 by Dow

Corning), which was partially cured by 30 min baking in an 80 °C oven. The gas layer mold was used to cast ~4 mm thick chips of PDMS (7:1 mixture of Sylgard 184, partially cured by 30 min baking in an 80 °C oven). After the inlet and outlet holes were punched in the chips (circles in Fig. 2-1 a, b), the chips were placed on top of the 50 µm layer of PDMS on the flow layer mold in alignment with the flow channels. The two PDMS layers were bonded and fully cured by 3 hours baking in the oven. The monolith two-layer chips were separated from the mold, and the flow layer port holes were punched in the chips. To complete the microfluidic devices, the chips were reversibly bonded to #1.5 microscope cover glasses by overnight baking in an 80 °C oven.

Reagents and cells

Tris(2,2′-bipyridyl) ruthenium(II) dichloride hexahydrate (RTDP), Tween 20, and fluorescein-isothiocyanate were obtained from Sigma. The *E. coli* strain used in the study was described elsewhere.[22] In brief, a truncated quorum sensing *lux* operon from *V. fischeri* was expressed in *E. coli* to track the multigenerational colony growth. An *Eco*RI-*Kpn*I fragment containing *luxR*, the *lux*box, and *lux*I promoter region was inserted into the MCS of pPROBE′-*gfp*-tagless vector to create pJWP01S. This construct was used to transform *E. coli* strain MG1655. The culture (growth) medium both in test tubes and microfluidic devices was LB broth with 50

μg/mL kanamycin and 10 nM of *V. fischeri* specific autoinducer, N-3-oxo-hexanoyl homoserine lactone (HSL). The addition of 10 nM of autoinducer to the growth medium causes overexpression of the *gfp*-tagless reporter.[23] Before the on-chip experiments, the *E. coli* strain was cultured overnight at 35 °C to an OD_{600} of 1.0–1.5.

Setup and procedure

The liquids fed into and drawn off from the flow inlet and flow outlet of a device were kept in modified 1 cc plastic syringes attached to stages sliding on a vertical rail. The flow through the device was driven by a combination of hydrostatic pressure (due to differences in the syringe elevations) and regulated pressure of compressed air.[4] To fill the growth chambers of the device with a liquid, the flow-through channels were filled with a 0.5% solution of Tween 20 (fed from the inlet), and the inlet and outlet were both pressurized at ~0.7 psi. After no air was left in the chambers, the device was perfused for 15 min with 0.1% solution of BSA in a phosphate buffer to purge Tween 20 and to make the surfaces non-sticky for cells. To load *E. coli* cells into the growth chambers, the device was filled from the outlet with an *E. coli* culture grown overnight, and the inlet and outlet were both pressurized at ~1.5 psi (with somewhat higher pressure at the outlet) to make the capillaries passable for cells. Once there were enough cells in chambers, the outlet was depressurized and

cells were purged from the flow-through channels by 15 min perfusion from the inlet driven by a pressure of 0.7 psi. After that, a syringe with the growth medium was connected to the outlet, with the level of the medium set at ~2″ above the device level. The inlet syringe was raised to a higher level to provide a differential pressure of 0.5 psi for continuous perfusion of the flow-through channels with fresh growth medium.

The pressure of compressed air, oxygen, and nitrogen, fed to the gas inlets of the devices, was adjusted by two Porter pressure regulators (8310ANBF10, range 0–10 psi) and measured by a Heise digital pressure indicator with an accuracy of 0.015 psi. To prevent the clogging of gas channels with dust, inline gas filters were placed upstream of the pressure regulators. [O_2] in gas mixtures emerging from the gas outlets (Fig. 2-1 a,b) was sampled off-chip (one outlet at a time) using a commercial oxygen analyzer, MAXO_2 by Maxtec, with a nominal precision of 1% of [O_2]. Because of the low volumetric flow rate of the incoming gas mixtures (~2 mL/min), to ensure reliable [O_2] measurements with a minimal response time, the oxygen sensor of the analyzer (MAX-250E by Maxtec) was equipped with a specially made receptacle that had a low internal volume (0.5 mL) and effectively isolated the sensor from the ambient air. The sensor was connected to the gas outlets through a ~10 cm line of Tygon tubing (ID = 1/16″) and a short piece of hypodermic tubing, which was inserted into the gas outlets.

The experiments with *E. coli* and measurements of fluorescence in the microchannels were done on a Nikon TE300 inverted fluorescence microscope. For measurements of RTDP and FITC fluorescence, we used Sony XCD-X900 and Basler A102f IEEE 1394 cameras. GFP fluorescence of *E. coli* was recorded with a CoolSnap HQ cooled camera. For stable fluorescence illumination, we used a modified Nikon mercury lamphouse with the mercury lamp replaced by an LED mounted on a small cooling fan. The LEDs used for measurements of fluorescence of RTDP and FITC were Luxeon V royal-blue and Luxeon V cyan (LXHL-LR5C and LXHL-LE5C by Lumiled), respectively, with the central wave lengths of 455 and 505 nm, respectively, and with maximal light powers of 700 mW and 160 lumens (at a current of 700 mA). Both LEDs were powered by a stabilized HP power supply, and the current through both LEDs was set at 650 mA and continuously monitored with a 6.5 digit multimeter, Fluke 8500A. By directing the light from the royal-blue LED onto the CCD array of a 10 bit digital camera, we found that the power of light emitted by the LED varies by <0.1% within 20 min. The filter cube used for RTDP fluorescence contained a 450/50 nm excitation filter, a 490 nm dichroic splitter and a 530 nm long-pass filter as the emission filter. The filter cube used for FITC fluorescence contained a 500/20 nm excitation filter, 520 nm dichroic splitter, and 550/50 nm emission filter. For the visualization of *E. coli* GFP fluorescence, we used the royal-blue LED and a standard GFP filter cube.

Results

To obtain the local values of $[O_2]$ in the flow channels of a device, we filled it with a solution of RTDP and measured its fluorescence. Oxygen is a quencher of RTDP fluorescence. The intensity of fluorescence of RTDP molecules in the presence of oxygen, I, is reduced compared to the intensity without oxygen, I_0, according to the Stern–Volmer equation, $I_0/I = 1 + K_q \times [O_2]$, where K_q is a quenching constant. To avoid possible confusion with the intensity of fluorescence recorded by our microscopy setup, in what follows, the molecular fluorescence intensities entering the Stern–Volmer equation will be called fluorescent yields. According to the Stern–Volmer equation, $[O_2]$ can be evaluated from measurements of the fluorescent yields as $[O_2] = (I_0/I - 1)/K_q$. The value of K_q can be obtained by comparing the fluorescence of the RTDP solution when it is saturated with a chemically inert gas, such as N_2, and when it is saturated with O_2 (in equilibrium with pure O_2). Because our measurements were always performed at atmospheric pressure and room temperature, with $[O_2]$ in a saturated solution remaining nearly constant (at ~1.3 mM), it was convenient to normalize $[O_2]$ to its saturation value. With this normalization, the quenching constant, K_q, became dimensionless and was obtained as $K_q = I_0/I_{100} - 1$, where I_{100} is the fluorescent yield in a solution saturated with O_2. We note, however, that K_q defined this way was temperature dependent and was expected to decrease by ~2% per 1 °C

near room temperature, because the solubility of O_2 in water decreases by ~2% when the temperature increases by 1 °C. In addition, because of variability of the values of K_q for RTDP reported in the literature[14,24,25] and because of possible dependence of the fluorescence lifetime and K_q on pH, temperature and on the concentration of ions in the solution,[26] the value of K_q for the system had to be found experimentally. The task of our first set of experiments was to check whether the oxygen content of the medium in flow channels is at equilibrium with the gas flowing through gas channels.

Equilibration between the O_2 content in gas and flow channels

To test the equilibrium between the O_2 content in the RTDP solution in flow channels and the gas in the gas channels, each of the gas inlets in device 1 was connected to a source of compressed N_2 and a source of compressed O_2, both set at a pressure of 5.00 psi, through a 3-way solenoid valve that was controlled by a home-made driver. The valves were switched between three different states: (1) ON/ON, with both gas inlets fed with O_2 (thus flooding the entire gas channel network with O_2); (2) OFF/OFF, with both gas inlets fed with N_2 (N_2 in the entire gas channel network); and (3) OFF/ON, with the gas composition in the gas channels varying from pure O_2 to pure N_2 along the positive *y*-axis direction (Fig. 2-1 a). We determined the rates of flow through the gas outlets in state 3 by measuring the rate of displacement of water from a graduated cylinder.

The flow rates were all ~30 µL/s, corresponding to a flow rate of $Q \approx 135$ µL/s through each of the inlets. The flow rate through the central serpentine channel of the 1st mixing stage (56 mm long with 150 × 150 µm cross-section), was estimated as ~110 µL/s, corresponding to a mean velocity of ~5 m/s and a passage time of ~11 ms. This passage time was ~ 10 time longer than the diffusive mixing time, $w^2/D = 1.1$ ms ($D \approx 0.2$ cm^2/s is the diffusion coefficient for N_2/O_2 mixtures and w is the channel width), indicating that N_2 and O_2 were completely mixed after passing through this channel as well as through other serpentine channels of the gas-mixing network.[17]

The Reynolds number in the gas flow was calculated as $Re = Q\rho/(h_g\eta)$, where $\rho = 1.25$ kg/m^3 and $\eta = 1.8 \times 10^{-5}$ Pa s are the density and viscosity of N_2, and $h_g = 150$ µm is the channel height. Re had its highest value of ~60 in the 100 × 150 µm channels connected to the inlets. At this relatively low value of Re, the flow was expected to be laminar and stable, except for possible Dean vortices in curved segments of the channels. The volume of the gas between a solenoid valve and the test area of the device was <20 µL (most of it in the valve and the tubing connecting the valve with the device inlet). Therefore, the characteristic time of exchange of the gas content in the test area was expected to be <0.15 s.

The flow channels of the device were filled with a 250 ppm (by weight) solution of RTDP in a pH 7.5, 10 mM phosphate buffer. The

solution was driven through the flow channels of the device by applying various differential pressures between the inlet and outlet. The maximal flow velocity in 25 μm wide flow-through channels, which was measured by tracking fluorescent beads, had a linear dependence on the applied differential pressure (not shown) with a slope of 460 μm/s per 1 psi, corresponding a slope of 260 μm/s per 1 psi in mean flow velocity. The intensity of fluorescence of RTDP in the flow channels was measured using an epi-fluorescence video microscopy setup. Therefore, in addition to the fluorescence yield, *I*, the signal recorded by the camera in the setup was proportional to the local depth of the flow channels. Because the flow channels of the device were separated from the gas channels by a relatively thin layer of PDMS (50 μm), the depth of the flow channels was sensitive to variations in pressure in the gas and flow layers. To minimize the measurement errors resulting from uncontrolled variations of the flow channel depths, the fluorescence was measured in 25 μm wide flow-through channels, whose depth had substantially smaller pressure sensitivity than that of the 100 μm wide chambers. The local intensity of fluorescence of RTDP was calculated by averaging the values of pixels corresponding to the central ~10 μm of the channel width and subtracting the background, which was sampled at ~50 μm from the channel in an area without microchannels or sources of fluorescence.

When the two solenoid valves were simultaneously switched off or on, changing the gas fed to both inlets from O_2 to N_2 or back (both at 5.00 psi), the intensity of fluorescence averaged over a 200 μm long internal region (y-axis extension) of a flow-through channel under gas test channel 1 changed by a factor of 3.37 within ~4 sec (Fig. 2-2 a). Because the flow-through channel depth was expected to remain unchanged, it was assumed that the ratio of fluorescence yields of RTDP, I/I_0, was the same as the measured ratio of fluorescent intensities. Following the Stern–Volmer equation $[O_2] = (I_0/I - 1)/K_q$, we plotted the dependences of $I_0/I - 1$ on time, t, after the switching from O_2 to N_2 and from N_2 to O_2 (Fig. 2-2 b). The two dependences were well fitted by functions $a \exp(-(t - t_1)/\tau)$ and $a[1 - \exp(-(t - t_2)/\tau)]$, respectively, with $a = 2.37$ (putative value for K_q) and $\tau = 0.79$ sec, indicating that the oxygen exchange occurred as an exponential decay with a characteristic time $\tau = 0.79$ sec. (The value of K_q is somewhat higher than the values of ~2.25 measured in most other tests, most likely because of a relatively low temperature in the room during this test.)

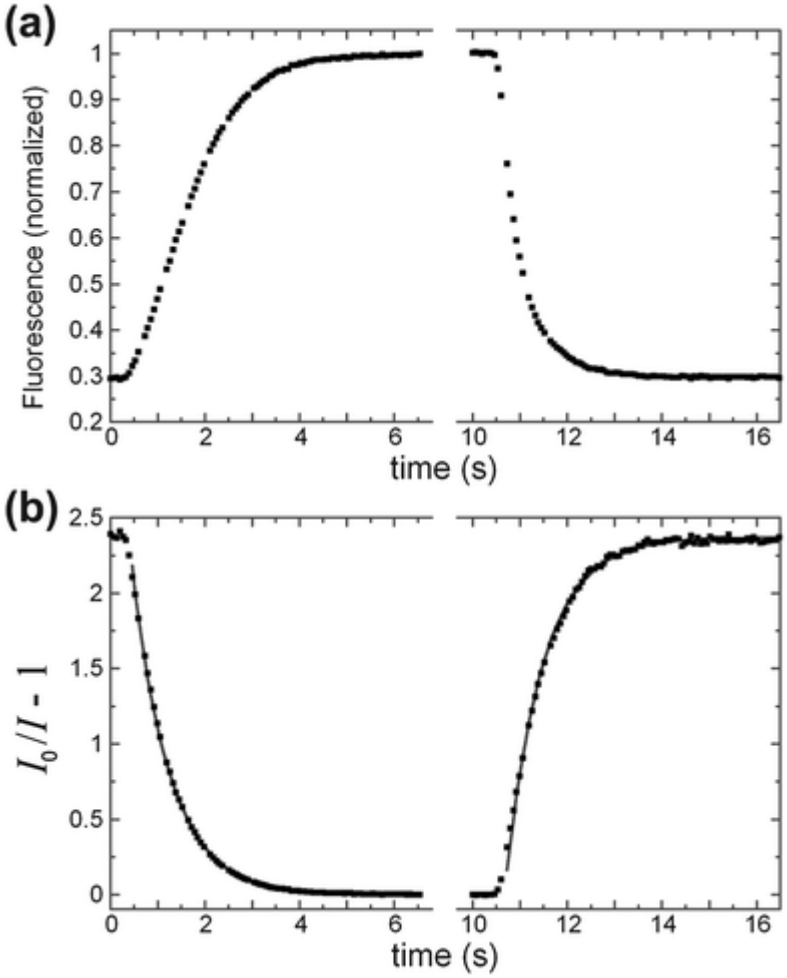

Figure 2-2: Dynamics of changes in the fluorescence of RTDP in a 25 μm wide flow-through channel under gas test channel 1 during switching of the gas fed to the gas inlets from O_2 to N_2 and back. The fluorescence was recorded at 15 frames per second with a Sony XCD-X700 camera. (a) Intensity of fluorescence as a function of time. The intensity is normalized to its level with N_2 fed to the gas channels. The gas was switched from O_2 to N_2 at ~0.5 sec and back at ~10.5 sec. (b) $I_0/I - 1$ (symbols) as a function of time, t, where I is the fluorescence intensity at a given moment, and I_0 is the intensity with N_2 fed to the gas channels. The dependences at $0.5 < t < 6.5$ sec and $10.5 < t < 16.5$ sec are fitted by exponential functions (continuous lines) $a \exp(-(t - t_1)/\tau)$ and $a[1 - \exp(-(t - t_2)/\tau)]$, respectively, with $a = 2.37$, $\tau = 0.79$ sec, $t_1 = 0.40$ sec and $t_2 = 10.67$ sec.

Because the solubility of O_2 in PDMS is ~6 times higher than in water (at room temperature),[6] the O_2 content of a saturated solution in a 6 μm deep flow channel is equivalent to that of an ~1 μm thick layer of PDMS. Given the diffusion coefficient of O_2 in water, $D_w = 2 \times 10^{-5}$ cm^2/s, the time of diffusive mixing of O_2 in a channel with a depth h = 6 μm is estimated as $h^2/(2D_w)$ = 9 msec. Hence, the measured exchange time τ = 0.79 sec is almost entirely due to the exchange of O_2 content in the 50 μm thick PDMS membrane between the gas channel and flow channel. We used FemLab to perform a numerical simulation of the PDMS layer as a slab with a thickness d = 50 μm that is initially filled with a substance with a diffusion coefficient $D_p = 3.4 \times 10^{-5}$ cm^2/s,[6] with boundary conditions of zero concentration at the top (gas channel with a flow of N_2) and zero diffusion at the bottom (cover glass). The concentration at the bottom of the slab was decaying exponentially with a characteristic time of τ = 0.30 sec, whereas the experimentally measured decay time of 0.79 sec corresponded to a diffusion coefficient of $D_p = 1.3 \times 10^{-5}$ cm^2/s inside PDMS. We note that a simple estimate of the time of diffusive exchange, $d^2/(2D_p)$ = 0.96 sec, is in good agreement with the simulation. A likely reason for the discrepancy between the experiment and simulation is reduced gas permeability of the 50 μm thick PDMS layer near its surfaces that reduces the rate of gas exchange through it.[14] Another source of the

discrepancy is a finite exchange time of the gas in the gas channel, which is estimated as ~0.1 sec.

The time dependences in Fig. 2-2 indicate that there is a fast transport of O_2 between the flow and gas channels and that the O_2 content of liquid in the flow channels reaches a steady state in ~4 sec after switching the gas fed to the gas channel network. The O_2 content in the liquid might still be out of equilibrium with that in the gas channel because of the presence of two competing gas transport mechanisms: the diffusion in the plane of the device (*xy*-plane, Fig. 2-1) and the flow of the liquid that causes downstream (*y*-direction) transport of O_2 dissolved in the liquid. The diffusion of O_2 in the *x*-direction (Fig. 2-1) is not likely to cause any net transport, because the gas test channels extend over a distance of 6 mm in this direction, practically precluding any gradients of O_2 in the *x*-direction. On the other hand, the width (*y*-axis extension) of the gas test channels is relatively small (600 μm), and large gradients of O_2 in the *y*-direction are expected near the channel edges.

To test whether the *y*-direction transport of O_2 by the diffusion and flow has an effect on the O_2 concentration in flow channels under a gas test channel, we measured distributions of fluorescence intensities in a 25 μm wide flow channel when both gas inlets are fed with N_2 or O_2. The measurements were done at three differential pressures between the flow inlet and outlet (0.25, 0.5, and 1 psi) corresponding to mean flow velocities

of 65, 130, and 260 μm/s. The fluorescence micrographs were taken at least 30 sec after the gas supply was switched to allow the gas content to reach a steady state (*cf.* Fig. 2-2). The ratio of fluorescence intensities under N_2 and O_2 as a function of a position in the *y*-direction is shown in Fig. 2-3 for a region under the gas test channel 1 and immediately upstream of it. (We note that with an appropriate subtraction of the background, the ratio of fluorescence intensities is not sensitive to non-uniformity of the channel depth and of fluorescence illumination and light collection.)

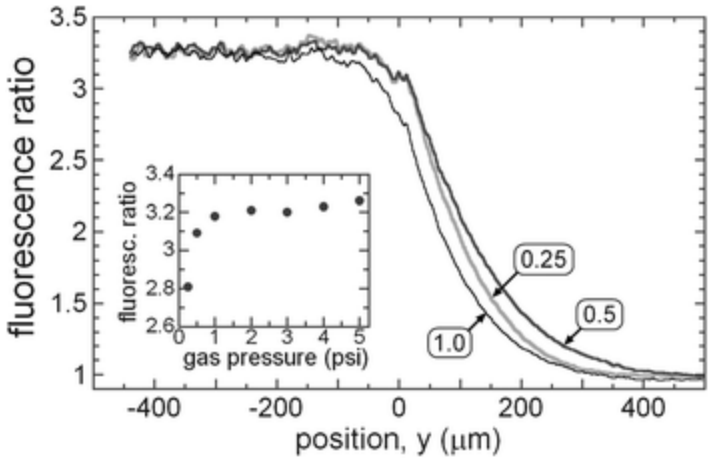

Figure 2-3: The ratio of fluorescent intensities between the states when the gas inlets are fed with N_2 and with O_2 (both at 5 psi) as a function of position, y, along a flow-through channel at three differential pressures between the flow inlet and outlet. The three curves are marked by the values of the differential pressure, ΔP, in psi, 0.25, 0.5, and 1. The position $y = 0$ corresponds to the upstream edge of gas test channel 1. *Inset*: the ratio of fluorescence intensities under the internal region of gas test channel 1 between the states when the gas inlets are fed with N_2 and with O_2 as a function of pressure at the gas inlets, P_g. The flow of liquid was driven at $\Delta P = 0.5$ psi.

The three curves in Fig. 2-3 have two main features in common. First, the fluorescence ratio at large distances upstream of the gas channel always approaches unity, indicating that the switching of the gas has little effect on the O_2 content in these far-upstream areas. This result is expected. At large distances, the gas channel is an inefficient source or sink of O_2, because the diffusion of O_2 occurs in two dimensions in the *yz*-plane (whereas the gas channel is only 150 μm deep) and the characteristic time of diffusive exchange increases as the distance squared. Because of the slow rate of the diffusive exchange, the shapes of the curves upstream of the gas channel ($y > 0$) differed and depended on the long-time history of the content of the gas channel. Second, in the range of y corresponding to an internal region of the gas channel starting 200 μm from the channel edge ($y < -200\mu m$), where all growth chambers are situated, the fluorescence ratios for all three curves have plateaus with mean values that are within 0.5% of 3.25. (The measurement error in this experiment was estimated as 0.5–1%, with two major sources being the uncertainty in the background level and the variation of the channel depth with the pressure in the flow layer.) The experimental results indicate that in this internal region under the gas channel there are no gradients of $[O_2]$ along the y-direction and no dependence of $[O_2]$ on the liquid flow rate, when either N_2 or O_2 flow in the gas channel.

The absence of $[O_2]$ gradients along the *y*-direction precludes any net diffusive transport in this direction. Together with the absence of the dependence of $[O_2]$ on the liquid flow rate, it indicates that $[O_2]$ in the flow-through channels and growth chambers under the internal region of the gas channel is at equilibrium with $[O_2]$ in the gas channel. As an additional control, we measured the N_2/O_2 ratios of fluorescence intensities in segments of 8 different flow channels that were all in the internal region under gas channel 5. The ratios had a mean value of 3.25 with a coefficient of variation of 0.5%, indicating that, as expected, $[O_2]$ is constant under a given gas channel.

The composition of gas flowing through the gas channels is expected to vary on the way from the inlets to the test region due to diffusive exchange through the channel walls with the gas dissolved in the PDMS chip (which is air in the beginning of the experiments). This variation in gas composition is expected to depend on the gas flow rate, becoming strong at low flow rates. Therefore, to test the magnitude of this effect, we repeated the experiments described above with the gas flow driven by pressures, P_g, from 0.25 to 5 psi (always the same pressure for N_2 and O_2). The flow rate through the gas outlets was a linear function of P_g (not shown). The fluorescence intensity ratio under gas channel 1 (inset in Fig. 2-3) steeply increased with P_g up to P_g of 1 psi but was largely leveled off at P_g >1 psi. When both gas inlets were fed with O_2, sampling of the gas

emerging from gas outlet 1 gave [O_2] = 88.9% at a P_g = 0.25 psi, [O_2] = 96.0% at P_g = 0.5 psi, and [O_2] saturated at 100% at P_g > 1.2 psi, in qualitative agreement with the on-chip fluorescence tests. These results indicated that at a gas pressure of 5 psi, the gas exchange through the channel walls did not have appreciable effect on the composition of gas in test area. Therefore, the measured ratio of fluorescence intensities under the gas channel with N_2 and O_2 corresponds to the ratio of fluorescent yields I_0/I_{100} between RTDP fluorescence without quenching and with quenching by a saturated solution of O_2.

To test for possible cross-talk between adjacent gas channels, we measured the fluorescence intensity in device 1 under gas channel 1 when the gas inlet 1 is fed with N_2 and gas inlet 2 is fed with O_2. Under these conditions, the gas in channel 1 is pure N_2 as in the previous test, whereas the gas in channel 2 is 87.5% N_2 and 12.5% O_2 (see Fig. 2-4 a below) instead of pure N_2 in the previous test. When divided by the fluorescence intensity profile with pure O_2 in all gas channels (not shown), the measured profile was similar to the curves in Fig. 2-3 with an unchanged ratio of 3.25 under the gas channel 1, indicating that there was no cross-talk between the gas channels 1 and 2. To test for evaporation of water from the flow channels, a 3 ppm solution of FITC in a 10 mM phosphate buffer was perfused through the device at a differential pressure of 0.5 psi (same as used in experiments with *E. coli* below). The evaporation would

raise the concentration of FITC and thus the intensity of fluorescence in the flow channels. The fluorescence was measured under gas channel 9 (at the most downstream growth chambers) with and without flow of dry air through the gas channel network and was found to be unchanged to within 0.5%, indicating that the flow of air caused practically no evaporation of water from the flow channels.

To obtain an alternative estimate of the difference in $[O_2]$ between gas channel 1 and the flow channels under it, we used FemLab (COMSOL) to perform a time-dependent two-dimensional simulation of a fragment of the *yz*-cross-section of the device (see Supplementary Information and Fig. 2-8 for details). The distribution of $[O_2]$ under gas channel 1 found in the simulation (Fig. 2-8 b) had a shape similar to the experimentally obtained distributions of the N_2/O_2 fluorescence ratio in Fig. 2-3. In particular, in a 200 μm wide internal region (*y* from −400 to −200 μm) corresponding to the area of growth chambers in the device, $[O_2]$ was above 99.9%, which is within 0.01% of $[O_2]$ in the gas channel. Therefore, the results of the simulations agree with the experimental findings and indicate that $[O_2]$ in the growth chambers very closely matches $[O_2]$ in the gas channels above the growth chambers.

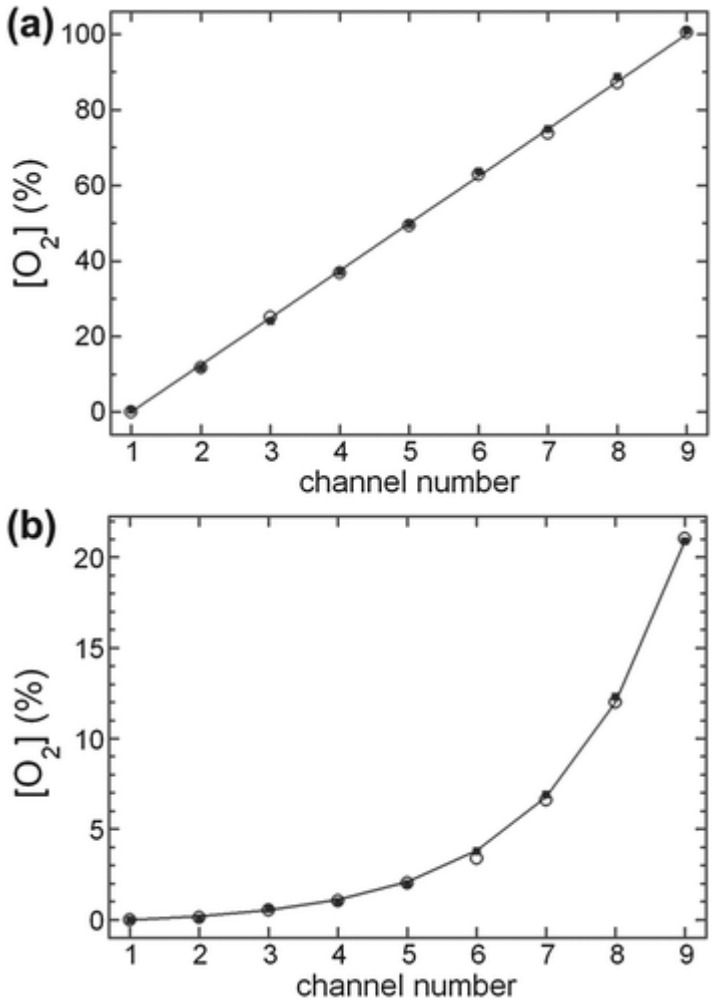

Figure 2-4: Concentrations of oxygen, $[O_2]$, (in % of pure oxygen) generated in the 9 gas test channels, as measured by the fluorescence of RTDP in flow-through channels under the gas test channels (open circles) and by the off-chip gas sampling (solid squares). Solid lines show the values of $[O_2]$, which the device is designed to generate. (a) Device 1 built to generate a linear dependence of $[O_2]$ on the channel number, n, $[O_2] = 12.5\% \times (n - 1)$. (b) Device 2 built to generate an exponential dependence of $[O_2]$ on n, $[O_2] = 20.9\% \times (3^{(n-1)/2} - 1)/80$.

Generation of linear and exponential series of O_2 concentration

To generate a linear series of [O_2] spanning from 0 to 100%, gas inlets 1 and 2 of device 1 were fed by N_2 and O_2, respectively, both pressurized at 5.0 psi. The flow channels were filled by a 250 ppm (by weight) solution of RTDP, as before, with ΔP = 0.5 psi applied between the flow inlet and outlet. [O_2] under the gas test channels 1–9 was calculated based on the intensity of fluorescence, I, measured in a 25 μm flow-through channel under the internal region of the gas channel (>100 μm from the edges) as $[O_2] = (I_0/I - 1)/(I_0/I_{100} - 1)$, where I_0 and I_{100} were the intensities of fluorescence measured when both gas inlets were fed with N_2 and O_2, respectively (open symbols in Fig. 2-4 a). In parallel, [O_2] in the gas mixtures coming out of the gas outlets was measured by the off-chip oxygen analyzer (solid symbols in Fig. 2-4 a). The [O_2] values evaluated from the fluorescence and off-chip sampling both closely followed the linear series of [O_2] that the device was designed to generate (solid line in Fig. 2-4 a). The root-mean-square (RMS) of the differences between the target and actual values of [O_2] as measured by the fluorescence intensity and off-chip analyses were 0.6% and 0.8%, respectively. The RMS of the differences between the results of [O_2] measurements by the two methods was 0.8%, which was within the 1% accuracy of the oxygen analyzer as stated by the manufacturer.

To generate an exponential series of [O_2] spanning from 0 to 20.9%, gas inlets 1 and 2 of device 2 were fed by N_2 and air, respectively. The inlet pressures were set at ~5 psi and subsequently adjusted to bring [O_2] at the gas outlet 5 to its target value of 2.1%. (The final pressure values, 4.84 psi and 4.65 psi, for N_2 and air, respectively, were somewhat different from each other, which was most likely due to imperfections in the device fabrication.) As in the previous experiment, [O_2] was measured in parallel from the fluorescence and off-chip sampling (Fig. 2-4 b). The values of [O_2] from both types of measurements closely followed the exponential dependence on the number of the gas outlet, n, that the device was designed to produce, $[O_2] = 20.9\% \times (3^{(n-1)/2} - 1)/80 = 20.9\% \times \{\exp[k(n-1)] - 1\}/80$, where $k = \ln(3)/2$ (solid line in Fig. 2-4 b). The RMS of the differences between the expected and measured values of [O_2] was 0.17% and 0.13% of [O_2] for the measurements by fluorescence and off-chip sampling, respectively, and the RMS of the differences between the measurements by the two methods was 0.20% of [O_2]. In particular, for gas channels 2–4 with the expected [O_2] of 0.19, 0.52, and 1.10%, [O_2] was measured at 0.14, 0.53, and 1.04%, respectively. This range of [O_2] corresponded to $1 \leq I_0/I < 1.025$, and the accuracy of measurements of I_0/I was improved to ~0.001 – 0.002 (limited by the variations of the channel depth and the fluctuations of the light source), corresponding to 0.05 – 0.1% in [O_2].

Changing pH in flow channels by injection of CO_2 into gas channels

To test the equilibration between the flow channels and gas channels for a gas other than O_2, we used the setup with the two solenoid valves to switch the gas fed to the two gas inlets from air to CO_2 and back to air. The diffusion of CO_2 through porous polypropylene membranes sandwiched between channels machined in PMMA was used before to create gradients of pH in the channels.[27] Indeed, when dissolved in water, CO_2 produces carbonic acid and bicarbonate, thus reducing the pH of the solution. Therefore, [CO_2] in the solution was monitored by the intensity of fluorescence of FITC, which is an increasing function of pH with a strong dependence near pH 7. Device 1 was filled with a 3 ppm solution of FITC in a pH 7, 10 mM phosphate buffer and its flow through the device was driven by a differential pressure of 0.5 psi. The pressure of both air and CO_2 was set at 5 psi, as before. After the gas fed to the gas inlets was switched from air to CO_2, the intensity of fluorescence of FITC under gas test channel 1 decreased by a factor of ~20 within 0.47 sec based on 90–10% criterion (Fig. 2-5). The initial fluorescence intensity was recovered, after the gas fed to the gas channel network was switched back to air. The transition back was much slower, however, ~10 sec based on 90–10% criterion (Fig. 2-5). We note that based on the value reported for the diffusion coefficient of CO_2 in PDMS (2.2×10^{-5} cm^2/s or 1.5 times lower

than for O_2),[6] the CO_2 exchange was expected to have an exponential relaxation time of ~1.2 sec (*cf.* Fig. 2-2 b).

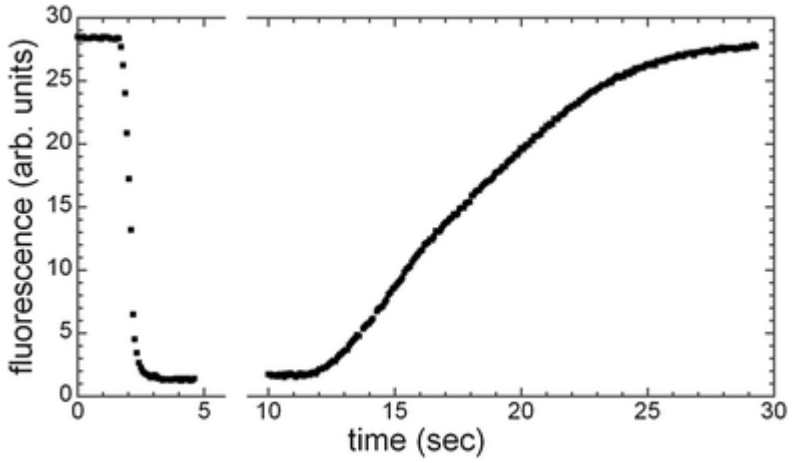

Figure 2-5: Time dependence of fluorescence (in arbitrary units) of a 3 ppm solution of FITC in a phosphate buffer (with pH = 7.0 when exposed to air) measured in a flow-through channel under gas test channel 1. The gas supplied to the two gas inlets was switched from air to pure CO_2 at 1.8 sec and back to air at 12 sec.

To estimate the change in pH in the flow channels caused by CO_2 of the gas channels, we measured the pH of the FITC solution in a test tube after it was saturated with CO_2 (by bubbling pure CO_2 through it) and found it at 4.5. A 3 ppm solution of FITC in a buffer with pH 4.5 was then prepared, and the intensity of its fluorescence in the same flow-through channel was measured (with air in the gas channel above it). The fluorescence was ~1.6 in the units of Fig. 2-5, which was, within the experimental uncertainly, identical to the value measured in the previous experiment with CO_2 in the gas channel. This result was consistent with equilibrium between [CO_2] in the gas and flow channel and also indicated

that the flow of CO_2 in the gas channel reduced pH of the buffer solution by 2.5 points, from 7.0 to 4.5. The relatively large change in pH explains the strong asymmetry between the transition curves from air to CO_2 and back from CO_2 to air. Because H_2CO_3 is a weak acid, the number of protons per dissolved molecule of CO_2 decreases as pH is reduced. Moreover, pH itself is a logarithmic function of the concentration of protons in the solution, making pH and the reduction in pH-dependent fluorescence of FITC a strongly non-linear, saturating function of $[CO_2]$. Therefore, when the same FITC solution was bubbled through with 5% CO_2 in air, its pH decreased from 7.0 to 5.8, about a half of the reduction measured for 100% CO_2. In other words, a major reduction in pH and FITC fluorescence occurs after $[CO_2]$ in the solution is increased from zero to a few percent a short time after the gas is switched from air to $[CO_2]$, and the initial level of fluorescence is not recovered until the last few percent of $[CO_2]$ diffuse out of the solution, after the gas is switched back to air. In terms of practical applications, injection of $[CO_2]$ into the gas channels proved to be an efficient way to rapidly reduce the pH of the solution in the flow channels.

Culturing E. coli *in chambers with different O_2 concentrations*

To demonstrate an application of the proposed technology of on-chip generation of series of $[O_2]$ to live cell experimentation, we cultured *E. coli* in the chambers of microfluidic device 2, measured their growth curves,

and tested the dependence of the growth curves on [O_2]. Our goal was to perform a feasibility study only. Therefore, the experiments were done at room temperature (instead of 35 °C as is optimal for *E. coli*) and the numbers of sampled colonies and cells were relatively small. In all experiments, the cell culture medium was perfused through the device at a differential pressure of 0.5 psi.

As in the previous study,[4] the size of an *E. coli* colony in a growth chamber was evaluated by measuring the total power of fluorescence in the chamber under the assumption that the power of GFP fluorescence per cell is constant. This is a reasonable assumption in a logarithmic growth phase, when the rate of cell growth and division is constant, and a dynamic equilibrium is expected to exist between the synthesis and folding of GFP on one hand and its degradation and dilution due to cell growth and division on the other hand. In addition, whenever possible, particularly in small colonies, the number of cells was also assessed by direct counting. In our preliminary experiments, we noticed that in colonies under gas channel 1, which were exposed to completely anaerobic conditions (pure N_2), the number of cells remained nearly constant for hours, whereas the total power of fluorescence gradually increased and nearly doubled after several hours. This was likely because the transition from an aerobic culture in the test tube to the anaerobic growth chambers led to a change in the relationship between the rates of GFP production, degradation, and

dilution due to cell division. The cells eventually reached a steady level of fluorescence, but it required many hours, apparently because of a reduced rate of intracellular processes in the N_2 atmosphere at room temperature.

Therefore, to avoid the long term adaptation processes during the measurement of growth curves, cells were loaded into the chambers in the evening and incubated overnight in an N_2 atmosphere by feeding N_2 to both gas inlets. In the morning, the gas supplied to gas inlet 2 was switched to air, exposing cells under gas channels 1–9 to different graded levels of O_2 (Fig. 2-4 b). The growth curve measurements were started 3–4 hours later to allow the cells to accommodate to the new conditions and to reach a steady level of fluorescence per cell. Two or three separate growth chambers were selected under each of the gas test channels, and the images of GFP fluorescence in the chambers were periodically taken (Fig. 2-6). When the imaging was started, the number of cells per chamber varied between 5 and 50.

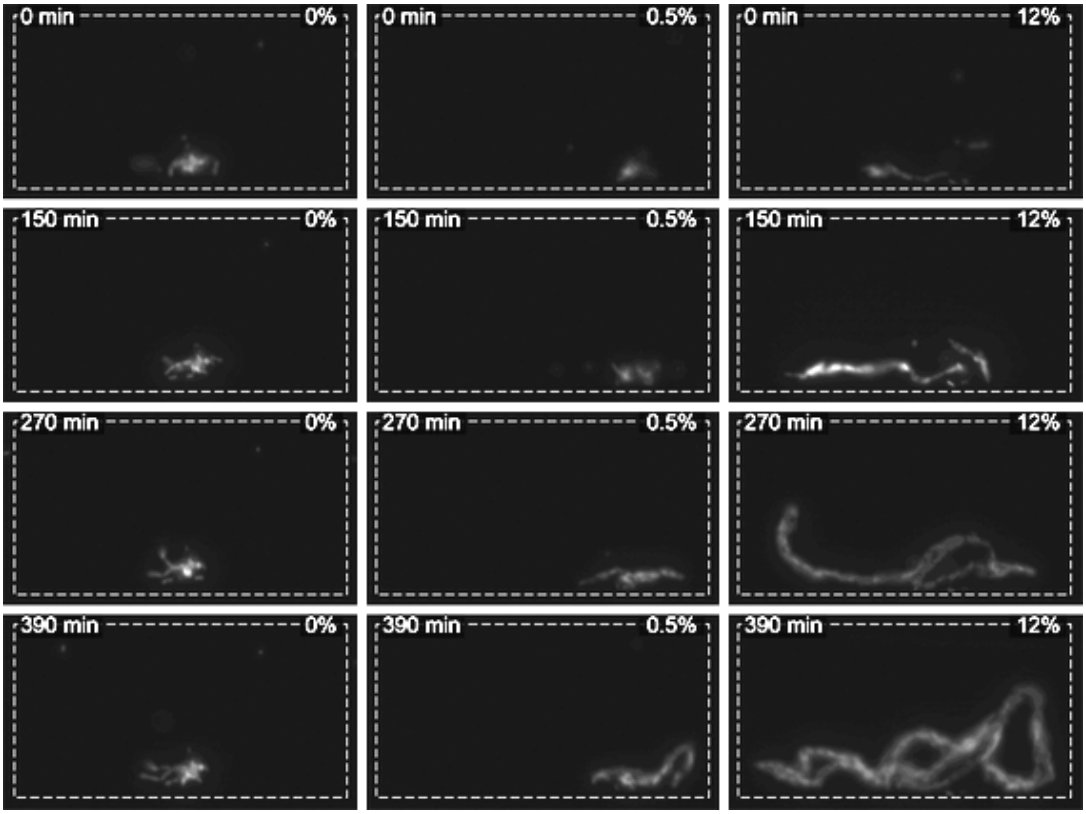

Figure 2-6: Fluorescence micrographs of three growth chambers with E. coli colonies at different time points. The chambers were situated under the gas test channels with [O_2] of 0% (left column), 0.5% (central column), and 12% (right column). The photographs were taken at 0, 150, 270, and 390 min from the point at which the growth curve measurements were started. Dashed lines show the boundaries of the growth chambers, 100 × 50 μm in size. The micrographs were taken with a 60×/1.2 WI objective and a CoolSnap HQ camera, under illumination with the royal-blue LED using a GFP filter cube.

The time dependence of the integral fluorescence in the growth chambers showed that, as expected, cells grew faster at higher [O_2] (Fig. 2-7 a) and the largest increase in the colony growth rates occurred at [O_2] near zero, when the conditions changed from completely anaerobic to microaerobic. The division rate leveled off at ~0.55 hr^{-1} or 110 min per

division, when [O_2] increased to ~7%. Somewhat unexpectedly, however, we repeatedly found by direct cell counting and measurements of fluorescence that cells exposed to pure N_2 ([O_2] = 0) did not divide at all and the integral fluorescence of colonies exposed to pure N_2 remained unchanged within the experimental error. On the other hand, the addition of as little as 0.2% of O_2 (1% of air in the air/N_2 mixture) led to a slow but measurable growth with a division time of ~6 hours (evaluated by the total power of fluorescence and confirmed by the direct cell counting), and at [O_2] = 0.5% the division rate reached about a half of its saturated level (Fig. 2-7 b). A t-test indicated that the growth rate at [O_2] = 0.2% was significantly higher than at [O_2] = 0 ($p < 0.01$) and the growth rate at [O_2] = 0.5% was significantly higher than at [O_2] = 0.2% ($p < 0.025$).

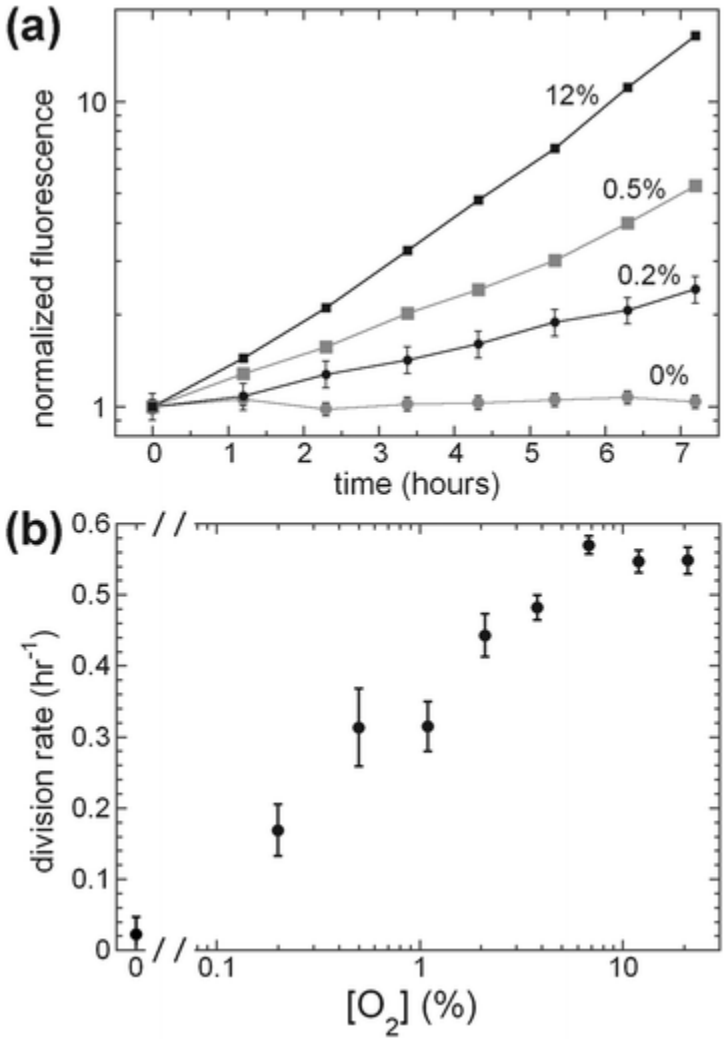

Figure 2-7: Growth of E. coli colonies at various concentrations of oxygen, [O_2]. (a) Growth curves (in semi-logarithmic coordinates) in chambers with [O_2] = 0, 0.2, 0.5, and 12% are shown by gray circles, black circles, gray squares, and black squares, respectively. [O_2] = 100% corresponds to the medium in equilibrium with pure O_2 at 1 atm. The colony growth is measured by the total power of fluorescence recorded from the area of the growth chamber, and the fluorescence is normalized to its value at time zero. Each growth curve shows an average of data from two growth chambers. All curves were obtained from a single experiment. (b) The rate of cell division (in inverse hours) as a function of [O_2] in semi-logarithmic coordinates. The time between cell divisions was calculated as the doubling time of the total power of fluorescence in the growth chamber. Each data point represents an average of growth exponents obtained from growth curves in an average of 5 separate chambers in two different experiments. Error bars are SEM.

When cells were cultured in the same room and in the same medium in a 15 mL test tube, which was covered by a loose cap and placed on a shaker rotating at 240 rpm, their growth rate was ~0.48 hr^{-1} (as measured by OD_{600} between 0.11 and 0.42). This growth rate was consistent with the growth rates measured on the chip, especially taking into account that without active air bubbling, the aeration of the test tube culture was not perfect. In another experiment, cells were cultured in a sealed 15 mL test tube, which was equipped with a gas inlet and outlet (again, at the same room temperature, in the same medium and with 240 rpm shaking), and the medium was bubbled with N_2 at 0.6 mL/sec. The OD_{600} increased from 0.16 to 0.49 within 19 hr, corresponding to a growth rate of 0.085 hr^{-1} and division time of ~12 hr. This growth rate was substantially lower than the growth rate measured on the chip at $[O_2]$ = 0.2%, but unlike the on-chip cultures exposed to pure N_2, the test tube culture bubbled with N_2 showed measurable growth. A possible reason for the difference in the growth rates is that the bubbling of the test tube culture with N_2 was not as efficient in setting a pure N_2 atmosphere in the medium as the positioning of the microfluidic growth chambers under a gas test channel ventilated with N_2 (see a more detailed discussion below).

Discussion and Conclusions

The proposed technology and devices have three major capacities: on-chip generation of series of mixtures with different gas content out of two gases fed to the device; setting the gas content of liquid in microchannels in the flow layer by a flow of a designed gas mixture through channels in the gas layer; fast variation of the gas content of the liquid in the flow channels. To generate gas mixtures with linearly and exponentially varying concentrations of O_2, the gas channel layers of the devices had gas-mixing networks of a type used before for mixing liquids.[17] The original networks were modified to account for a much higher diffusivity in the gas phase (0.2 cm^2/s for N_2/O_2 mixture versus $\sim 10^{-5}$ cm^2/s for small molecules in an aqueous solution) and relatively large volumetric flow rate required to minimize the unwanted changes in the gas composition caused by the diffusive exchange with the gas contained in the porous PDMS chip (inset in Fig. 2-3). The on-chip gas-mixing network in device 2 made it possible to generate seven customized N_2/O_2 mixtures out of air and N_2 fed to the device and to use these two readily available gases and two gas supply lines to study the growth of *E. coli* colonies at nine different O_2 concentrations in a single chip.

The fast switching of the gas composition utilizes a special feature of PDMS, its high permeability to low-molecular gases. When the composition of the gas fed to the gas inlets of the device is switched, $[O_2]$ in

the flow channels changes with a characteristic delay time (exponential decay time) of 0.8 sec (Fig. 2-2), with a similar response time of ~1 sec found for [CO_2] (Fig. 2-5). These relatively short gas exchange times make the technique a promising tool for testing real-time responses of live cells to the changes in [O_2] and pH in terms of changes in the cell shape, motility, intracellular distribution of soluble proteins, and conformations of proteins and protein complexes. For the last two tasks, fluorescently labeled proteins could be used. Importantly, the switching of the gas content is accomplished by molecular diffusion and, with an appropriate balance of gas pressures, does not cause any flow of liquid or other mechanical perturbation in the flow channels. In addition, it does not change the concentrations of nutrients, ions, macromolecular factors, or any other non-volatile components of the liquid, except for products of chemical reactions between components of the gas mixture and liquid, such as bicarbonate for CO_2 and water. Numerical simulations indicate that the gas exchange time is proportional to the square of the thickness of the membrane between the gas and flow channel. Therefore, decreasing the membrane thickness below the current value of 50 μm is expected to reduce the gas exchange time to <0.8 sec.

The results of experiments with O_2, N_2, and the RTDP solution indicated that, within the experimental precision, the composition of gas dissolved in an aqueous solution under the internal region of a gas channel

is identical to the composition of gas in the gas channel (Fig. 2-3 and 2-4). (The experimental error was ~1% near 100% [O_2] and ~0.1% at 0–1% [O_2].) Numerical simulations (Fig. 2-8) further showed that the matching between [O_2] in the flow channels and gas channels can be as close as 0.01%. These findings from measurements with a fluorescent dye and numerical simulations were corroborated by the experiments on culturing *E. coli* in growth chambers of the device. We consistently found no detectable colony growth in chambers exposed to pure N_2 and significant growth of colonies in chambers exposed to air/N_2 mixtures with [O_2] as little as 0.2% (Fig. 2-7).

It is instructive to estimate how the consumption of O_2 by growing bacteria may influence [O_2] in the growth chambers. The O_2 consumption of *E. coli* was reported to increase linearly with the division rate,[28,29] reaching 20 mmol per hour per 1 g of dry mass (20 mmol/hr/g) at a growth rate of ~1 division per hour. At the growth rate of 0.2 divisions per hour measured in the microfluidic device at [O_2] = 0.2% (Fig. 2-7), the O_2 consumption was reported at ~6 mmol/hr/g. With the *E. coli* cell footprint of ~2 μm^2 and its dry mass of ~0.3×10^{-12} g (taken to be 27% of the live cell mass[30]), a tightly packed monolayer of *E. coli* corresponds to a dry mass density of 0.15 g/m^2. The O_2 consumption of the monolayer at [O_2] = 0.2% is then expected to be 0.9 $mmol/m^2/hr$ or 0.25 $\mu mol/m^2/s$. This consumption requires a supply equivalent to a flux of pure O_2 (44.6 mol/m^3

of gas at 1 atm) at a rate $J = 5.6 \times 10^{-9}$ m^3/m^2/s = 5.6×10^{-9} m/s. Given the PDMS thickness $d = 5 \times 10^{-5}$ m, O_2 solubility in PDMS $b = 0.18$, and O_2 diffusion coefficient $D_p = 1.3 \times 10^{-9}$ m^2/s, the difference in [O_2] across the PDMS layer, $\Delta[O_2]$, required to provide this flux (which is diffusion driven) can be found as $\Delta[O_2] = Jd/(bD_p) = 1.2 \times 10^{-3}$ or 0.12% of pure O_2.

If the practical goal is to limit $\Delta[O_2]$ to 0.01%, which is 1/20 of the [O_2] = 0.2% that device 2 is designed to impose in growth chambers under gas channel 2 (Fig. 2-4), cell densities of up to 1/12 of a tightly packed monolayer can be allowed in these growth chambers. For the 50 × 100 μm chambers used in the experiments, this cell density amounts to ~200 cells per chamber, which is 3–5 times higher that the cell numbers typically reached by the end of our experiments (Figs. 2-6 and 2-7). Cell colonies in chambers at [O_2] > 6% reached substantially larger sizes and had ~3 times higher growth rate that was expected to lead to the O_2 consumption at rates of ~15 mmol/hr/g.[28,29] Nevertheless, for [O_2] = 6%, the condition $\Delta[O_2]$ = 1/20 [O_2] is satisfied at $\Delta[O_2]$ equal to 0.3%. At this value of $\Delta[O_2]$ the flux of oxygen is expected to be $J = \Delta[O_2]bD_p/d = 1.4 \times 10^{-8}$ m/s (equivalent to 2.3 mmol/m^2/hr), which is expected to suffice for a very large colony of up to 2500 cells (close to a tightly packed monolayer or 1/6 of the chamber volume). The estimates for the O_2 supply also indicate that the device should efficiently evacuate from the culture chambers the gases generated

as a result of cell metabolism and respiration, if these gases have good solubility and high diffusivity in PDMS, as is the case for CO_2.

The capacity of the proposed device to maintain bacterial colonies at well-defined low levels of [O_2] (such as 0.2% maintained within 0.01%) in spite of the continuous consumption of O_2 by the cells could prove useful for detailed studies of cell cultures at microaerobic conditions ([O_2] << 21%). To compare the device with a large-scale culture in a test tube, flask, or a chemostat, we note that the time of equilibration of [O_2] between a growth chamber and the gas test channel above it can be estimated as $\tau' = dh/(6D_p) \approx 38$ msec (see Supplementary Information for a detailed discussion). This equilibration time corresponds to the time of O_2 diffusion through a water layer of thickness $l = \sqrt{2D_w\tau'} \approx 12\mu m$. Therefore, a large-scale culture with conditions similar to those on the chip would have to involve intensive bubbling with a gas mixture of a desired [O_2] in combination with vigorous agitation that would homogenize [O_2] on scales down to 12 μm within ~38 msec (with the homogenization on scales below 12 μm occurring by molecular diffusion). Such conditions would be very difficult to implement in large-scale cultures.

The techniques and devices for generating series of different gas mixtures and for culturing cells in media with well-defined [O_2] can have numerous potential applications in microbiology and cell biology. They can be used to study the levels of expression of various genes associated with

anaerobic and aerobic metabolism of *E. coli* and other microorganisms at high throughput and with [O_2] controlled with a resolution and accuracy that are difficult to achieve with conventional tools. The devices and techniques introduced in this paper can also be used to study gene expression and cell division rates under conditions when [O_2] changes in time along a prescribed pattern with switching times as short as 1–2 sec. The devices could provide a convenient platform to study the dependence of metabolism and gene expression on the concentration of other gases, in particular CO_2,[31] and be applied to culturing anaerobic organisms. With some modifications, the devices can also potentially be used for detailed analyses of responses of higher eukaryotes, including mammalian cells, to various steady levels and temporal patterns of [O_2] (hypoxia, normoxia, oxidative stress), mimicking diverse cell microenvironments in a variety of pathological and physiological conditions.[32]

Supplementary Information

To obtain an alternative estimate of the difference in [O_2] between gas channel 1 and the flow channels under it (*cf.* Fig. 2-3), we used FemLab to perform a time-dependent two-dimensional simulation of a fragment of the *yz*-cross-section of the device (Fig. 2-8). The fragment included the gas channels 1 and 2 (*cf.* Fig. 2-1), with the boundary conditions of [O_2] = 100% and 87.5%, respectively (Fig. 2-8 a). The device

was simulated as a monolith of PDMS with a 50 μm thick layer between the gas channel and the insulating lower boundary (cover glass) and with O_2 diffusion coefficient D_p = 1.3 × 10^{-5} cm^2/s, as evaluated from the gas switching tests (Fig. 2-2). The flow channels and the active flow of the liquid through them were not incorporated in the simulation. The initial conditions were [O_2] = 21% everywhere in PDMS and the distribution of [O_2] was allowed to evolve for 1 min. The final distribution of [O_2] under gas channel 1 (Fig. 2-8 b) had a shape similar to the experimentally obtained distributions of the N_2/O_2 fluorescence ratio in Fig. 2-3. In particular, in a 200 μm wide internal region (y from -400 to -200 μm) corresponding to the area of growth chambers in the microfluidic device, [O_2] obtained from the simulation was above 99.9%, which is within 0.01% of [O_2] in the gas channel. Therefore, the simulations indicate that [O_2] in the growth chambers of the device is expected to match [O_2] in the gas channels very closely.

A conspicuous difference between the experiment and simulations is that at $y > 0$ the fluorescence intensity ratio in Fig. 2-3 (experiment) decays substantially faster than [O_2] in Fig. 2-8 b (simulation). This difference is most likely due to the flow of the RTDP solution in the negative y-direction, which was not incorporated in the simulation. To estimate the effect of the flow on the [O_2] distribution, we first note that because of 6 times higher solubility of O_2 in PDMS as compared to water,

the total O_2 content of a flow channel with the depth h = 6 μm is equivalent to the O_2 content of an $h/6$ = 1 μm layer of PDMS (which is in equilibrium with water in the channel). The characteristic time of equilibration of [O_2] in the flow channel with [O_2] in the gas channel by diffusion through PDMS with thickness d = 50 μm can thus be estimated as $\tau' = dh/(6D_p) \approx 38\, msec$. The time of [$O_2$] equilibration along the vertical direction in the flow channels, which is estimated as $h^2/(2D_w) = 9\, msec$ (D_w = 2 × 10^{-5} cm^2/s is the diffusion coefficient of [O_2] in water), is substantially shorter and can thus be neglected.

For the velocity of 260 μm/s in the flow channel at the driving pressure of 1 psi, the equilibration time of 38 msec corresponds to a distance of 10 μm along the flow direction, implying that within a distance of 200 μm, the difference in [O_2] between the flow and gas channel is expected to become indistinguishable from zero. Therefore, for a driving pressure of 1 psi or less, the contribution of the liquid flow in setting the distribution of [O_2] under a gas channel is expected to be small compared with that of the diffusive exchange with the PDMS chip (Fig. 2-8). Specifically, the flow is not expected to have any appreciable effect on [O_2] in the regions with the growth chambers (>200 μm from the gas channel edges). We finally note that the estimated equilibration time $\tau' = dh/(6D_p) \approx 38\, msec$ is different from the equilibration time after

switching of the gas fed to the gas channel network (Fig. 2-2), τ, which was measured at 0.8 sec and estimated as $d^2/(2D_p)$, because the two equilibration processes are essentially different. In the former case, only $[O_2]$ in the aqueous solution is changing as the solution advances along the flow channel, whereas $[O_2]$ in the PDMS membrane remains constant. In contrast, in the latter case, the O_2 content of the PDMS membrane is exchanged, which involves the diffusive transport of $6d/h$ = 50 times larger amount of O_2.

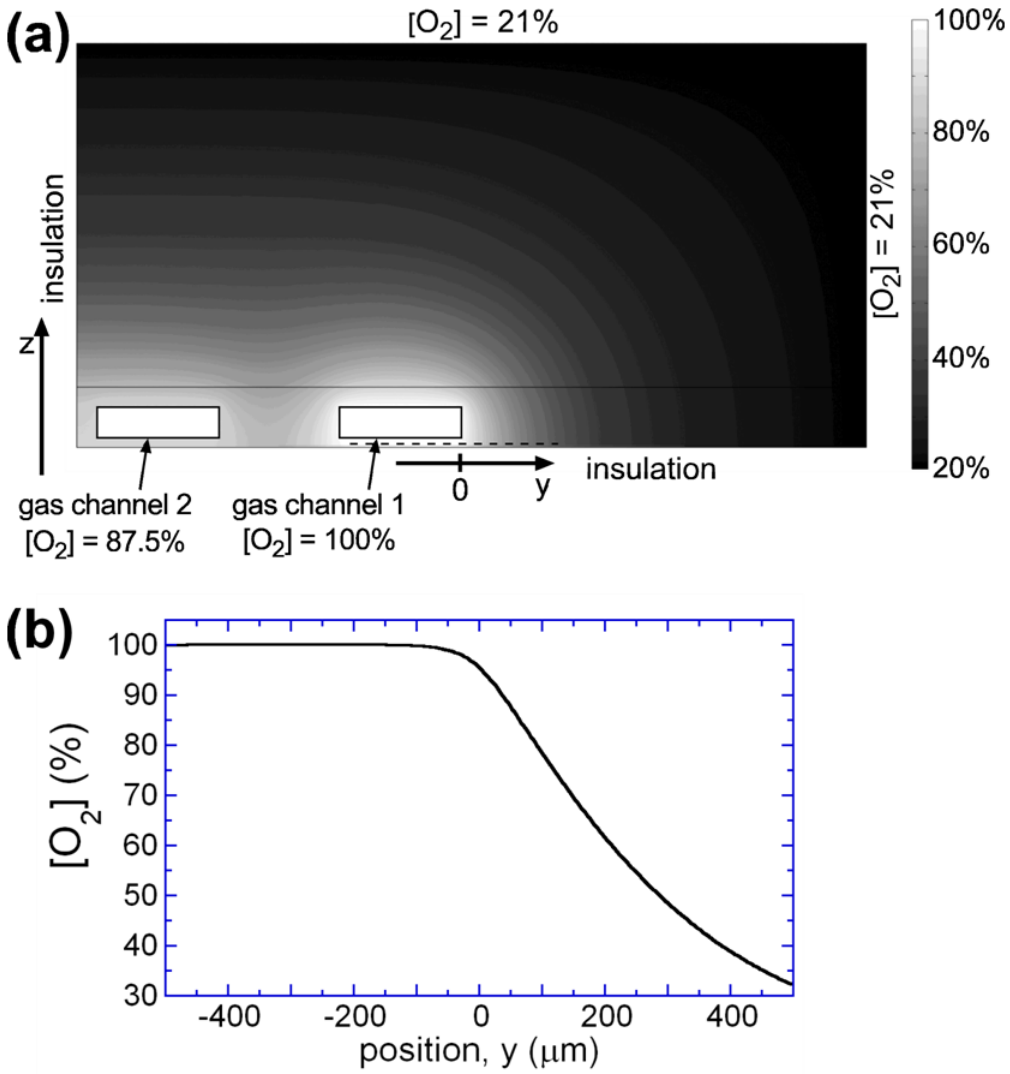

Figure 2-8: Time-dependent two-dimensional numerical simulation of oxygen concentration, $[O_2]$, in a fragment of cross-section of device 1 in *yz*-plane. (a) Computational domain, 3.9 × 2 mm in size, with $[O_2]$ after 1 min coded by a grayscale, as shown by a legend bar on the right. Gas channels 1 and 2, with their boundaries at $[O_2]$ = 100% and 87.5%, respectively, are shown as white rectangles. Boundary conditions are insulation at the bottom (coverglass) and on the left (internal area of the test region) and $[O_2]$ = 21% (air) at the top and on the right. (b) $[O_2]$ under gas test channel 1 at 5 μm above the lower boundary (along the dashed line in panel (a)) as a function of position, y, with y = 0 corresponding to the right edge of the gas test channel (*cf.* Fig. 2-3).

Acknowledgements

We thank Terry Hwa, Dalai Yan, Sydney Kustu, and Rob Gunsalus for helpful discussions and Virginia VanDelinder for useful suggestions. The work was partially funded by DARPA and by NSF NIRT Grant No. 0608863.

Chapter 2.1, in full, is a reprint of the journal article "Fine temporal control of the medium gas content and acidity and on-chip generation of series of oxygen concentrations for cell cultures", *Lab on a Chip*, 2009. Polinkovsky, Mark; Gutierrez, Edgar; Levchenko, Andre; and Groisman, Alex. The dissertation author was the first author and a leading contributor of this paper.

2.2: Computer-Controlled Multi-Channel Gas Mixer

2.2.1: Motivation for Developing a Stand-Alone Gas Mixer

We saw in Chapter 2.1 how to create a set of different oxygen concentrations, [O_2], on-chip from just two source gases. However, that technique has several drawbacks. The gas-mixing network is designed to output specific [O_2], in a certain spatial arrangement. These parameters can only be modified by designing and fabricating new devices with different gas-mixing networks. Moreover, only gas mixtures with a monotonic series of [O_2] can be generated in a given device. In addition, due to the limited accuracy of the microfabrication process, the resistances of channels in the on-chip gas mixer are always somewhat different from their intended values, resulting in variations in the [O_2] series produced by different devices.

To overcome these constraints, we have designed an off-chip, multi-channel gas mixer. All channels of the mixer are fed from the same two gas sources and each channel is independently controlled. This mixer can be used with a variety of microfluidic devices and other systems with sufficiently low gas consumption rates. Importantly, with the multi-channel mixer, there is no need to include an on-chip gas mixer, greatly simplifying the design and operation of the microfluidic devices. Moreover, the digital control of gas concentrations implemented in the mixer makes it

accurate and reliable, so the mixer can be used with a new device without needing a calibration of the [O_2]. After the mixer was developed and built, our laboratory has used different modifications of it in a wide variety of experiments: *E. coli* aerotaxis, migration of mammalian cells at different oxygen tensions, zebrafish hypoxia response, and testing the gene expression of mammalian cells cultured in multiwell plates at different levels of [O_2] (the subject of Section 2.3).

2.2.2: Design and Operation of Multi-Channel Gas Mixer

The multi-channel gas mixer (Fig. 2-9) is designed to mix two gases fed to its inlets in desired proportions and to supply the gas mixtures to microfluidic devices at volumetric flow rates, Q, of 0.1 – 0.3 mL/s. The mixer has 10 identical channels, each consisting of three essential elements: a miniature 3-way solenoid valve (LHDA 1223111H by The Lee Company), which has two inlets and one outlet and is periodically switched with a controlled duty cycle; a fluidic resistor connected to the common port (outlet) of the valve to control the flow rate through the valve by setting the pressure at its inlets; and a mixer tube downstream of the resistor to homogenize the gas mixture generated by the valve (Fig. 2-9 and 2-10). The 10 valves are face-mounted on a polished aluminum board with 3 rows of holes in it and 10 holes in each row (Fig. 2-9 and 2-10). The holes in the two outer rows are concentric with the valve inlets, and the holes in the central row are concentric with the valve outlets. 20 mm long pieces of stainless steel hypodermic tubing (gauge 15) are glued into the holes (Fig. 2-10). The steel tubing pieces in the outer rows are connected through short segments of Tygon tubing (with the internal diameter, ID, of 1/16") to two separate gas distributors (made of modified 10 cc plastic syringes), one for all normally-opened valve inlets and one for all normally-closed valve inlets. The former gas distributor is connected to a source of

filtered, pressure-regulated nitrogen, N_2 (99.995% purity), and the latter distributor is connected to filtered, pressure-regulated oxygen (O_2) or air.

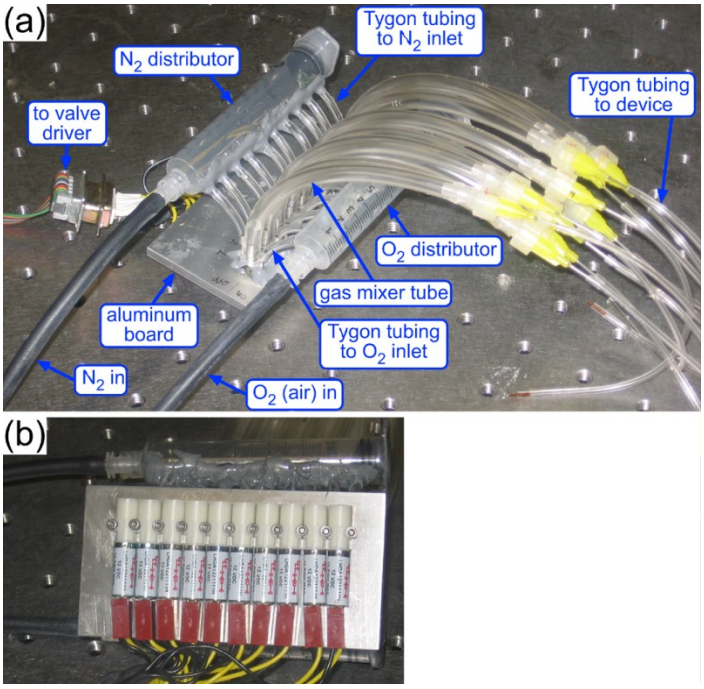

Figure 2-9: The 10-channel gas mixer. (a) Top view, showing two gas supply lines (for N_2 and O_2, made of black rubber), N_2 and O_2 distributors (modified plastic syringes), gas mixer tubes, and connecting tubing lines. (b) Bottom view showing the array of 10 miniature 3-way solenoid valves face-mounted on the aluminum board.

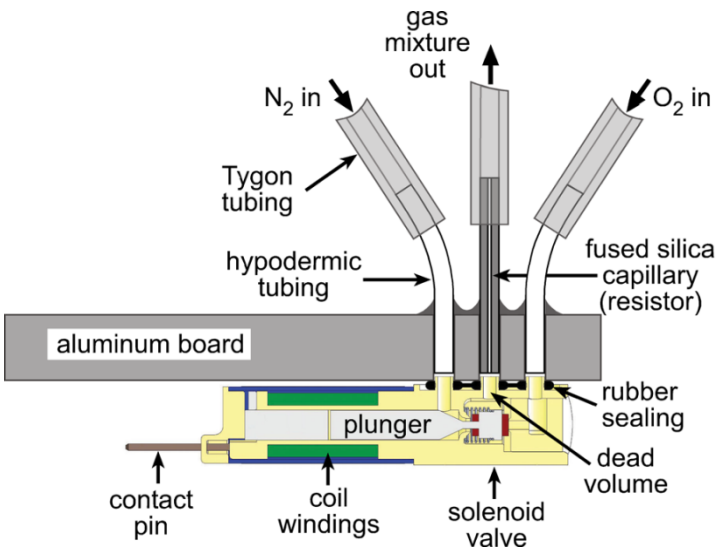

Figure 2-10: Schematic drawing showing a cross-section of a 3-way solenoid valve mounted on the aluminum board of the gas mixer. Three pieces of gauge 15 hypodermic tubing are glued into three holes in the board, which are concentric with the ports of the valve. The central piece, which is connected to the common port (outlet) of the valve, has a fused silica capillary with an ID of 100 µm glued into it. The capillary serves as a fluidic resistor. The space between the head of the plunger of the valve and the entrance of the capillary is the dead volume of the mixer.

The pieces of hypodermic tubing in the central row, which are connected to the outlets of the solenoid valves, have 20 mm long segments of polyimide-coated fused-silica capillaries (TSP100200 by Polymicro Technologies) glued into them, with the rest of the tubing interior filled with epoxy (Fig. 2-10). The capillaries have an ID of 100 µm and serve as fluidic resistors immediately adjacent to the valve outlets. Air flow rates of 0.1 and 0.2 mL/s through a valve (as measured by the displacement of water from a graduated cylinder) require pressures of 2 psi (14 kPa) and 4 psi (28 kPa), respectively, at the valve inlets. The pieces of hypodermic tubing in the central row are connected to the gas inlets of the microfluidic

device through the gas mixer tubes, which are 10 cm long segments of Tygon tubing with ID = 3/16", and 12 cm long segments of Tygon tubing with ID = 0.75 mm (with some connectors in between; Fig. 2-9 and 2-10).

The solenoid valves are switched on and off periodically. The period, T, is normally 2 s. The duty cycle of the valve, which is defined as the ratio between the time when the valve is powered (ON time), t_{ON}, and the period, T, determines the fractions of time that the valve is opened to the flow of O_2 (or air) and to the flow of N_2. At a volumetric flow rate Q = 0.1 mL/s in both ON and OFF states, the gas flow in the mixer tube has a mean velocity $\bar{v} = 0.56$ cm/s and one period of the valve corresponds to an ~1.1 cm long segment of gas injected into the mixer tube, with a total of 9 segments in the mixer tube.

To explore the distribution of oxygen concentration, $[O_2]$, in a mixer tube, we used a code in Matlab to perform one-dimensional (1D) numerical simulations of the $[O_2]$ profile along the tube, accounting for the flow of gas and diffusion of O_2, but disregarding the non-uniformity of both flow velocity and $[O_2]$ over the cross-section of the tube. (The actual velocity profile was expected to be parabolic, leading to some non-uniformity of the $[O_2]$ profile across the tube.) The value of $[O_2]$ at the inlet (left edge) changed between 0 (N_2) and 100% (O_2) with the period T = 2 s and a duty cycle t_{ON}/T; O_2 diffused along the 10 cm computational domain with a diffusion coefficient, D_{gas} = 0.2 cm^2/s, and the entire O_2 distribution

uniformly moved towards the outlet (right edge) with velocity $\bar{v}$. The initial condition was $[O_2] = 0$ everywhere.

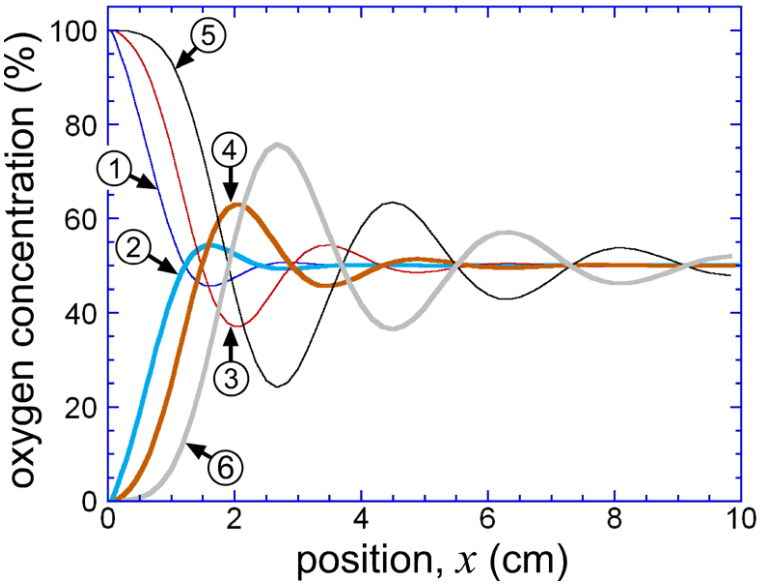

Figure 2-11: Distributions of oxygen concentration, $[O_2]$ (in %), along the 10 cm long gas mixer tube after 20 cycles of the solenoid valve starting from $[O_2]$ = 0% (when steady states are reached) from 1D numerical simulations in Matlab. The simulations were performed for oxygen diffusion coefficient D_{gas} = 0.2 cm²/s, a period T = 2 s, and a duty cycle t_{ON}/T = 50%. (The condition at the left boundary, x = 0, was changing periodically between $[O_2]$ = 100% for 1 s and 0% for 1 s.) The gas flow velocities (from left to right) were $\bar{v}$ = 0.56 cm/s (curves 1 and 2), 1.12 cm/s (curves 3 and 4), and 1.68 cm/s (curves 5 and 6) corresponding to the volumetric flow rates Q = 0.1, 0.2, and 0.3 mL/s, respectively. The odd- and even-numbered curves correspond to moments at the ends of the phases with $[O_2]$ = 100% (end of O_2 injection) and $[O_2]$ = 0% (end of N_2 injection) at x = 0.

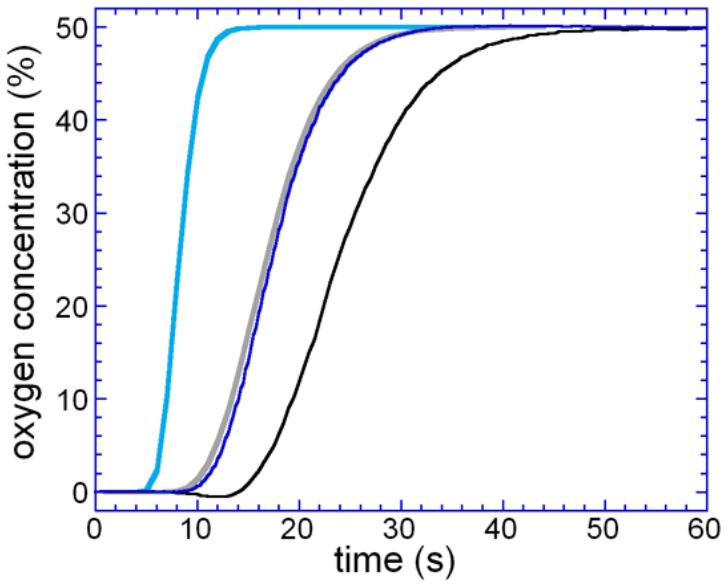

Figure 2-12: Oxygen concentration, $[O_2]$, as a function of time after the gas mixer is switched from a duty cycle resulting in $[O_2]$ = 0% to a duty cycle resulting in $[O_2]$ = 50%, as obtained from 1D numerical simulations (gray and light blue curves) and from experiments (black and dark blue curves). Gray and black curves are for a flow rate Q = 0.1 mL/s and the two blue curves are for Q = 0.2 mL/s. The two simulation curves show $[O_2]$ at the end of the gas mixer tube, and the two experimental curves show $[O_2]$ obtained from measurements in two microfluidic devices with ~150 µm thick layer of PDMS between the gas channels and the cover glass at the bottom of the chip. Based on our previous results,[26] for this PDMS thickness, one could expect an ~7 s delay in the response of $[O_2]$ in the flow channels to changes of $[O_2]$ in the gas channels, which can explain the apparent delay in the experimental curves as compared with the simulation curves. Interestingly, the experimental curve at Q = 0.2 mL/s (dark blue) is nearly identical to the simulation curve at Q = 0.1 mL/s (gray).

The simulations were performed for duty cycles of 0.5 (Fig. 2-11) and 0.1 (not shown), which were representative of proportional and disproportional mixing. The simulations at $\bar{v} = 0.56$ cm/s showed that when a steady state is reached after ~20 periods, $[O_2]$ at the outlet becomes equal to $t_{ON}/T \times 100\%$ with both fractional error and peak-to-peak

variations (within one period) of < 0.001 of the mean concentration for both duty cycles. The peak-to-peak variations remained at < 0.001 of $t_{ON}/T \times 100\%$ also at $\bar{v} = 1.12$ cm/s (corresponding to Q = 0.2 mL/s) and reached an appreciable level of ~0.08 of the mean only at $\bar{v} = 1.68$ cm/s (Fig. 2-11; with the mean value still within 0.001 of $t_{ON}/T \times 100\%$).

The simulations indicate that the mixing of the gas in the mixer tube is practically perfect with the steady state [O_2] matching the duty cycle up to Q = 0.2 mL/s. Moreover, according to the simulations, the steady state is established relatively quickly, with only 25 s at Q = 0.1 mL/s and only 11 s at Q = 0.2 mL/s required to reach 9/10 of the ultimate steady-state concentration (Fig. 2-12). The transition times between 1/10 and 9/10 of the steady-state concentration were even shorter, at 13 and 5 s for Q = 0.1 mL/s and 0.2 mL/s, respectively.

To test the switching time of the gas mixer experimentally, we measured [O_2] in the test channel of the device using a solution of the oxygen-sensitive fluorescent dye, RTDP. The fluorescence was measured as a function of time after all 9 channels of the mixer operating at Q = 0.2 mL/s were switched from a cycle generating [O_2] = 0% to a cycle generating [O_2] = 50% (dark blue curve in Fig. 2-12). Fluorescence micrographs of the test channel were taken every 0.5 s, and the intensity of fluorescence in the test channel, I, was converted into [O_2] using the equation $[O_2] = (I_0 / I - 1)/K_q$ (with I_0 and K_q measured separately), as explained in

the main text. The transition was 9/10 complete after 24 s, and transition time from $[O_2]$ = 5% to $[O_2]$ = 45% (1/10 – 9/10 through the transition) was 12 s. In a separate experiment, all 9 channels of the mixer were switched from a cycle generating $[O_2]$ = 25% to a cycle generating $[O_2]$ = 75% and a nearly identical transition curve was measured (not shown). The test was repeated at Q = 0.1 mL/s in a similar two-layer device that had the same thickness of the PDMS layer between the gas channels and cover glass (150 μm, similar to the device used in the study), and the transition was 9/10 complete after 34 s with 16 s between 1/10 and 9/10 through the transition. Somewhat longer transition times in the experiments, as compared to the simulations, were likely due to a substantial delay (estimated at ~7 s) in the response of $[O_2]$ in the flow channels (measured by the fluorescent dye) to changes of $[O_2]$ in the gas channels due to a relatively thick layer of PDMS between the two channel layers.[26]

To test for temporal variations of $[O_2]$ in the test channel of the device, in particular on the time scale of the period of the valve switching, T = 2 s, we acquired a 90 s time series of the intensity of fluorescence of RTDP in the test channel, I, taking 5 frames per second, and calculated $[O_2] = (I_0 / I - 1) / K_q$ for each frame. The mixer was fed with N_2 and O_2 at 4 psi and all of its channels operated at $t_{ON} / T \approx 0.5$ (with synchronous switching) and Q = 0.2 mL/s. The resulting 90 s time series (Fig. 2-13) showed that $[O_2]$ in the test channel remained nearly constant, varying

with a standard deviation, SD, of only 0.055% from its 46.3% mean value. This value of SD corresponded to a coefficient of variation, CV, of ~0.001, which was comparable to instrumental errors due to fluctuations in the power of fluorescence illumination and due to the vibration and drift of mechanical parts of the microscope. Moreover, Fourier analysis of the time series showed practically no component with the valve switching period of 2 s (it had an amplitude of 0.022% or 0.0005 of the mean value), which was experimental evidence for the efficiency of the gas mixer tube. (We note, however, that because of the estimated ~7 s delay between variations of $[O_2]$ in the gas channels and the test channel, the amplitude of the 2 s variations of $[O_2]$ in the test channel was expected to be reduced by a factor of ~20 compared with that in the gas channels.)

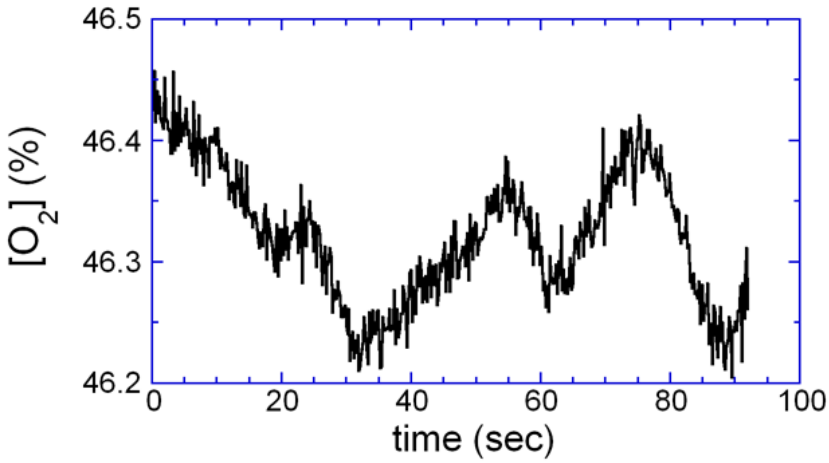

Figure 2-13: Time series of oxygen concentration, $[O_2]$, measured in the test channel of the microfluidic device. The gas mixer was fed with O_2 and N_2 and all its channels operated at a flow rate Q = 0.2 mL/s, with a period T = 2 s and a duty cycle of ~0.5. The measurements were done using oxygen-sensitive fluorescence of RTDP at a sampling rate of 5 times per second.

It is worth noting that, according to the simulations, in spite of the extreme simplicity of its construction, the gas mixer tube achieves two important goals, which are generally difficult to combine: very low variations of [O_2] at the outlet during a cycle of the valve (CV < 0.001 at Q = 0.2 mL/s) and a short transition time (only 5.5 cycles at Q = 0.2 mL/s). The combination of these useful features depends on the exact repetition of the valve cycles, including their period, T, and the ON time, t_{ON}. An important practical requirement for appropriate operation of the gas mixer is that the ratio between the volume of O_2, V_o, and the total volume of gas, V_t, passing through the solenoid valve during one cycle closely matches the desired value of [O_2] in the gas mixture.

The solenoid valves in the mixer had a short response time of ~4 ms, and from our previous work,[27] the repeatability of their switching was estimated as better than 1 ms. The valves were controlled using a home-built driver, which was interfaced with a dedicated computer through a National Instruments PCI-6503 card. The card was programmed using LabView code, and the timing of the signals sent to the valves was expected to be accurate to within 1 ms as well. The error of 1 ms was very small compared with the 2 s period of the valve cycles and was thus expected to lead to negligible errors in the definition of both T and t_{ON}. A much more significant source of error in the definition of [O_2] was the relation between the actual volume ratio V_o/V_t and the electronically

defined duty cycle, t_{ON}/T. Among the factors contributing to the lack of correspondence between the two ratios were differences in the pressures of O_2 (or air) and N_2 at the two valve inlets, difference between the viscosities of O_2 (or air) and N_2, and the presence of a dead volume between the plunger of the valve and the fluidic resistor (capillary; Fig. 2-10).

To minimize differences between the pressures of O_2 and N_2, both pressures were carefully adjusted and equilibrated using two sensitive regulators (8310ANBF5 by Porter Instruments) and a single high-accuracy pressure gauge (digital gauge by Heise with an accuracy of 0.015 psi), which was alternatively connected to the two regulators. The resulting pressure difference was estimated as <0.5% and was expected to lead to an insignificant error in $[O_2]$ in the gas mixture. The viscosities of N_2, air, and O_2 at 20 °C and atmospheric pressure are 1.747×10^{-5}, 1.837×10^{-5}, and 2.023×10^{-5} Pa·s, respectively. That is, the viscosities of air and O_2 are higher than the viscosity of N_2 by factors of k_a=1.05 and k_O=1.16, respectively. Therefore, one could expect to obtain a desired value of $[O_2]$ (in % of pure O_2) by setting the duty cycle at

$$t_{ON}/T = \frac{k_O[\mathrm{O_2}]}{100\% + (k_O - 1)[\mathrm{O_2}]} \tag{2-1}$$

when mixing O_2 and N_2, and at

$$t_{ON}/T = \frac{k_a[\mathrm{O_2}]}{20.9\% + (k_a - 1)[\mathrm{O_2}]} \tag{2-2}$$

when mixing air and N_2.

One could also expect, however, that the presence of the finite dead volume of gas between the plunger of the valve and the inlet of the fluidic resistor (Fig. 2-10) would necessitate corrections to the calculated duty cycles. Indeed, when the valve is switched from N_2 to O_2, the viscosity of the gas flowing through the capillary is lower than the viscosity of O_2, until the entire dead volume is purged of N_2. Vice-versa, immediately after the valve is switched from O_2 to N_2, the viscosity of the gas flowing through the capillary is higher than the viscosity of N_2. Therefore, the direct application of the equations 2.1 and 2.2 to calculate the duty cycle was likely to result in V_o/V_t somewhat higher than t_{ON}/T (and somewhat higher than desired $[O_2]$ in the gas mixture). The magnitude of this effect was expected to be proportional to the ratio between the dead volume and V_t. Therefore, we used face-mounted solenoid valves with a small dead volume and placed the capillaries very close to the valve outlets. (A large dead volume would also cause another undesirable effect, disproportionally high sensitivity of $[O_2]$ in the mixtures to small mismatches between the pressures at the two valve inlets.)

The values of $[O_2]$ in the gas mixtures produced by the mixer were evaluated with a commercial oxygen analyzer ($MAXO_2$ by Maxtec) with a nominal accuracy of 1%.[26] In addition, $[O_2]$ was also evaluated by measurements of fluorescence of RTDP in a microchannel (as described in

the main text and in Ref. 26) in a microfluidic device similar to one used in this study, with an expected absolute accuracy of better than 1% in $[O_2]$ (and down to 0.1% in $[O_2]$ at low $[O_2]$). Typical results of measurements of $[O_2]$ (in %) for mixtures of air and N_2 with t_{ON}/T from eq. 2-2 are shown in Table 2-1.

Table 2-1: Measurements of $[O_2]$ (in %) for mixtures of air and N_2 with t_{ON}/T from eq. 2-2.

Expected from eq. 2-2	0	2	4	6	8	10	12	14	16	18
Measured with analyzer	0.2	2.3	4.2	6.1	8.1	10.4	12.0	14.1	16.0	18.0
Measured by fluorescence	0.00	2.16	4.25	6.18	8.26	10.22	12.25	14.07	16.15	17.94

As expected, the direct application of eq. 2-2 resulted in somewhat higher than desired values of $[O_2]$. Therefore, to improve the accuracy of $[O_2]$ in the mixtures, we corrected the values of $[O_2]$ plugged into eq. 2-2, subtracting from them 0 to 0.2%, depending on the range. The results obtained with the corrections are shown in Table 2-2.

Table 2-2: Measurements of [O_2] (in %) for mixtures of air and O_2 with corrected t_{ON}/T.

Expected after corrections	0	2	4	6	8	10	12	14	16	18
Measured with analyzer	0.1	2.0	4.0	6.0	7.9	9.9	11.9	14.0	16.0	17.9
Measured by fluorescence	0.00	1.93	4.03	6.01	7.96	9.95	11.96	13.94	15.96	17.86

The values of [O_2] measured with both the oxygen analyzer and fluorescence microscopy were very close to the desired values, with an absolute standard deviation of 0.05% for both measurement techniques, which was as low as one could expect given the instrumental errors.

We also tested variations of [O_2] between the 9 channels of the gas mixer, when they were all operated at the same period T = 2 s with identical duty cycles. In this test, the mixer was fed with O_2 and N_2 at 4 psi (resulting in Q = 0.2 mL/s), the duty cycles were set at 0.114, 0.224, 0.334 and 0.435 (values producing [O_2] = 10%, 20%, 30%, and 40%, according to eq. 2-1), and [O_2] was measured with the oxygen analyzer. The results of the test (Fig. 2-14) indicated a good consistency of [O_2] in different channels. Its absolute standard deviations at t_{ON}/T = 0.114, 0.224, 0.334 and 0.435 were 0.12%, 0.17%, 0.19%, and 0.29%, respectively, which were well within the instrumental error of the analyzer. The variations of [O_2] between measurements taken on different days at the same Q, T, and duty cycle (not shown) were somewhat higher, but still within the error of the

analyzer. Therefore, once calibrated and corrected, the gas mixer could be reliably used without the necessity of monitoring [O_2] in the generated gas mixtures.

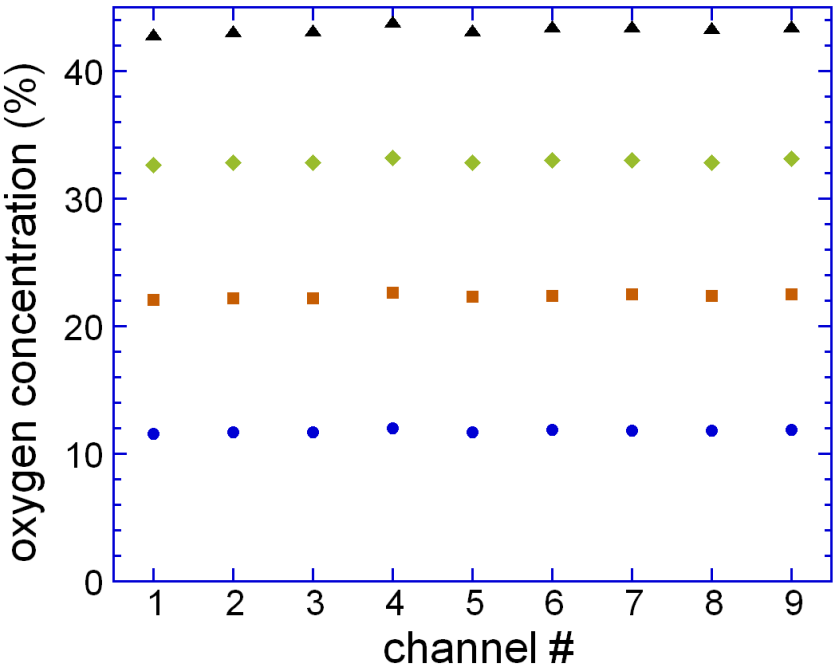

Figure 2-14: The values of oxygen concentration, [O_2], in gas mixtures produced by 9 channels of the gas mixer fed with O_2 and N_2 at 4 psi, with the valves switched with a period T = 2 s at duty cycles of 0.114 (circles), 0.224 (squares), 0.334 (diamonds), and 0.435 (triangles). [O_2] was measured with the MAXO_2 oxygen analyzer.

The hydrodynamic resistance of the fluidic resistors in the gas mixer was chosen to obtain volumetric flow rates of air in the range of 0.1 – 0.3 mL/s at air pressures of 2 – 6 psi at the mixer inlets. Pressures in this range do not require special reinforced tubing and are simple to adjust and to measure accurately. The flow rates in the range 0.1 – 0.3 mL/s result in small gas consumption (with each of the 10 channels of the mixer

operating at 0.2 mL/s, a standard 200 ft^3 gas cylinder is expected to last for more than a month) and from our previous work,[26] we expected a flow rate of 0.2 mL/s to be sufficiently high to prevent contamination of the gas mixtures fed to the device by the atmospheric air. (The sources of contamination include the diffusion through the porous PDMS chip and uncontrolled leakages at the tubing connection points and its effect on $[O_2]$ in the gas mixtures is expected to be inversely proportional to the gas flow rate.[26]) Importantly, when the gas channels have a depth of 150 μm (as in the presented device), which is easy to produce using standard microfabrication procedures, Q = 0.2 mL/s corresponds to a relatively low pressure at the gas inlets. Indeed, for a fully developed laminar flow of air with viscosity $\eta_a = 1.8 \cdot 10^{-5}$ Pa·s at a volumetric flow rate $Q = 0.2$ mL/s in a square channel with a width $w = 150$ μm and length $L = 12\,\text{mm}$ (typical dimensions for the gas channels of the device), the pressure drop along the channel is $\Delta P = 28\frac{L\eta_a Q}{w^4} \approx 2.4$ kPa. Because the gas outlet is vented to atmosphere, ΔP also represents the gauge pressure at the gas inlets and the maximal gauge pressure inside the gas channels, and at its estimated value of 2.4 kPa, this pressure is expected to cause only minor stresses in the device and minor deformations of gas channels. Moreover, the pressure drop of 2.4 kPa at $Q = 0.2$ mL/s is ~10 times smaller that the pressure drop across the fluidic resistors at the same gas flow rate (4 psi ≈ 28 kPa).

Therefore, connecting the gas mixer to the microfluidic device is expected to have little influence on the operation of the mixer (other than ~8% reduction in Q), and $[O_2]$ in the gas channels is not expected to change due to variations in the dimensions of the channels or layout of the device, provided that the channel resistances remain sufficiently small.

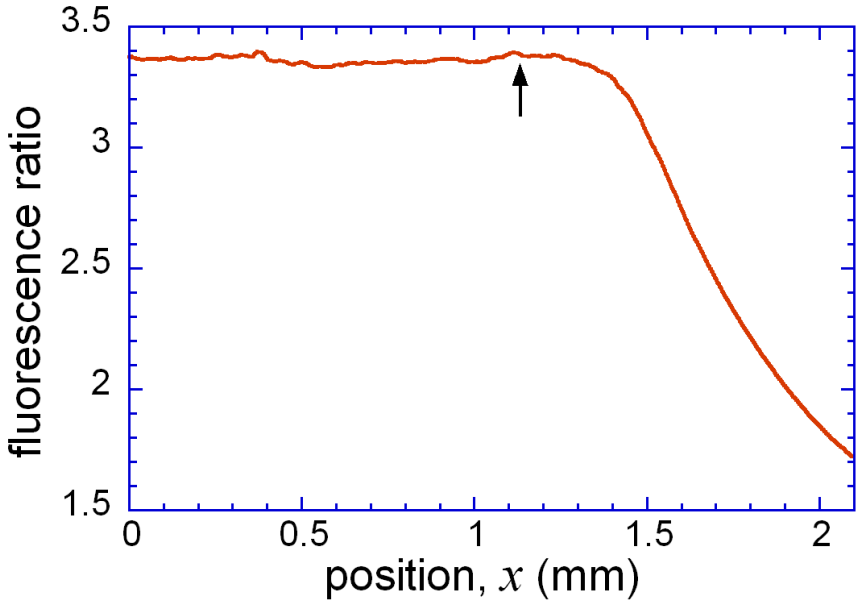

Figure 2-15: The ratio of intensities of fluorescence in the 90 μm wide test channel (filled with a 250 ppm solution of RTDP) between the cases when N_2 and O_2 is fed to all 9 gas inlets. The fluorescence ratio is plotted as a function of the position along the test channel, x, with $x = 0$ corresponding to the middle of gas channel 5 (the center of the gas channel array). x = 1.125 mm (indicated by an arrow) corresponds to the center of gas channel 9 (*cf.* Fig. 3 in Ref. 26). In the internal region, between $x = 0$ and 1.125 mm, the mean value of the measured fluorescence ratio is 3.35 and the standard deviation is 0.0135, corresponding to ~0.5% in $[O_2]$, which is within the measurement error. Therefore, the results of the measurements are consistent with the result of numerical simulations that when the gas mixtures with the same $[O_2]$ are fed to all gas channels, $[O_2]$ in the internal region of the test channel is uniform and identical to $[O_2]$ in the gas channels.

Chapter 2.2.2, in full, is a reprint of the "Supplementary Information" from the journal article "Generation of oxygen gradients with arbitrary shapes in a microfluidic device", *Lab on a Chip*, 2010. Adler, Micha; Polinkovsky, Mark; Gutierrez, Edgar; and Groisman, Alex. The dissertation author was a participating investigator of this paper.

2.3: Precise Control of O_2 Concentration in 24-well Cell Culture Plates for Hypoxia Studies

Abstract

Oxygen concentration, [O_2], is an important physiological parameter. Cell culture media are often exposed to the atmosphere, with [O_2] ≈ 21%, whereas normal levels of [O_2] in the human body are substantially lower, varying in a 2-9% range. Furthermore, many pathologies involve hypoxia, with even lower [O_2]. A common technique to create normoxic and hypoxic conditions in cell cultures is by using O_2-controlled incubators and specialized hypoxic chambers. Nevertheless, such systems tend to be bulky and expensive, only provide a single [O_2] at a time, and are usually incompatible with high-resolution time-lapse microscopy. Moreover, low solubility and diffusivity of O_2 in aqueous media can lead to major delays in the onset of hypoxia after a cell culture dish is placed into a hypoxic atmosphere. In addition, at high cell densities, [O_2] around cells can drop substantially below that in the gas phase. Here, we describe a system consisting of a multi-channel, computer-controlled gas mixer and a set of microfabricated gas-distribution strips, which are mounted on a standard 24-well plate to effectively impose a series of up to 6 different levels of [O_2] in media in the wells with an uncertainty of <0.5%. Slow bubbling through media in the wells enhances the vertical

transport of O_2, accelerating the onset of hypoxia ~15-fold, as compared to hypoxic chambers. The enhanced transport of O_2 also enables hypoxia assays with much greater cell densities and much more accurate control of [O_2] around cells at a given cell density. The system is tested by using real-time PCR to analyze the levels of expression of 4 different hypoxia-related genes in mouse fibroblasts exposed to 6 different levels of [O_2] in a single assay.

Introduction

Most mammalian cells use oxygen as the oxidizing agent in their metabolism and are thus sensitive to the concentration of oxygen, [O_2], in their environment. Hypoxic conditions, with [O_2] lower than normal, affect a wide variety of housekeeping and pathology-related cellular processes, including wound healing, angiogenesis, tumorigenesis, and immune and cell death pathways.[28-30] Additionally, chronic hypoxia and anoxia (lack of oxygen) can lead to morphological changes at the cellular level, while prolonged hypoxia underlies or contributes to deleterious conditions including diabetes, neurological problems, and stroke, among others.[28-31] Furthermore, the normal physiological level of [O_2] (normoxia) in the human body varies between tissues, depends on the distance from the closest blood vessel, and is considered to be in the range of 2-9%,[32] which is substantially lower than [O_2] ≈ 21% in a liquid medium at equilibrium

with atmospheric air. Therefore, to emulate normal physiological conditions in a tissue culture, in addition to using media with a suitable chemical composition, ionic content, and pH, it is important to set [O_2] at an appropriate normoxic level.

Experiments of mammalian cells at controlled [O_2] are most commonly performed in hypoxic incubators, which range from large and relatively expensive glove boxes to compact and inexpensive sealed chambers. However, compact hypoxia chambers or even standard glove boxes cannot be readily combined with high-resolution microscopes to monitor cells in real time. Some specialized hypoxic incubators integrated with microscopes are currently available (Hypoxia workstation by BioSpherix and VivaView system by Olympus), but they are expensive, high-end systems with limited flexibility. Apart from the difficulty of performing real-time microscopy, conventional hypoxic incubators only allow testing cells at a single [O_2] at a time. No less importantly, in standard hypoxic incubators, the desired [O_2] is imposed upon the liquid medium with cells by setting the proportion of O_2 in the gas mixture filling the incubator. (In addition to O_2 and N_2, the mixture usually contains CO_2.) In many cases, hypoxic conditions need to be applied to cells on a plastic (or glass) substrate under a considerable layer of liquid medium. When cells are cultured in a Petri dish or a flask in a glove box (or large hypoxic chamber), the medium can be stirred with a shaker, thus

facilitating the transport of O_2 between the gas phase and the medium around cells. However, if hypoxia is induced in a more compact hypoxia chamber, or if cells are cultured in a multiwell plate with small cross-section wells, stirring the medium by shaking is impractical or inefficient, and the O_2 transport occurs by diffusion only.

The solubility of O_2 in water, ~1 mM at 1 atm partial pressure at 37 °C (as compared to ~39 mM in the gas phase), and its diffusivity, $D_w \approx 3 \times 10^{-5}$ cm^2/s (as compared to 0.2 cm^2/s in the gas phase), are both relatively low, leading to a two-fold problem. First, after a culture dish (or a multi-well plate) with medium and cells on the bottom and is taken from an environment with atmospheric air ($[O_2] \approx 21\%$ in the medium initially) and placed into a hypoxic chamber, it takes substantial time until the medium around the cells becomes hypoxic. Indeed, without mixing, for a layer of medium with a thickness h, a characteristic time for equilibration of $[O_2]$ at the bottom of the dish with $[O_2]$ in the gas phase is $\tau_w = h^2/(2\ D_w)$. If $[O_2]$ in the incubator is set to zero, it will take time $t_w \approx 2.07\ \tau_w$ for $[O_2]$ at the bottom of the dish, $[O_2]_B$, to drop from 21% to 2% (~9/10 through the transition; from a numerical simulation). For a moderate layer of medium with h = 5 mm, the value of t_w is ~146 min, suggesting that cells plated on the dish bottom are exposed to hypoxia with a substantial delay. In experimental tests on the onset of hypoxia at the bottom of culture dishes placed into hypoxic chambers, the transition times were found to be

between 3 and 7 hours.[33,34] The problem can be remedied by using a cellular medium that is pre-equilibrated with an O_2-N_2-CO_2 gas mixture containing the desired low proportion of O_2. However, this approach may be practically difficult, especially for compact hypoxia chambers and for cells in multiwell plates.

Second, O_2 around cells on the dish bottom is continuously consumed by cellular respiration. As a result, after the initial transient process of $[O_2]$ equilibration is complete (at times greater than t_w), $[O_2]_B$ becomes lower than $[O_2]$ at the top, $[O_2]_T$ (surface of the medium), which is always at equilibrium with the gas phase. O_2 consumed by respiration is replenished by the diffusion of O_2 through the medium, from its surface to the dish bottom. According to Fick's law of diffusion, the diffusive flux can be calculated as

$$J = D_w([O_2]_T - [O_2]_B)/h \qquad (2\text{-}3)$$

and in a steady state, it is equal to the rate of O_2 consumption by cells per unit area, R (which is analogous to the reaction rate in chemistry), $J = R$. The value of R is a product of the rate of O_2 consumption by a single cell and the density of cells on the bottom. A high cell density leads to large R, and thus large J and large product $D_w([O_2]_T - [O_2]_B)/h$ in a steady state. Therefore, given the relatively low solubility of O_2 in water and relatively

low D_w, a moderate h and a large cell density may lead to a large difference in $[O_2]$ across the medium, $\Delta[O_2] = [O_2]_T - [O_2]_B$.

As a result, $[O_2]$ in the cellular environment may be substantially lower than its intended value, as defined by the proportion of O_2 in the gas phase. Importantly, unlike the delay in the onset of hypoxia, t_w, which can be readily estimated and accounted for, $\Delta[O_2]$ is a more subtle parameter. The value of $\Delta[O_2]$ is proportional to the cell density and cellular rate of respiration under particular experimental conditions, and thus may be difficult to evaluate and account for. Moreover, as cells proliferate and their density grows, $\Delta[O_2]$ is expected to increase and, hence, $[O_2]_B$ is expected to decrease, potentially changing the conditions in the course of an experiment and further complicating the situation. This effect can be particularly deleterious for hypoxic cell cultures, where $[O_2]_T$ is set at a low level. $[O_2]_B$ may decline precipitously, signaled by a growing $\Delta[O_2]$, which may lead to anoxic conditions around cells. This line of reasoning is corroborated by recent experiments, in which $[O_2]$ was monitored at the bottoms of wells with different densities of cells (mouse embryonic fibroblasts, MEF) and ~5 mm layers of medium.[34] The value of $\Delta[O_2]$ was found to be largely proportional to the cell density and independent of $[O_2]_T$, with $[O_2]_B$ approaching zero at a high cell density (100,000 cells/cm^2) and $[O_2]_T = 7\%$.[34]

It is worth noting that the diffusive flux, J, is an inverse function of the medium thickness, h, whereas t_w is proportional to h^2. Therefore, the steady-state concentration difference, $\Delta[O_2]$, and the delay time, t_w, can both be substantially reduced by decreasing h. The reductions are 5-fold and 25-fold, respectively, if h is decreased from 5 mm to 1 mm. Nevertheless, a major decrease in the medium layer thickness would be problematic for long-term experiments, because it may lead to excessive depletion of nutrients in the medium (and its contamination with metabolites) and an increased effect of evaporation on the chemical composition of the medium.

Well-controlled levels of $[O_2]$ and nutrients in cellular media have been generated using microfluidic devices made of polydimethylsiloxane (PDMS).[26,35-39] PDMS is porous and its O_2 permeability (the product of the solubility and diffusivity of O_2) is about an order of magnitude greater than that of water.[5] Therefore, PDMS layers of moderate thickness are only minor barriers for the diffusion of O_2. A desired level of $[O_2]$ can be effectively imposed upon a cell culture in a microchannel by flowing a gas mixture with the desired proportion of O_2 through nearby channels. At the same time, the medium in the cell culture can be replenished by continuous perfusion of fresh medium through the device.[26,35-39] However, microfluidic devices are substantially more difficult to handle than cell culture dishes. In addition, whereas microfluidic devices are well-suited for

high-resolution microscopy, they do not usually allow recovering an amount of cells sufficient for standard biochemical analyses. The high O_2-permeability of PDMS has also been used to control [O_2] and impose hypoxic conditions in adherent cell cultures in 6-well plates, by using gas-perfused PDMS plugs inserted into the wells, with the bottoms of the plugs touching the medium surface.[40]

Here we describe an experimental system consisting of a computer-controlled multi-channel gas mixer[41] and a set of gas distribution strips to rapidly impose and maintain well-defined [O_2] in media in the wells of standard 24-well cell culture plates (Fig. 2-16). The system makes it possible to set six different user-defined levels of [O_2] in quadruplets of wells, using just two commonly available gas mixtures, such as air with 5% CO_2 and N_2 with 5% CO_2. The gas mixture supplied to a gas distribution strip is slowly bubbled through ~5 mm layers of medium in the wells, making it possible to impose hypoxia near the well bottoms within ~22 min, compared to ~5.5 hours without bubbling. Testing of the setup with 3T6 mouse fibroblasts plated on the bottoms of the wells at different densities showed that at a high cell density without bubbling, [O_2] around cells can drop precipitously below [O_2] in the supplied gas, whereas with the bubbling, [O_2] around cells remains close to [O_2] in the gas. The setup was further used to for the analysis of expression of 4 different hypoxia-

related genes at 6 different levels of [O_2] in a single assay using real-time PCR (RT-PCR).

Experimental

Design and fabrication of the gas distribution strips

A gas distribution strip consists of a 2 mm thick, 90 × 18 mm two-layer ribbon and four PDMS plugs, which are attached to the ribbon from the bottom (Fig. 2-16 a). All parts of the strip are made of soft PDMS (XP-565 by Silicones, Inc.). The plugs are pushed into the wells of a standard 24-well plate to hermetically seal the wells, and the distance between the plugs (19.3 mm) is equal to the distance between the wells. To make a plug, an ~9 mm thick layer of cured PDMS is punched with an 18 mm diameter steel punch. The lower layer of the ribbon has a network of 150 µm deep gas channels engraved on its upper surface. The network consists of a single 1.5 mm wide, 80 mm long main gas channel running along the ribbon and four side channel arrays above the plugs (Fig. 2-16 a). The upper layer of the ribbon is cut from a 1 mm thick sheet of cured PDMS, and its lower surface seals the gas channels. The lower layer of the ribbon is cast using a lithographically fabricated master mold: a 6 inch silicon wafer with a 150 µm tall relief of SU8 epoxy on its surface. A 1 mm layer of PDMS pre-polymer is poured over the mold and cured by baking for 20 min in a 65 °C oven on a leveled support (to ensure uniform thickness). The

mold with cured PDMS is then spin-coated with an ~10 µm layer of PDMS pre-polymer (acting as a glue), and the plugs are placed onto it, carefully aligned with the SU8 relief on the mold. The PDMS pre-polymer is allowed to cure at room temperature overnight, bonding the plugs to the PDMS layer on the mold. The bonding is subsequently reinforced with more PDMS pre-polymer, which is applied around the plugs and cured at 65 °C for 20 min.

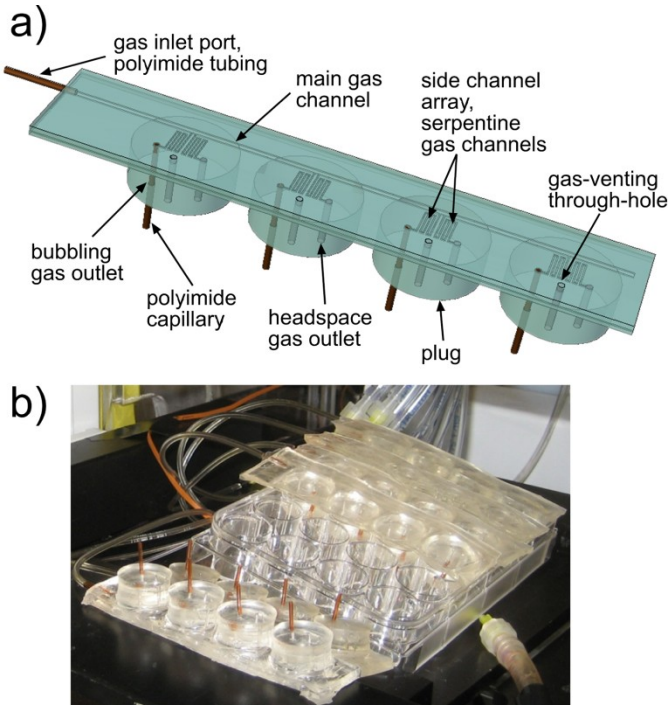

Figure 2-16: (a) Schematic drawing of a gas distribution strip. (b) Photograph of a 24-well plate with 4 gas distribution strips attached to it and 2 strips detached from it.

The PDMS layer with the plugs bonded to it is then separated from the wafer and cut into individual strips. Two holes are punched through

each plug, from top to bottom, at designated locations in the microchannel network. The upper layer of the ribbon is bonded to the lower layer by treating them both with oxygen plasma (10 sec exposure in Plasma-Preen II from Plasmatic Systems, Inc.). The inlet side of the two-layer ribbon is cut, exposing an edge of the main gas cannel. A segment of 18-gauge polyimide tubing is inserted into the main channel and glued into place by applying partially-cured PDMS around it. One through-hole is punched through each plug (and the two layers of the ribbon above it), forming a vent in an area free of gas channels (Fig. 2-16 a; also see below).

Each side channel array of the gas channel network consists of two serpentine channels, 75 µm and 150 µm wide. The outlets of the serpentine channels are open to the bottom side of the plug through the two vertical holes punched in the plug. The hole connected to the 75 µm wide channel has a 15 mm long 21-gauge polyimide capillary inserted into it. When a plug seals a liquid-filled well of a 24-well plate, the capillary becomes immersed in the liquid. Thus, the flow of gas emerging from the 75 µm wide channel bubbles through the liquid, while the flow from the 150 µm wide channel is directed to the headspace of the well. The gas is vented from the headspace to the atmosphere through the single through-hole punched in the plug. The lengths of the 75 and 150 µm wide serpentine channels are adjusted to provide an even distribution of gas flow between the 4 plugs of a strip. Because of the finite fluidic resistance of the 1.5 mm

wide main channel, the lengths of the serpentine channels decrease with the distance from the strip inlet.

When a low-[O_2] gas mixture is supplied to the strip, the flow of gas into the headspaces is used to counteract spontaneous leakages of O_2 from the atmosphere into the wells. Leakages are expected to occur due to the presence of the venting through-holes, the diffusion of air through the porous PDMS, and imperfect sealing of the PDMS plugs to the walls of the wells. Given the length of the venting through-hole (~10 mm) and the coefficient of diffusion of O_2 in air (0.2 cm^2/s), the leakage through a vent hole is expected to be negligible at gas flow velocities >2 cm/s through the hole. For the 0.3 mm diameter of the hole, this condition is equivalent to total volumetric gas flow rates >1.4 µL/s through the plug. The footprint of the gas channels in the strip is ~1 cm^2 per well; the thickness of the PDMS layer covering the gas channels from the top is 1 mm; O_2 solubility and diffusivity in PDMS are ~0.18 and ~2 × 10^{-5} cm^2/s, respectively.[26,5] Therefore, at [O_2] = 0 in the gas channels and 21% in the atmosphere, the diffusive flux of O_2 towards the gas channels is estimated at ~0.76 %·µL/s. To limit its effect to a <0.1% change in [O_2], the total gas flow through a plug should be >8 µL/s. Gas leakages around the plug perimeter are difficult to estimate. Therefore, a gas flow rate sufficient to impose the desired level of [O_2] with required precision had to be found experimentally.

The rates of gas bubbling and of gas flow through the headspace each require optimization. Excessive bubbling may mechanically perturb cells at the bottom of the well and can also lead to the medium bubbling up, out of the well. Conversely, slow bubbling leads to slow inception of hypoxia and slow transport of oxygen to cells. High gas flow through the headspace can lead to excessive evaporation of the medium, whereas low gas flow may be insufficient to counteract leakages of O_2 from the atmosphere. Several versions of the gas distribution strips were made, with different ratios of flow rates between the bubbling and headspace gas outlets. In this study, we used strips with a flow ratio of 1:2 (1/3 of the gas flow goes to the bubbling outlet).

In all experiments, gas distribution strip inlets were connected to separate outlets of the computer-controlled, 10-channel gas mixer, which is described in detail elsewhere.[41] The mixer has 10 miniature solenoid valves with fluidic resistors, and its two inlets are fed by two equally pressurized source gases (or gas mixtures). The valves are switched on and off periodically, and their duty cycles, which are adjusted individually, set proportions of the source gases in the mixtures delivered to the respective outlets. The gas-flow resistance of a fluidic resistor in the mixer was ~7 times greater than the cumulative resistance of a gas distribution strip. In this study, the inlets of the mixer were connected to compressed air and N_2 or, in experiments on mammalian cells, to air with 5% CO_2 and N_2 with 5%

CO_2. The inlet pressures were adjusted with two sensitive regulators and set equal to each other using a single digital pressure gauge. The uncertainty of $[O_2]$ at a given mixer outlet was estimated to be the sum of an ~0.02 fractional error and an ~0.1% absolute error.

Cell culture

3T6 mouse fibroblasts were acquired from ATCC (Manassas, VA) and cultured in Dulbecco's Modified Eagle Medium (ATCC) supplemented with 10% bovine calf serum (Hyclone, Santa Clara, CA) and 100 U/mL penicillin/streptomycin (Invitrogen, Carlsbad, CA). Cultures were maintained in a 5% CO_2 incubator at 37 °C and the culture media was changed every 2-3 days until cells reached confluence. Cells were detached with 0.25% trypsin (Invitrogen), seeded in 24-well plates in 1 mL culture medium, and allowed to grow for 24 hours (time required to reach confluence). In experiments with long-term cell cultures, this medium was replaced with fresh medium supplemented with bovine animal serum. In RT-PCR assays, after the 24 hour incubation, cells were treated in serum-free culture medium for 16 hours to arrest cell division. This medium was replaced with fresh serum-free medium before the start of a hypoxia assay.

Bubbling gas through a medium containing serum can cause proteins in the serum to denature.[42] Moreover, in our early experiments, bubbling through a serum containing media led to formation of foam at the

liquid surface. Sometimes, as the foam was building up, it rose to the level of the plug and started coming out through the vent hole, forcing a significant amount of the medium out of the well. The formation of foam was prevented by adding an anti-foaming agent (Antifoam A Concentrate from Sigma-Aldrich) at a concentration of 10 ppm. The anti-foaming agent did not have an observable effect on the viability of 3T6 cells grown in the wells, as assessed by propidium iodide exclusion and visual inspection (data not shown; see also Fig. 2-20).

Real-time PCR

The expression of selected hypoxia-related genes was determined by RT-PCR analysis. Following treatment, cells stored in RNAprotect® reagent (Qiagen, Valencia, CA) were detached from the 24-well bottoms by scraping with a rubber spatula, re-suspended in a cell-lysis buffer with 1% β-mercaptoethanol, and lysed by vortexing. Total RNA was extracted using a Clontech Nucleospin RNA II kit with on-column DNAase step (Macherey-Nagel, Bethlehem, PA). RNA quantity and RNA integrity number (RIN) was assessed with an Agilent 2100 Bioanalyzer and RNA chips (Agilent, Santa Clara, CA). cDNA was synthesized from total RNA using the Superscript III First Strand kit (Invitrogen), according to manufacturer's instructions. Briefly, 1 µg of RNA was annealed to 1 µL of OligodT at 65°C for 5 mins. cDNA was synthesized by cycling at 50 °C for

50 minutes, and 85 °C for 5 minutes. The reaction mixtures were treated with 1 µL RNase H at 37 °C for 20 minutes, and cDNA quantity and quality was verified using a ND-1000 spectrophotometer (Thermo Sci., Wilmington, DE).

For PCR amplification of cDNA, gene expression was quantified using a Power SYBR green PCR kit (Life Tech., Carlsbad, CA) according to manufacturer's instructions (Applied Biosystems, Foster City, CA). Briefly, 20 µL reaction mixtures were prepared, containing specific primers (1 µL each of fwd and rev primers), 1 µL of cDNA (1.5 µM) and the SYBR green master mix. Experiments were performed under the following conditions: 95 °C for 10 mins followed by 40 cycles of 95 °C/15 secs, 60 °C/60 secs, then 95 °C/15 secs, 60 °C/15 secs, and 95 °C/15 secs, on an AB 7600 RT-PCR machine (Life Tech.). Changes in gene expression in each sample were measured by comparing CT values to the housekeeping gene, GAPDH. Primers were obtained from ValueGene (San Diego, CA) and the oligonucleotide primer sequences used were as follows:

1. Hypoxia-inducible factor-1α (HIF-1α):

   fwd: CAGTCGACACAGCCTCGATA

   rev: CGGCTCATAACCCATCAACT

2. Urokinase plasminogen activator (uPA):

   fwd: TGGAAATGGTGACTCTTACCG

   rev: TAGGGTTTCTGAAGGACAGCA

3. Matrix metalloproteinase 2 (MMP-2):

    fwd: CCCCATGAAGCCTTGTTTACC

    rev: ACCTTGTAGGAGGTGCCCTGGAA

4. Matrix metalloproteinase 9 (MMP-9):

    fwd: AGACCAAGGGTACAGCCTGTTC

    rev: GGCACGCTGGAATGATCTAAG

5. GAPDH:

    fwd: ATGTTCCAGTATGACTCCACTCACG,

    rev: GAAGACACCAGTAGACTCCACGACA

Gene expression changes under hypoxic conditions were presented as the fold change relative to the [O_2] = 21% control on the same plate. Significance was assessed with an unpaired t-test. The criterion for statistical significance was a p-value < 0.05.

Results

Testing and calibration of the setup without cells

In all tests and live cell experiments with the setup, home-made humidifier bottles filled with water were connected in-line between the gas mixer and distribution strips. The passage (bubbling) of the gas mixtures through water was expected to humidify the mixtures to nearly 100%, thus reducing the evaporation of medium in the 24-well plate. Based on the above arguments on the penetration of O_2 from the atmosphere into a well

sealed by a plug, we expected that as the gas flow rate through a strip is increased, $[O_2]$ in the well approaches $[O_2]$ in the hypoxic gas mixture fed to the strip.[26,41] To find the magnitude of the gas flow rate through a plug, Q, providing a sufficiently close match between $[O_2]$ in the aqueous medium in the well and in the gas mixture, we fed pure N_2 to the strip and measured $[O_2]$ in the well as a function of Q.

To measure $[O_2]$, we used a 250 ppm solution of an oxygen-sensitive fluorescent dye, tris(2,2'-bipyridyl) ruthenium(II) chloride hexahydrate (RTDP), in phosphate buffered saline (PBS). ~1 mL of the solution was dispensed in a well, filling it to ~5 mm in depth. As previously discussed,[13,26] $[O_2]$ in an RTDP solution can be determined using the Stern-Volmer equation:

$$I_0 / I = 1 + K_q[O_2] \tag{2-4}$$

where K_q is the quenching coefficient of RTDP, I_0 is the intensity of fluorescence of the dye at zero oxygen, and I is the fluorescence intensity at the $[O_2]$ of interest. The value of K_q is temperature-dependent, and a convenient, practical way to find it is by measuring fluorescence intensities when the solution is saturated with air ($[O_2]$ = 20.9%), I_{air}, and pure N_2, I_0, and by using the equation $K_q = (I_0/I_{air} - 1)/20.9\%$. After the values of I_0 and I_{air} are found, $[O_2]$ can be calculated from measurements of fluorescence intensity, I, as

$$[O_2] = \frac{(I_0 / I - 1)}{K_q} = 20.9\% \cdot \frac{(I_0 / I - 1)}{(I_0 / I_{air} - 1)} \qquad (2\text{-}5)$$

The fluorescence of RTDP was measured with a Nikon TE-2000U inverted fluorescence microscope equipped with a stable LED fluorescence light source (~0.1% illumination intensity drift within 20 min)[26] and a Sony XCD-X700 digital camera. The RTDP solution was imaged near the bottom of a well with a 10x, NA = 0.25 objective. The fluorescence signal was found to be independent of the depth of the solution in the well, as long as the depth was greater than 300 μm. Therefore, the measured values of I were expected to reflect the level of $[O_2]$ near the bottom of the well, where adherent cells would be located.

Before the measurements of I versus Q were started, the value of I_{air} was measured by saturating the well with atmospheric air, and a putative value of I_0 was measured by setting the flow rate of N_2 to a relatively high level of 56 μL/s and allowing ~1.5 hr for equilibration (see Fig. 2-18 below for the relevant equilibration times). From these measurements, the value of K_q was calculated at ~2.35 (for 100% O_2), in good agreement with our previous measurements.[26,41] The equilibration time of ~1.5 hr was also used for other tested flow rates, Q. As expected, $[O_2]$ (calculated from I using eq. 2-5) was a decreasing function of Q (Fig. 2-17). Most importantly, for the data points with Q > 39 μL/s (excluding the 56 μL/s reference), the average value of $[O_2]$ was 0.35%, corresponding to an ~0.8% reduction in I

as compared to I_0, which was comparable with an estimated measurement error of ~0.5%. The error was greater than in our previous measurements of $[O_2]$ using fluorescence of RTDP in microfluidic devices[26,41] due to much longer time intervals between the measurements of fluorescence at the reference points (air and N_2) and test points (hours versus minutes). All subsequent experiments were performed at Q = 45 µL/s, corresponding to gas flow rates of 15 and 30 µL/s through the bubbling and headspace outlets, respectively. Taking into account the uncertainty of the actual $[O_2]$ at the putative I_0 reference point with Q = 56 µL/s, we estimated that when pure N_2 is fed to a strip at Q = 45 µL/s, it results in $[O_2] < 0.5\%$ in the wells. By extension, when a hypoxic gas mixture is fed to the strip, the actual $[O_2]$ in the wells (excluding the effects of cellular respiration) is expected to be <0.5% above $[O_2]$ in the gas phase.

In addition to the relation between the steady-state $[O_2]$ in the medium in the wells and the O_2 content and flow rate of the gas mixture, an important parameter of the setup is the time of equilibration of $[O_2]$ at the bottom of a well with $[O_2]$ in the gas mixture. The equilibration time was tested by filling a well with 1 mL of an aerated 250 ppm solution of RTDP in PBS, putting a gas distribution strip on top of the 24-well plate, starting a flow of N_2 through the strip, and taking fluorescence micrographs of the RTDP solution near the well bottom every 20 sec. Fluorescence intensity, I, measured at a given time point was converted

into $[O_2]$ at that time point using eq. 2-5, with I_{air} and I_0 taken to be, respectively, the fluorescence intensity before the flow of N_2 was started and after ~100 min of the N_2 flow (Fig. 2-18).

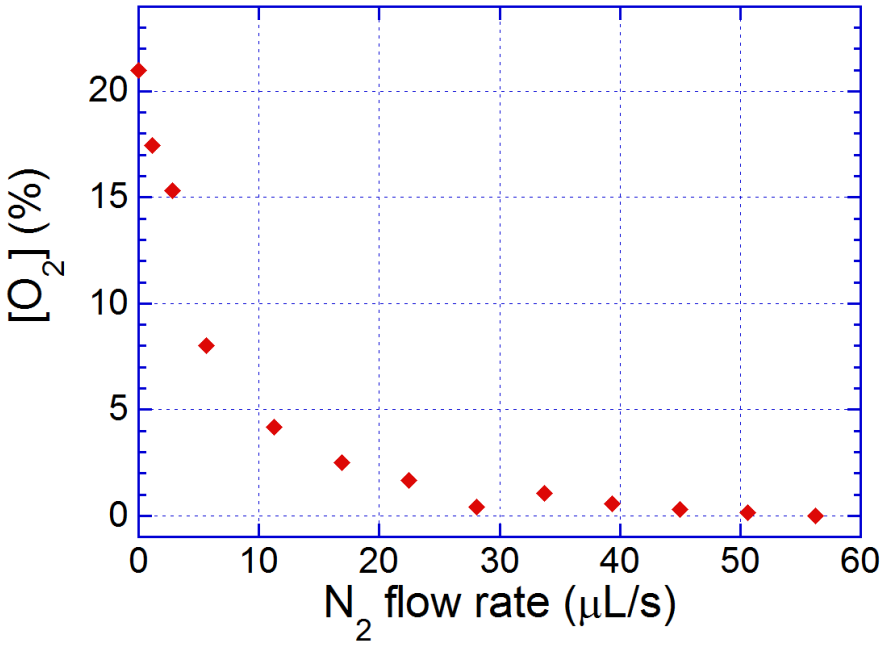

Figure 2-17: The concentration of oxygen, [O2], near the bottom of a well of a 24-well plate with 1 mL of RTDP solution, as a function of flow rate of N_2 through a plug inserted into the well. $[O_2]$ was estimated from measurements of fluorescence of RTDP. The N_2 flow was split 2:1 between the well headspace and bubbling through the medium.

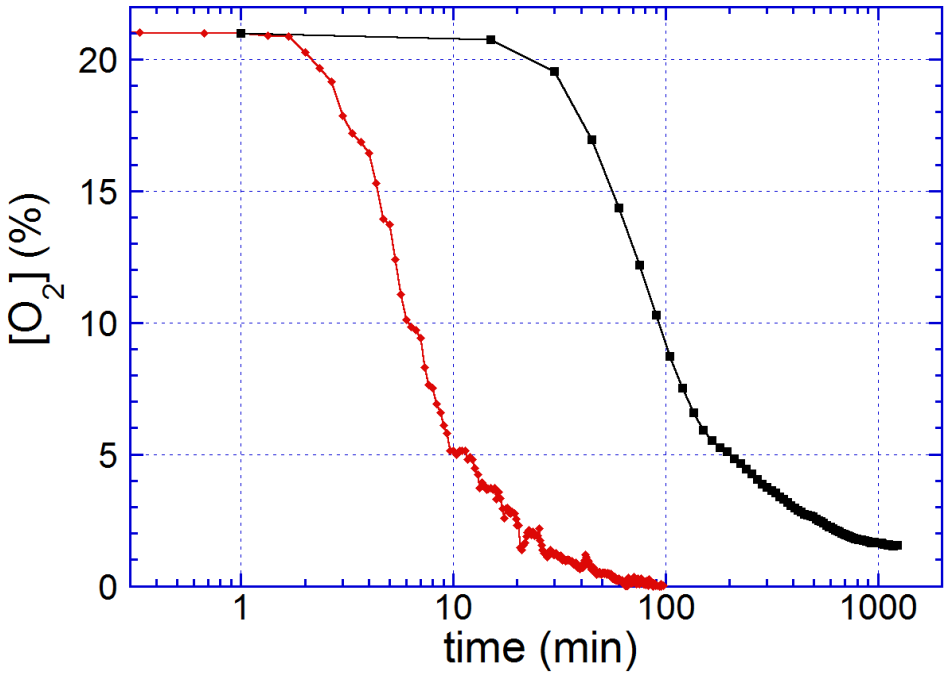

Figure 2-18: The concentration of oxygen, $[O_2]$, near the bottom of a well of a 24-well plate with 1 mL of RTDP solution, as a function of time after a 45 µL/s flow of N_2 is started through a gas strip attached to the plate. *Red symbols*: The plug inserted into the well has a capillary dipped into the medium, resulting in the bubbling of N_2 through the medium at ~15 µL/s. *Black symbols*: The plug does not have a capillary, and the entire flow of N_2 is directed to the well headspace.

As expected, because of the relatively low flow rate of N_2 (45 µL/s), considerable amounts of air dissolved in the PDMS plug (~0.35 mL) and present in the headspace (~0.5 mL), and the relatively large volume of solution in the well, $[O_2]$ at the well bottom responded to the initiation of the N_2 flow with a considerable delay. It took nearly 2.5 min for $[O_2]$ at the bottom to drop by 1/10, from 20.9 to 18.8%. Nevertheless, later on, the transition accelerated and was 9/10 complete (with $[O_2]$ decreasing to ~2.1%) after ~22 min. (We note that what is plotted as $[O_2] = 0$ in Fig. 2-18

may actually correspond to [O_2] as high as 0.5%, but this fact does not change the assessment of the transition time.) The air-to-N_2 transition test was repeated 7 times and the 1/10 to 9/10 transition time (from [O_2] = 18.7% to 2.1%) was 19.3 ± 1.6 min (mean ± SD). When the gas supplied to a strip was switched from N_2 to air, the transition from [O_2] = 0 to 20.9% near the well bottom occurred on the same time scale (2 tests performed; not shown). Importantly, the variability in the transition time was small, despite some variations in the depths of immersion of the capillaries and their lateral positions within the wells (resulting from differences in the shapes of the plugs, imperfect registration of the plugs with respect to the gas channels, and random tilts of the capillaries with respect to the vertical).

The transition experiments were repeated with the capillary removed from the plug, thus stopping the bubbling of the RTDP solution, while maintaining the same integral gas flow rate through the plug (Fig. 2-18). Without the bubbling, the saturation value of [O_2] at the bottom was measured at 1.5%, which could correspond to an actual [O_2] as high as 2%, given our ~0.5% measurement uncertainty. The value of [O_2] was substantially greater than zero due to relatively inefficient O_2 transport through the solution (that occurred by diffusion only) and appreciable O_2-permeability of the polystyrene bottom of the well and because, unlike in a hypoxic chamber (or glove box), the 24-well plate was surrounded by

atmospheric air. The O_2-permeability of polystyrene at room temperature is in a range of 600 – 800 nmol/(m·s·GPa),[43] whereas the O_2-permeability of water, calculated as a product of the O_2 solubility, 1.37 mol/(m^3·atm), and diffusivity, 2×10^{-9} m^2/s, is 2.74×10^4 nmol/(m·s·GPa). As the result the O_2 permeability of a 5 mm layer of the aqueous solution in the well is expected to be 8.6 – 11.4 times greater than the permeability of the 1.25 mm thick bottom of the well, leading to a steady-state $[O_2]$ = 1.7 – 2.2% at the well bottom, in agreement with our measurements.

The transition time, based on the 1/10 to 9/10 criterion, was 310 ± 20 min (average of 4 data points), with the initial 1/10 through the transition taking an additional ~30 min (Fig. 2-18), in agreement with previous reports.[33,34] That is, without the bubbling, the $[O_2]$ equilibration was ~15 times slower, and we expect the same long equilibration time for a 24-well plate placed into a hypoxic chamber without stirring. [33,34] Since the time of equilibration by diffusion is inversely proportional to the diffusion coefficient, D_w, the effect of the bubbling can be interpreted as an ~15-fold increase in the effective diffusion coefficient, $D_{eff} \approx 15\ D_w$. We note that for a 24-well plate placed into an anoxic chamber, the point of 9/10 through the transition corresponds to $[O_2]$ = 2.1%, which can be loosely considered as the onset of hypoxic conditions. Therefore, for a 5 mm layer of aqueous medium in a well, the use of bubbling shortens the hypoxia onset time from ~340 min (5.5 hrs) to ~22 min.

The flow caused by the bubbling was tested by filling a well with 1 mL of a suspension of 2 µm green fluorescent beads in a density-matching solution and tracking the motion of the beads under fluorescence illumination. The motion consisted of a relatively fast pulsatile component, which was synchronized with pinching off of the bubbles, and a relatively slow drift, which was likely caused by the convective flow leading to the accelerated transport of O_2. The pulsatile and mean flow velocity both increased with distance from the well bottom. At a distance of ~20 µm from the bottom, the peak and mean flow velocities were 140 and 20 µm/s, respectively. These velocities corresponded to peak and mean shear stresses of 0.07 and 0.01 dyne/cm^2, respectively, at the well bottom, both too low to cause appreciable mechanical perturbation of cultured adherent cells.

Because the setup was designed for long-term experiments, it was important to minimize the evaporation of medium from the wells. At a temperature of 37 °C, typical for mammalian cell cultures, the density of saturated water vapors is ~44 mg/L. Therefore, continuous flow of dry gas through a well at Q = 45 µL/sec, totaling ~4 L per day, is expected to lead to evaporation of 175 µg of medium or 17.5% of its original amount in the well within a day. In a preliminary experiment, with the 24-well plate in a 37 °C incubator, the gas strip was fed with non-humidified gas, and the evaporation from wells after 18 hours was measured at 133 ± 33 µL, in

good agreement with the theoretical prediction. When the gas mixture fed to the strip was bubbled through a water-filled humidifier bottle, which was held at the same 37 °C temperature, the evaporation was reduced to 55 ± 15 μL over the 18 hour time interval, rendering multi-day hypoxia assays substantially more practical. One of the factors causing the residual evaporation was likely the high water-vapor permeability of PDMS (~60 times higher than its O_2 permeability), causing substantial diffusion of water vapors through the 1 mm layer of PDMS above the channels in the gas distribution strip.

Measurements of oxygen concentration in long-term cell cultures

To measure [O_2] *in-situ*, around 3T6 mouse fibroblasts plated at the bottom of a well, we used OxoDish® 24-well plates and SensorDish Reader (PreSens, GmbH, Regensburg, Germany). The OxoDish® 24-well plates contain an [O_2]-sensitive spot at the bottom of each well, and the response of the spot is read out by the SensorDish Reader through the transparent bottom of the well. 3T6 mouse fibroblasts were plated at a low cell density (~10,000 cells/mL) into a row of 4 wells and at a high density (~40,000 cells/mL) into another row of 4 wells. The 24-well plate was placed into a 37 ºC, 5% CO_2 incubator to allow cells to adhere and spread. Before the experiment, the medium in each well was exchanged with 1 mL of fresh medium containing 10 ppm of the anti-foam agent. In addition to the two

rows of wells with cells, medium was also added into a row of 4 wells without cells, also at 1 mL per well.

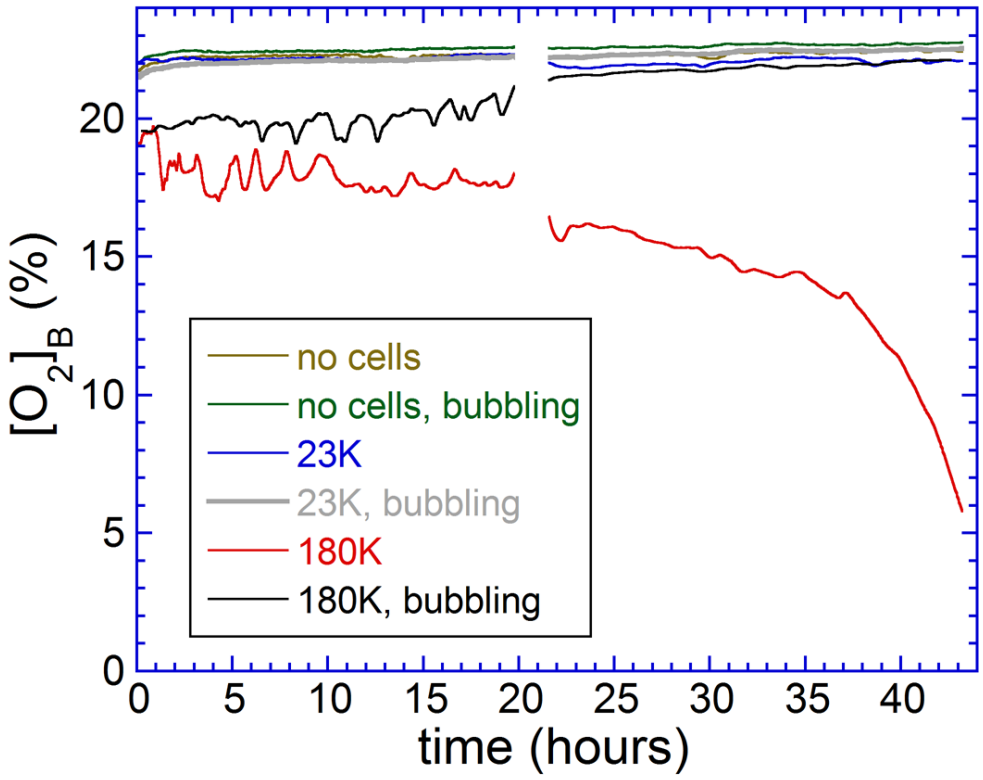

Figure 2-19: The concentration of oxygen, $[O_2]$, at the bottoms of wells of a 24-well plate versus time in a long-term culture assay with gas distribution strips attached to the plate. There were wells with two different densities of 3T6 mouse fibroblasts on the bottoms and wells without cells (no cells). There were four wells at each cell density, two with and two without bubbling of gas (air with 5% CO_2) through the medium. The two cell densities, as evaluated at the end of the assay, were 23,000 cells/cm^2 (23K) and 180,000 cells/cm^2 (180K) on average. The plotted values of $[O_2]$ are averages between two wells at the corresponding sets of conditions (n = 2).

Three gas distribution strips were attached to the plate, covering the wells with media inside. The strips were modified by removing the capillaries from every other plug, so only two wells in a row had gas bubbling through the medium, whereas the other two wells had the entire gas flow directed to the headspace. The 24-well plate with the gas strips was mounted on the reader and placed into a 37 ºC incubator. Air with 5% CO_2 (emulating the atmosphere in a regular cell incubator) was fed to all three gas strips, and [O_2] at the bottom of all 12 wells was recorded in parallel for ~44 hrs (Fig. 2-19). At ~20 hrs, the 24-well plate was briefly placed on a microscope equipped with a 37 ºC environmental chamber to visually check the viability of cells (the gap in the curves of Fig. 2-19). After the 44 hr assay, the viability and density of cells were evaluated under a microscope again. Cells in all wells had typical fibroblast-like morphology, maintained process extension and cell-to-cell connections, and were evenly distributed over the substrate, indicating good cell viability (Fig. 2-20). The cell density was evaluated by taking micrographs of random regions of wells, counting the numbers of cells in these regions, and dividing the numbers by the area of the field of view. In the 4 wells with cells plated at a low density, the post-assay cell density was measured at 23,000 ± 11,000 cells/cm^2 (mean ± SD), whereas in the 4 wells where cells were plated at a high density, the post-assay density was measured at 180,000 ± 20,000 cells/cm^2.

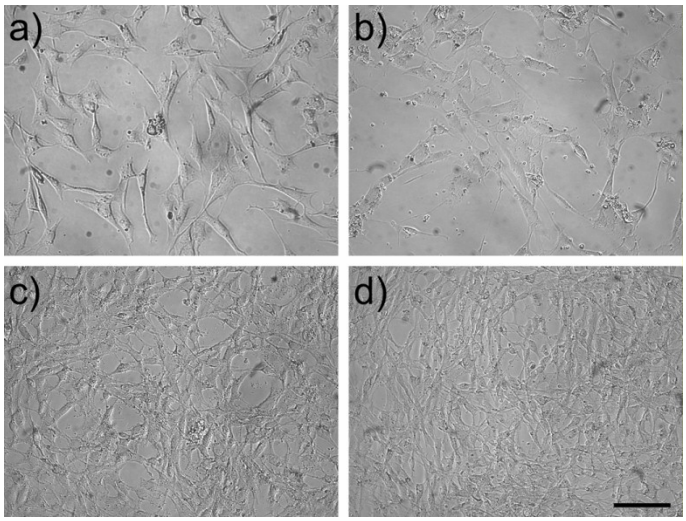

Figure 2-20: Representative bright field micrographs of 3T6 mouse fibroblasts taken in different wells of a 24-well plate after a 44 hr assay with the gas distribution strips attached to the plate and air with 5% CO_2 perfused through the strips. (a) and (b) wells with an average cell density of 23,000 cells/cm^2 without and with the bubbling, respectively. (c) and (d) wells with an average cell density of 180,000 cells/cm^2 without and with the bubbling, respectively. Scale bar = 100 µm.

The dependences of $[O_2]$ at the bottom of the wells on time (Fig. 2-19) show that $[O_2]$ remains nearly constant and at about the same level in the wells without cells and in the wells with the final cell density of 23,000 cells/cm^2. This level is measured at ~22.5% likely due to imperfect calibration of the O_2-sensing setup. In contrast, $[O_2]$ in the wells with 180,000 cells/cm^2 without bubbling is substantially below 20% during the entire assay and, towards the end of the assay, $[O_2]$ decreases to ~6%, which is ~16% lower than in the other wells. As argued in the Introduction, at a given cell respiration rate, the difference between $[O_2]$ in the atmosphere above the medium and around cells, $\Delta[O_2] = [O_2]_T - [O_2]_B$,

is expected to be proportional to the density of cells in the well, explaining the much lower [O_2] at 180,000 cells/cm^2 as compared to that at 23,000 cells/cm^2. The gradual decline of [O_2] in the wells without bubbling that end up at 180,000 cells/cm^2 can be explained by the increasing consumption of O_2 caused by proliferation of cells. These results are in good agreement with previous measurements using the same PreSens setup with mouse embryonic fibroblasts (MEF; primary cells) plated in a 24-well plate with the same amount of media in the wells (1 mL).[34] When the 24-well plate was placed into an [O_2] = 19% incubator, at 10 hours through an assay, [O_2] around MEF cells plated at 10,000, 33,000, and 100,000 cells/cm^2 was measured, respectively, at 1, 3, and 10% below [O_2] in the atmosphere.[34] Extrapolating these results to a density of 180,000 cells/cm^2, one would expect Δ[O_2] = 18%, which is very close to the value of 16% that we measured. Relatively high [O_2]$_B$ without bubbling at 23,000 cells/cm^2, <1% below [O_2] without cells in our experiments (while one could expect 1-2% below [O_2] without cells at 32-44 hrs), could be due to the system's limited precision (nominally, ±1%) and some differences in the metabolism of the 3T6 cells at low and high densities.

Most importantly, the results in Fig. 2-19 indicate that the application of bubbling nearly completely eliminates the respiration-induced depletion of O_2 in the wells with 180,000 cell/cm^2. As argued above, the results of the transition experiment (Fig. 2-18) can be

interpreted as an ~15-fold increase of the effective diffusion coefficient due to the bubbling, $D_{eff} \approx 15\ D_w$. Eq. 2-3 suggests that a given diffusive flux of O_2 through the medium, J, as required to compensate for the cellular respiration, is maintained at a 15-times smaller concentration difference, $\Delta[O_2] = [O_2]_T - [O_2]_B$, if D_{eff} is used instead of D_w. Given $\Delta[O_2]$ = 16% at 44 hrs for 180,000 cells/cm^2 without bubbling, one could expect $\Delta[O_2] \approx 1\%$ with the bubbling, and this value was consistent with the experimental results in Fig. 2-19 (again, given the ±1% precision of the system). The benefit provided by the bubbling, the maintenance of $[O_2]$ in the medium around cells close to $[O_2]$ in the gas mixture, even at high cell densities, should be particularly valuable for gas mixtures intended to create normoxic or hypoxic conditions, with $[O_2]$ substantially below 21%. In these cases, a high initial cell density or proliferation of cells during the course of an assay can readily lead to an increase of $\Delta[O_2]$ to the point that the medium around the cells becomes anoxic.[34] (Our attempt to perform an experiment using a triple gas mixture with $[O_2]$ = 6% produced inconsistent results, likely because of the relatively low resolution of the setup.)

Finally, we note that in addition to the efficient O_2 transport (Fig. 2-18), the convective flow generated by the bubbling likely resulted in a substantially more uniform distribution of nutrients and metabolites in the medium, improving the composition of the medium around cells.

Specifically, for bovine serum albumin (BSA) with a diffusion coefficient D_s ≈ 60 μm²/s, taken as a representative of macromolecular nutrients contained in the serum, the time of equilibration of concentration by diffusion across a 5 mm medium layer is $\tau_s = h^2/(2D_s) \approx 58$ hrs. This long equilibration time suggests that the depletion of macromolecular nutrients at the well bottom, where they are consumed or degraded by cells, may be substantially greater than the depletion of nutrients averaged over the entire volume of the medium. If, for example, the average depletion of BSA is 50% over 48 hrs, the depletion at the bottom is nearly 90% (results of a numerical simulation). Conversely, an increase in the effective diffusion coefficient by a factor of 15 due to bubbling, would make the concentration of BSA at the bottom practically the same as its average concentration (47.5% versus 50%), thus increasing the BSA concentration around cells more than four-fold. (The difference between concentration distributions with and without bubbling is less extreme for substances with higher diffusion coefficients, such as low-molecular-weight nutrients, and for lower consumption rates, which are expected at reduced cell densities.)

Measurements of gene expression under hypoxia by real-time PCR

To test the effect of hypoxia on gene expression, 3T6 mouse fibroblasts were plated in all wells of a 24-well plate at a density of 100,000 cells/well, with 1 mL of culture medium in each well. Six gas-

distribution strips were attached to the 24-well plate and connected to the gas mixer, which supplied O_2-N_2-CO_2 mixtures with 0, 1, 2, 3, 4, and 21% O_2 to different strips. All six mixtures contained 5% CO_2, and gas was bubbled through the medium in all 24 wells of the plate. After 4 hrs in a 37 °C incubator, ~900 μL of culture media was aspirated from each well through the venting hole in the plug using a gauge 27 syringe needle, without stopping the gas flow, and 4 volumes of RNAprotect® reagent (Qiagen, Valencia, CA) were dispensed into the well immediately thereafter. This procedure of addition of RNAprotect, a reagent providing immediate stabilization of mRNA in cells, minimized the exposure of cells in the wells to the atmospheric oxygen. Therefore, the stabilized mRNA content, which was subsequently analyzed) was expected to be unchanged from the respective hypoxic conditions in the wells. After RNAprotect was added to all wells, the gas flow was stopped, and the gas strips were disconnected from the plate. The 24-well plate was stored at 4°C for ~24 hours, at which time an RT-PCR assay was performed.

The number of cells recovered from a well was sufficient to test changes in the expression of a single gene with good precision. Therefore, the levels of expression of 4 genes were tested at each [O_2]. These genes were chosen specifically because they were all known to be involved in cells' hypoxic responses, their transcriptional changes during hypoxia had been previously studied in fibroblasts, and their transcriptional responses

to hypoxia were known to be different. HIF-1α protein is quickly degraded during normoxia and is stabilized during hypoxia, and the activity of HIF-1α during hypoxia induces numerous secondary effects.[44,45] Nevertheless, because the hypoxia-induced regulation of HIF-1α is post-translational, its mRNA expression level is not expected to be appreciably changed by hypoxia.[46] In contrast, transcription of urokinase-type plasminogen activator (uPA), which is an inducer of fibrinolysis (the process by which blood clots are broken down), is inhibited by hypoxia.[47] Therefore, hypoxia is expected to reduce the level of uPA mRNA.[47] The other two genes we analyzed were matrix metalloproteinases (MMP2 and MMP9), whose expression is up-regulated during hypoxia.[48,49] These proteinases break down the extracellular matrix, including basement membranes, allowing cells to migrate through underlying tissues and begin vascularization.[49,50]

The results of the real-time PCR assay (Fig. 2-21) agreed with results of the previous studies examining the hypoxia-related changes to these specific genes in 3T6 cells. The level of expression of HIF-1α was the same at all [O_2], whereas the expression of uPA was significantly downregulated, and the expression of both MMP2 and MMP9 was upregulated at all 5 reduced levels of [O_2]. Nevertheless, somewhat unexpectedly, there was no significant difference between the levels of mRNA for uPA, MMP2, or MMP9 between [O_2] = 0, 1, 2, 3, and 4%. It is worth noting, however, that as discussed above, the actual values of [O_2]

around cells might have been up to 0.5% greater, and the medium was likely never completely anoxic. Most importantly, the results of the assay demonstrated that the proposed experimental setup enables comparing the levels of expression of 4 different genes at 6 different levels of [O_2] in a single assay.

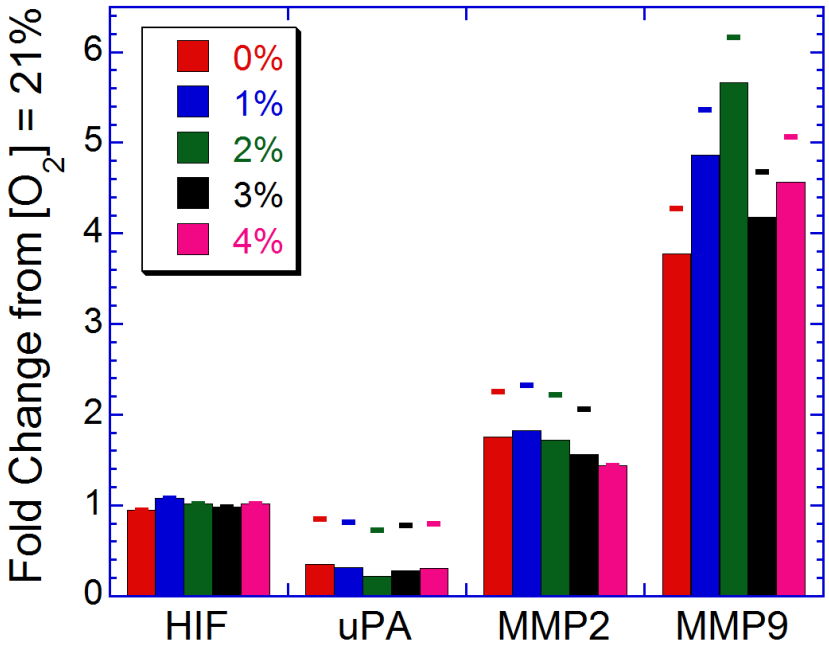

Figure 2-21: Fold change in the level of expression of hypoxia-related genes HIF-1α (HIF), uPA, MMP2, and MMP9 in 3T6 mouse fibroblasts after 4 hrs of incubation at [O_2] = 0, 1, 2, 3, and 4%, as compared with their expression at [O_2] = 21% (fold change in GAPDH mRNA), as measured by real-time PCR. Dashes (-) indicate data points with significant change from the [O_2] = 21% control, as assessed with an unpaired t-test ($p < 0.05$).

Discussion and Conclusions

The proposed experimental system, consisting of a computer-controlled, multi-channel gas mixer and microfabricated gas distribution

strips, makes it possible to generate a set of 6 different [O_2] levels in a standard 24-well plate, with 4 separate wells at each [O_2]. The system has been used to test the levels of expression of 4 different genes in mammalian cells exposed to 6 different [O_2] in a single assay. The capacity of the proposed system to test cellular responses to a range of [O_2] using two standard gas mixtures (5% CO_2 balanced with air and 5% CO_2 balanced with N_2) is unique and brings a new level of flexibility to hypoxia research. Importantly, the proposed system is relatively simple and inexpensive. It does not require specialized bulky infrastructure (such as hypoxia chambers or glove boxes), enables performing cell culture experiments at user-defined [O_2] anywhere in the range between 0.5 and 21% without purchasing specially formulated triple gas mixtures (O_2-N_2-CO_2), and consumes only ~0.5 cubic feet of the standard gas mixtures for one value of [O_2] per day. Another advantage of the proposed system over simple hypoxic incubators (but not glove boxes) is the possibility of changing cell culture medium by the aspiration and dispensing through the venting hole in the plug, without exposing cells to atmospheric air. This way, fresh medium can be added, cells can be fixed or lysed, and RNA and DNA content can be stabilized using special reagents, all without potentially confounding reoxygenation errors. Specifically, the proposed system is suitable for immunohistochemical analysis of protein changes following fixation of cells by dispensing 4% paraformaldehyde through the

venting hole in the plug. If the gas-distribution strips are put on a 24-well plate with cover-glass bottoms (commercially available from MatTek Corp., Ashland, MA), the proposed system becomes compatible with high-resolution time-lapse microscopy of cells at hypoxic conditions.

The hypoxia inception time provided by the system can likely be further reduced, and the lowest achievable [O_2] in the wells further lowered, by increasing the rates of bubbling and of the flow of gas through the well headspaces. Two shortcomings of the proposed system – the suspected presence of residual O_2 in the medium, when the strips are perfused with pure N_2, and appreciable evaporation during long-term assays – are likely connected to the diffusion of O_2 and water vapors through the 1 mm layer of PDMS sealing the channels in the gas distribution strip. Therefore, the performance of the system would likely be improved by making this layer gas-impermeable, e.g., by coating it with a thin layer of parylene.[51] Another possibility would be to machine the gas distribution strips from a hard plastic (while keeping the soft PDMS plugs), potentially making the system suitable for commercial production.

The proposed system has several advantages over the setup in which the O_2-content in a 6-well plate is controlled using gas-permeable PDMS plugs perfused with different gas mixtures and dipped into the medium in the wells.[40] A hypoxia inception time of 22 min is achieved with a 5 mm medium layer, as compared with the ~1 mm layer in Ref. 40, thus

allowing longer assays with higher cell densities, while diminishing the effects of the medium's evaporation. In addition, the accessibility of medium through the venting hole in the plug in the proposed setup makes it easy to exchange the medium in the course of an experiment, including the addition of various stabilizing and fixing agents. Furthermore, the use of capillaries dipped into medium in the wells minimizes the contact between the gas distribution strips and the medium, making it simple to attach the strips to a plate, avoiding any possible absorption of the medium into the porous material of the plugs, and simplifying cleaning and sterilization. Finally, the operation of the gas distribution strips together with the multichannel gas mixer enables increased flexibility and experimental throughput.

Experiments with the proposed system highlighted an important problem in the application of standard hypoxic chambers and incubators to cultures of adherent cells. With nearly uniform temperature and almost 100% humidity, which are common to hypoxic incubators, spontaneous convection in culture dishes is not likely to occur. Therefore, if the dishes are not shaken, the transport of oxygen between the incubator atmosphere, where a desired [O_2] is maintained, and the chamber bottom, where O_2 is consumed by cellular respiration and a low [O_2] needs to be imposed and maintained, occurs by molecular diffusion only. The diffusive transport may be sufficiently fast if the thickness of the medium layer is small (~1

mm). However, because of the relatively low diffusivity and solubility of O_2 in water, for more commonly used medium layers of ~5 mm thickness, the transport is slow. As a result, when a culture dish with an aerated medium is placed into a hypoxic incubator, it is likely to take 5 – 10 hours before cells at the bottom of the dish are exposed to hypoxia (Fig. 2-18 and Refs. 33 and 34). Moreover, at a high cell density, [O_2] around cells can be substantially lower than [O_2] in the incubator atmosphere (Fig. 2-19 and Ref. 34). This unwanted effect is exacerbated as cells proliferate, and it can easily lead, without the knowledge of the operator, to the exposure of cells to hypoxia or anoxia, even with a normoxic atmosphere.

Both negative effects of the slow transport of O_2 through the medium are alleviated by the proposed gas distribution strips. The bubbling of gas through the medium substantially accelerates the rate of O_2 transport, reducing the time of hypoxia inception ~15-fold (to ~22 min). The bubbling also reduces, likely by a similar factor, the difference between [O_2] in the gas phase and around the cells, thus making it possible to culture cells at up to 15-times higher densities and control [O_2] around the cells with 15-times higher precision at a given cell density. Importantly, the bubbling is performed at a slow gas flow rate of ~15 μL/sec, resulting in minimal mechanical perturbations to the cells (peak shear stress of 0.07 dyne/cm^2) and no loss of cell viability. In fact, the convective flow produced by the bubbling is expected to result in a higher

uniformity of the medium over the volume of the well and in improved medium composition around cells at the bottom (more nutrients and fewer metabolites). In addition, continuous mixing of the medium in the wells makes the proposed system potentially useful for experiments on planktonic cells.

The proposed system can be used in a variety of laboratory experiments, where adherent cells need to be cultured at well-defined oxygen tensions, including hyperoxia, normoxia, hypoxia, and anoxia. The compact size of the system and the minimal number and amount of gas mixtures required to perform hypoxia and normoxia assays make the system appealing to researchers whose main focus is outside hypoxia and O_2-control. The compatibility of the system with real-time high-resolution microscopy under O_2-controlled conditions and the possibilities of selecting any desired O_2 concentrations and running parallel assays at multiple [O_2] make the system a powerful tool for specialized hypoxia research.

Chapter 2.3, in full, is in preparation for publication as "Precise control of oxygen concentration in 24-well cell culture plates for hypoxia studies", Polinkovsky, Mark*; Pamenter, Matthew*; Haddad, Gabriel; and Groisman, Alex. The dissertation author is a co-first author and a leading contributor to this paper.

Chapter 3: Bi-directional Temperature Jump System to Study Fast Protein Folding Kinetics

3.1: Microfluidic Device and Temperature Jump System

Introduction

Temperature shifts are known to induce conformation changes in proteins and other biomolecules. Consequently, laser temperature jumps (T-jumps) have been employed to rapidly heat molecules and observe the effects. The advantage of this method is that the temperature change occurs on a faster time scale than the molecule's kinetic response, allowing the molecule's conformational kinetics to be observed at the new temperature. Furthermore, the laser T-jump apparatus can be coupled with a fluorescence excitation light source to use Förster resonance energy transfer (FRET) to monitor changes in the biomolecule's conformation over time.

The laser heating pulses can be as short as nanoseconds, although the short duration of the pulse typically limits the temperature jump to ~10 °C. At the same time, cooling the sample is limited by the thermodynamic properties of the sample's environment.[1-3] Therefore, observations of transitions from high temperatures to low temperatures have been limited to hundreds of microseconds – orders of magnitude

slower than the resolution of the heating transition. This presents a challenge for observing events such as biomolecules refolding into their native states after unfolding during a heating pulse.

Under normal conditions, biomolecules are in their native conformations at biological temperatures (25 to 37 °C) and unfold when the temperature increases. Thus, a T-jump experiment would be useful for measuring protein unfolding kinetics at microsecond (and faster) timescales. However, the folding transition is often of interest, and the T-jump technique has to be modified for this task. Ordinarily, either acid denaturation[2] or cold denaturation is used, with the protein unfolded in a solution with a high denaturant concentration (6 M Guanidinium chloride), at low temperature (~0 °C).[4,5] In these conditions, a laser T-jump pulse induces the protein to fold, and the folding behavior can be observed. Yet, this is not ideal either, as the non-native environment around the protein may affect the folding landscape, and consequently, the kinetics.[5] A more realistic measurement would employ a fast laser T-jump from room temperature, in a biologically relevant buffer, to unfold the protein at high temperatures (> 60 °C). Then, the sample would be re-cooled to biological temperatures in microseconds so that the protein's refolding can be observed. The advantage of this approach lies in its ability to provide information both on the unfolding and refolding of the protein, in the protein's natural environment, and with resolution down to microseconds

accessible in both directions. However, in order to utilize this method, the cooling time of the sample must be decreased by several orders of magnitude. Here, we present a laser T-jump system (Fig. 3-1 a) that provides both heating and cooling with a characteristic time of one microsecond through the use of microfluidics and substrates with favorable thermodynamic properties. In Section 3.2, we will describe experiments with DNA hairpins to investigate their folding and unfolding kinetics in various salt concentrations, at these previously inaccessible time scales.

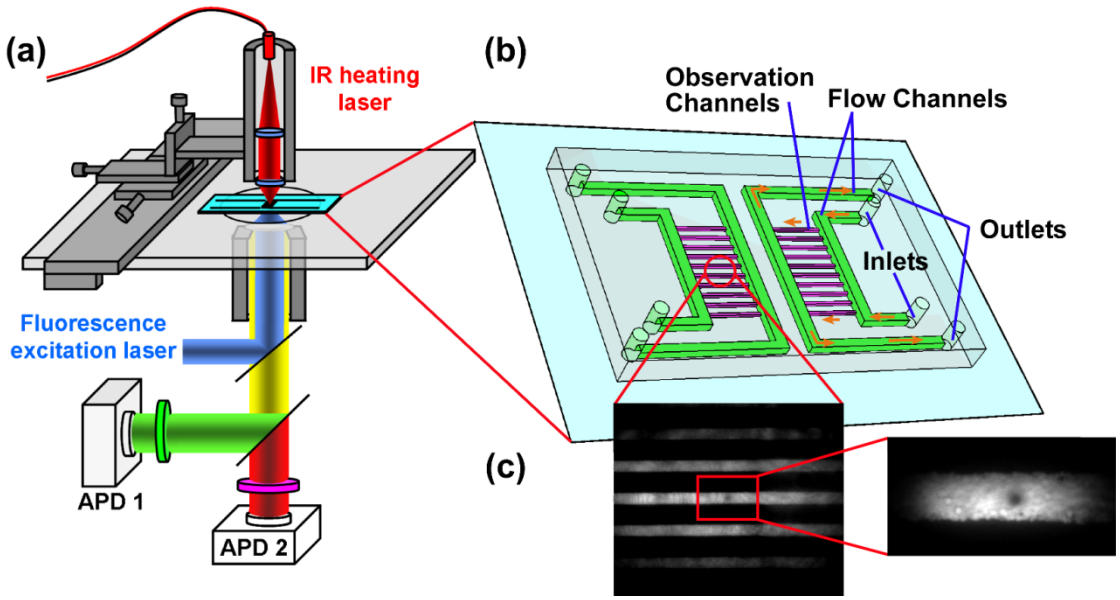

Figure 3-1: Diagram of T-jump setup and microfluidic device. (a) Schematic of the microfluidic device on the FRET setup, with the IR laser heating a spot from above. (b) The microfluidic device (channels not to scale). The flow channels are in green and the observation channels are in purple. Orange arrows indicate the direction of the sample flow. (c) A detailed snapshot of the IR laser heating HPTS dye in a 700 nm deep channel. The laser spot is 2 μm wide in a 5 μm wide channel.

Experimental

Device design and fabrication

Our device (Fig. 3-1 b) is cast in polydimethylsiloxane (PDMS), from a two-layer mold made on a silicon wafer using contact photolithography. The PDMS chip is sealed against a substrate to form the channels. Ordinarily, that substrate is a glass cover slip, which allows FRET measurements to be taken using an inverted epi-fluorescence microscope. To decrease the cooling time, however, a different substrate is necessary. Glass has a thermal conductivity of 1 W/(m·K), while quartz has a conductivity of 7 W/(m·K) and sapphire (aluminum oxide) has a conductivity of 30 W/(m·K).[6] Moreover, both sapphire and quartz are transparent at optical wavelengths and are available as cover slips. The optimal depth of the observation channels was found using time-dependent finite element simulations in COMSOL Multiphysics, with the main criteria being the characteristic cooling time of < 1 μs and a uniform temperature distribution throughout the depth of the channel. From the simulations, we found that 400 nm deep channels were optimal. Although we used 400 nm deep channels for our initial testing and characterization, their extremely small height complicated the fabrication process. Consequently, we used channels that are between 700 and 750 nm for our experiments with DNA hairpins, as these are more resistant to collapse,

are easier to work with, and still provide us with a cooling characteristic time under 2 μs.

The final consideration of the device design is to heat a small sample volume efficiently and quickly. Most standard T-jump systems use a Q-switched Nd-YAG laser with an IR wavelength near 1540 nm, corresponding to an absorption band for water.[1-3] However, this requires a significant volume of sample to absorb the laser light, which in turn limits cooling to hundreds of microseconds. Our device cannot utilize this water absorption band to heat the sample directly, as the observation channels are too shallow to absorb an appreciable amount of the laser power. Instead, we chose to use inexpensive near infrared (IR) diode lasers with a 980 nm wavelength, which are commonly available for optical communications purposes. The optical laser power was 200 – 400 mW, depending on the laser used, and all were powerful enough to boil the sample in the observation channels. Lasers at nearby wavelengths (such as 1064 nm) are also available and would be just as effective. Light at these wavelengths is not efficiently absorbed by our substrates, PDMS, or the sample. Therefore, we used sputter deposition to coat the sapphire substrate with a 20 to 25 nm layer of gold to absorb the IR laser radiation at the bottom of the channel and heat the sample above it.

The device design is centered on the sample observation channels, with large flow channels around them to provide a constant flow of fresh

sample. The observation channels (purple channels in Fig. 3-1 b) have a depth between 400 and 750 nm, depending on the device, and have varying widths between 5 and 10 μm on each device. In contrast, the flow channels, shown in green, (20 μm deep × 100 μm wide), are used as sources and sinks of the sample for the observation channels. The depth of the observation channels constrains the heated volume, significantly affecting the time needed to heat and cool the sample. The flow channels are designed to simplify the filling of the device with sample, with an inlet and outlet port on each side of the observation channels. Finally, each chip has two identical devices on it.

Description of System and Data Acquisition Control

The IR laser light is fed from the diode through an optical fiber and focused optically to a 2 μm diameter spot. The gold coating absorbs approximately 40% of the IR laser light, a large fraction of which is deposited in a fluid volume of 1.5 to 2.5 fL in the channel above. With this amount of concentrated power deposition, we have observed boiling at the location of the laser spot, meaning that we have the capability to perform temperature jumps from 25 °C to above 90 °C, a change that is five times higher than traditional temperature jumps,[1-3] with inexpensive, commercially available laser diodes.

We have developed two methods for obtaining data with 100 ns time resolution, depending on the detection requirements. For biological FRET data, we used a single-molecule FRET setup with avalanche photodiodes (APDs) as the detector, as described previously.[7] However, if spatial resolution was required, such as for the device characterization with dye, we used a different setup with a cooled CCD camera (Cooke SensiCam QE). In both cases, the device is mounted on an inverted epi-fluorescence microscope (Zeiss Axiovert 200 or Nikon TE300, respectively) with a blue (477 nm wavelength) laser as the excitation light source (Fig. 3-1 a). The IR heating laser is attached to the microscope stage above the device and is focused onto the gold at the bottom surface of the channel, just below the observed sample volume. The fluorescence emission signal is then output to the appropriate detectors. In both cases, we have to synchronize multiple control signals – the IR laser, the detectors, and for the CCD detection, the excitation laser signal. All of these have pulses of varying lengths, and recurring at different periods. The two systems diverge in their control schemes, and we will consider the CCD setup first.

The IR laser can be modulated directly through a custom-built control box (UCSD Physics Electronics Shop) by a TTL signal. The on and off time of the laser is in tens of nanoseconds, below our time resolution. The CCD camera can be controlled directly by its computer interface card, but its frame rate is several orders of magnitude slower than the required

time resolution. So, the solution is to modulate the excitation laser signal, ensuring that the CCD only picks up a fluorescence signal when the excitation laser light illuminates the sample. However, to maintain a uniform excitation light intensity, the excitation laser should not be switched on and off. Instead, an acousto-optic modulator (AOM) (from Crystal Technology, Inc.) is introduced into the excitation beam, and controlled with a TTL signal. The AOM has a switching time of 20 ns, also below the experimental time resolution. All of these components are controlled through a custom-built LabView (National Instruments) program interfacing with a National Instruments PCI-6111 Data Acquisition computer interface card (DAQ). The limit of our temporal resolution is 100 ns, twice the time corresponding to the 20 MHz clock rate of the card. The signal from each period of the IR heating is very low, so it must be integrated over many periods. Thus, the CCD camera exposure is set to be the length of thousands of T-jump cycles. The AOM signal is set to the same period as the IR laser, but the on-time can vary depending on the desired temporal resolution. In this way, the CCD exposure captures the fluorescence during a specific part of the IR heating cycle. After this data is taken, the AOM pulse is shifted by one time step and another exposure is acquired. In this way, exposures from all points of the T-jump cycle are acquired, each averaged over thousands of cycles. To increase the signal

level at each time step, the CCD exposure time is increased, allowing data acquisition over more cycles.

When we switch to the single-molecule FRET setup, the data acquisition scheme needs to be modified. We now use a National Instruments PCI-6602 Timing computer interface card, since we need more timers for synchronization and control than in the previous configuration. Here, the IR laser is still controlled by a TTL signal fed to the control box. But now, our detectors, the APDs, can be gated very quickly, so there is no need to modulate the excitation laser signal. Instead, we can provide gating pulses to the APDs, again with a TTL signal. However, there is a bottleneck in transferring the data from the APDs' buffers to the computer. We can take data over short periods but need at least 500 ns of dead-time between samples for the buffers to be read and cleared. Therefore, the APDs are set to take data over 100 ns windows, with a 900 ns off time before the next sample. This 1 μs period of APD acquisition is stepped by 100 ns in every IR heating cycle, ensuring that the APDs collect data from the same point in the IR period after 10 iterations. At the same time, in those 10 cycles, they collect data in every 100 ns window of the IR cycle. The stepping is done by making the IR period 100 ns shorter than a full integral number of microseconds, so the APD cycle and IR cycle slide by 100 ns relative to each other after each IR

cycle. Once the data is collected, a MATLAB routine is used to realign and sum the data from the corresponding time points of the IR cycle.

Temperature Calibration

By using the CCD camera setup, we can get spatial information on the IR laser spot heating the sample. Moreover, we can characterize the temperature jump by using a pH sensitive dye, 8-Hydroxypyrene-1,3,6-trisulfonic acid (HPTS), in Tris buffer, which is known to change its pH in response to temperature. HPTS has a fluorescence emission peak wavelength of 514 nm, while the excitation peak is very different for the acid (405 nm) and base (470 nm) forms of the molecule.[8] Since HPTS has a pKa of 7.3, the two populations will coexist in sizable fractions in the pH range of the solution as the temperature is increased from 25 °C, where the Tris buffer starts at a pH of 8, and decreases with temperature. By exciting the HPTS with a 455 nm blue laser, the fluorescence contribution from the acid state can be removed, and the response to the decreasing pH with temperature can be directly observed as a decreasing fluorescence intensity. Thus, dye fluorescence as a function of temperature was measured by using two separate devices, both filled with HPTS dye at a concentration of 200 μM (Fig. 3-2).

The first is a device designed for measuring bacterial thermotaxis.[9] Water circulators were connected to the two side channels, and water at a

desired temperature flowed through both channels, imposing that temperature on the thermotaxis channel between them, which was filled with HPTS dye. The second device was essentially the same as the one used for the T-jump measurements, with an additional layer containing a large flow-through fluid channel above the 400 nm deep observation channels. This large channel was connected to a water circulator that imposed the desired temperature on the observation channels below.

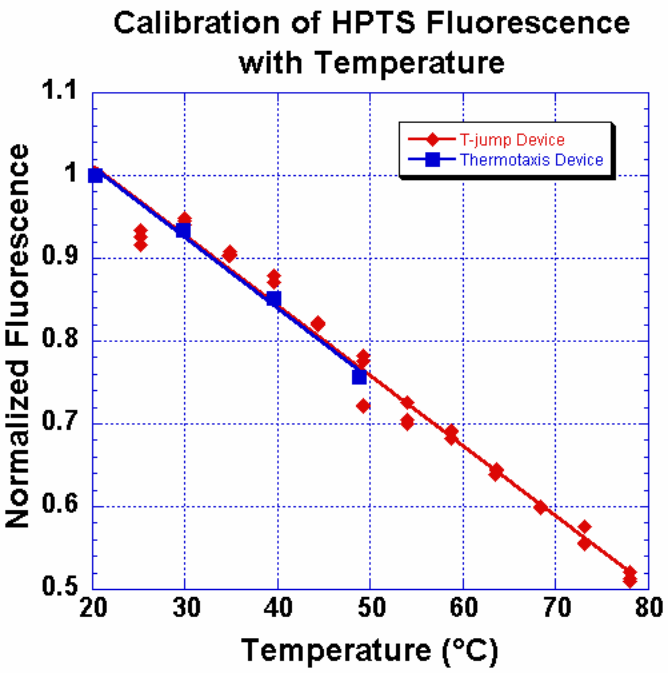

Figure 3-2: Temperature calibration of the HPTS dye. The fluorescence decreases linearly with temperature, and the plotted intensity values are normalized to the fluorescence intensity at 20 °C. The relationship is consistent between testing in two different devices.

Device Characterization

Having calibrated the ratio of HPTS fluorescence intensity with temperature, we could use the dye to characterize the temperature response of the device to the IR laser pulses. The important parameters are the transition times for heating and cooling, and the peak temperature.

First, some uncertainties associated with the IR laser heating must be considered. There is an unmeasured cooling of the sample during the dye calibration. However, the dye calibration tests were performed in two different devices, with consistent decreases in the ratio of fluorescence. Furthermore, one of these devices had the same channels as the T-jump device, and the calibration was done with the same optical components later used in the characterization of the device, all meant to reduce systematic errors from the dye calibration. A major source of uncertainty is the horizontal extent of the IR laser spot. It is only 2 μm wide, and has an area of ~50 pixels on the CCD image (using a 1x coupler and a 40x/0.95 objective). Since the laser beam is Gaussian in intensity, the center of the spot would be hotter than the edges. But, light leakage from surrounding pixels would tend to decrease the measured temperature at the center of the spot. We estimate that the uncertainty in the temperature is no more than 10%, and, this should not affect the timescale of the heating and cooling transitions. Further, during the DNA hairpin experiments on the FRET setup, the fluorescence excitation laser beam is only 300 nm wide, so

when the IR laser spot is nominally aligned to it, the temperature change is maximized in the measurement location.

On the CCD camera setup, we characterized the device with 400 nm deep observation channels and fit the heating and cooling to exponential decays. The characteristic heating time was 0.53 µs and the cooling time was 0.68 µs. The peak temperature was 92 °C (Fig. 3-3 a). We did the same on the FRET setup with 750 nm deep channels, to test our device before loading it with a biological sample. Here, the results were again as expected. The characteristic heating time was 1.9 µs and the cooling time was 1.4 µs, with a peak temperature of 96 °C (Fig. 3-3 b). As part of our characterization, we varied the IR laser power and the IR pulse duration. The characteristic heating and cooling times remained consistent in all cases (Fig. 3-3 c,d).

During our experiments with DNA hairpins, we found a very high background in the acceptor channel. The sapphire substrate has a significant fluorescence at wavelengths above ~630 nm, apparently from naturally occurring impurities, including chromium and titanium, that emit at red wavelengths when excited by blue and green light.[10] Because this fluorescence cannot be suppressed, in future experiments, an acceptor dye with fluorescence at lower wavelengths should be used in conjunction with a filter to block the sapphire's fluorescence above 630 nm. However, the sapphire does not affect the quenching behavior of the dyes

themselves, as verified with single dye controls. The background levels do not change within and outside the channels, suggesting that the sapphire simply contributes an overwhelming background signal in the red channel.

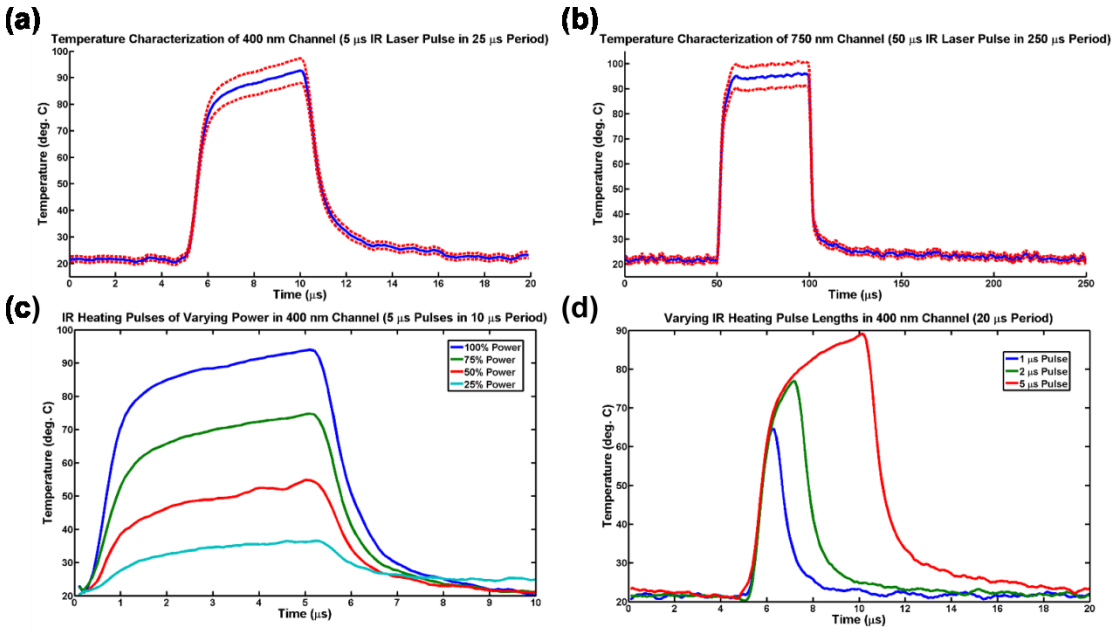

Figure 3-3: Characterization of the T-jump device with HPTS dye. (a) Heating profile in a 400 nm deep channel, with a 5 μs IR pulse in a 20 μs period. The characteristic heating and cooling times are 0.53 μs and 0.68 μs, respectively. (b) Heating profile in a 750 nm deep channel, recorded on the FRET setup, with a 50 μs IR pulse in a 250 μs period. The characteristic heating and cooling times are 1.9 μs and 1.4 μs, respectively. Both (a) and (b) display the 10% uncertainty bounds in red. (c) Heating pulses with varying IR laser power in a 400 nm deep channel. The characteristic cooling time remains invariant. (d) Heating pulses of varying duration in a 400 nm deep channel. The characteristic heating and cooling times remain invariant.

Conclusion

We have described and characterized a novel temperature jump setup that can heat and cool a sample of biomolecules in 1 µs, with temperature changes of > 50 °C. The resulting conformational changes of the biomolecules can be observed using fluorescent microscopy techniques, including FRET. To achieve high temporal resolution and fast temperature changes, we use a microfluidic device to constrain the heated volume and thermodynamic properties of the substrate to heat the sample and to rapidly dissipate heat during cooling.

3.2: Measuring DNA Hairpin Kinetics with T-jumps

Introduction

Single-stranded nucleic acids form many complex shapes, known as hairpins. Hairpins are vital for many biological processes, including transcription,[11] control of gene expression,[12] replication, and DNA recombination.[13-15] Therefore, measuring the thermodynamics of hairpin formation and stability, as well as the kinetics of folding and unfolding, would be useful for understanding these biological processes. The hairpin structure of a single sequence can vary depending on factors such as temperature, pH, and salt concentration in its environment. Moreover, the hairpin's kinetics also depend on the length and sequence of the nucleotides in the strand.[16-18] Studying how these factors affect the kinetics of hairpin folding would contribute not only to understanding hairpin conformational changes, but also the folding of more complex biomolecules.[19,20]

Many recent studies have focused on uncovering the aspects of hairpin dynamics.[16,21-36] Still, much uncertainty remains about key points, including the rates of folding and unfolding.[37,38] Moreover, there is no global model of hairpin kinetics, which would require consistent results from a wide variety of experiments, using an array of experimental techniques. Here, we describe experiments with our T-jump device that

demonstrate the utility of the apparatus, and provide data on hairpin kinetics at previously inaccessible timescales.

Temperature jumps have been used with fluorescence spectroscopy techniques to study hairpin kinetics.[22,25,35,36] However, these have a maximum T-jump of 10 °C, and non-native conditions are required for this small temperature change to induce a transition. Further, the long cooling time prevents measurements of the folding on time scales below hundreds of microseconds.[1-3] In contrast, our T-jump device permits the studying of temperature-induced folding and unfolding of DNA hairpins with large, rapid changes in both heating and cooling.

We used Förster resonance energy transfer (FRET) to measure the folding and unfolding kinetics of two different constructs: HP1, a small, 8 nucleotide-long hairpin, and HP2, a 40 nucleotide-long hairpin. Both of these showed two-state folding and unfolding, without evidence of intermediate states. HP1 had characteristic folding and unfolding times of less than 10 μs, while HP2 kinetics occur over longer times. Further, the salt dependence on the stability and the folding and unfolding rates of these hairpins agrees with the model proposed by Tan, *et al.*[34]

Materials and Methods

DNA Hairpins

Two different DNA hairpins were used in this work; Hairpin-1 (HP1) and Hairpin-2 (HP2). The sequences for HP1 and HP2 are as follows: 5'-TMR-CCTTTTGG-3', and 5'-Alexa488-AACCC-$(T)_{30}$-GGGTT-Cy5-3', respectively. All of the HPLC-grade synthetic oligonucleotides were purchased from IDT (San Diego, CA). HP1 was designed to have TMR dye on the 5' end and was used without any further modification. The purchased sequence of Hairpin-2 (HP2), contained a 5'-amino modifier (C6) and a 3'-Cy5 fluorophore. The 5' end of the DNA was labeled with Alexa488 by coupling the amino group with the N-hydroxysuccinimidylester of the dye (Alexa488-NHS ester, Molecular Probes). The labeling reaction was carried out in a freshly prepared 100 mM bicarbonate buffer (pH 8.9). The molar ratio of DNA to dye was 1:50, and the reaction mixture was incubated in the dark, overnight, at room temperature. The labeled DNA was purified from the excess dye by multiple ethanol precipitations. The absorption measurements showed more than 90% labeling efficiency. Since Alexa488 serves as the donor in the resulting FRET pair, the degree of labeling was satisfactory and no further purification steps were performed.

For the negative controls, the following DNA constructs were used: for HP1, 5'-TMR-CCTTTT; and for HP2, 5'-AminoModifierC6-AACCC-$(T)_{30}$-

GGGTT-Cy5-3' and 5'-Alexa488-AACCC-$(T)_{30}$-GGGTT-3'. The later was purchased with the 5'-amino modifier (C6) and labeled as described for HP2.

Bulk Fluorescence Measurements

Ensemble fluorescence measurements were performed in an ISS fluorimeter, equipped with a Peltier-type temperature controller. DNA concentrations of 200 nM in 10 mM phosphate buffer (pH 7.4) were used for all of the experiments. The excitation wavelengths were 547 nm for TMR, and 470 nm for Alexa488, and the fluorescence intensity was measured at 565 nm and 518 nm for HP1 and HP2, respectively, for the data analysis. To determine the melting temperatures of the hairpins, the fluorescence of the donor was monitored over a temperature range of 10 to 75 °C with 2 to 5 °C intervals, at several NaCl concentrations. The negative controls for the hairpins were subjected to identical conditions to evaluate the temperature and the salt dependence of the dye fluorescence. Subsequently, the melting data for the hairpins was corrected to remove the temperature and salt effects on the dye. The melting data was fitted by a two-state model with the midpoint of the transitions corresponding to the melting temperatures (T_m).

Fluorescence measurements in the T-jump device

To study the response of the hairpins to temperature jumps, and hence, to measure the rates of folding and unfolding, HP1 and HP2 were introduced into the microfluidic device and subjected to laser temperature jumps. For HP1, the IR heating pulse was 100 μs long, followed by an off-time of 100 μs. These were cycled 5×10^4 times, and typically 10 such runs were integrated to determine the rates. For HP2, the IR heating pulse was 400 μs, followed by an off period of either 1600 μs or 9600 μs. These were cycled 10^4 times to achieve a satisfactory signal-to-noise ratio.

Results

Conformational Fluctuations in HP1

The thermal melting profiles of HP1 (Fig. 3-4), monitored by a change in TMR fluorescence as a function of temperature, showed that the overall fluorescence change is dominated by the strong decrease in fluorescence of TMR by itself with temperature. The fluorescence of the control sequence, with a 5'-TMR but lacking the two guanosines on the 3' end (to prevent the hairpin formation), showed a cubic temperature dependence. The fitted parameters were used to estimate the actual fluorescence change due to thermal unfolding of HP1 (Fig. 3-4 inset). It should be noted that the salt dependence of the TMR fluorescence was found to be negligible under the experimental conditions used and no

corrections for salt concentration were made. Fig. 3-4 shows that HP1 unfolding can be modeled as a two-state transition with a midpoint corresponding to 38.2 °C in the presence of 100 mM NaCl. Increasing NaCl concentration to 600 mM did not change the T_m significantly, indicating that 100 mM NaCl is sufficient to screen the backbone charges during folding.

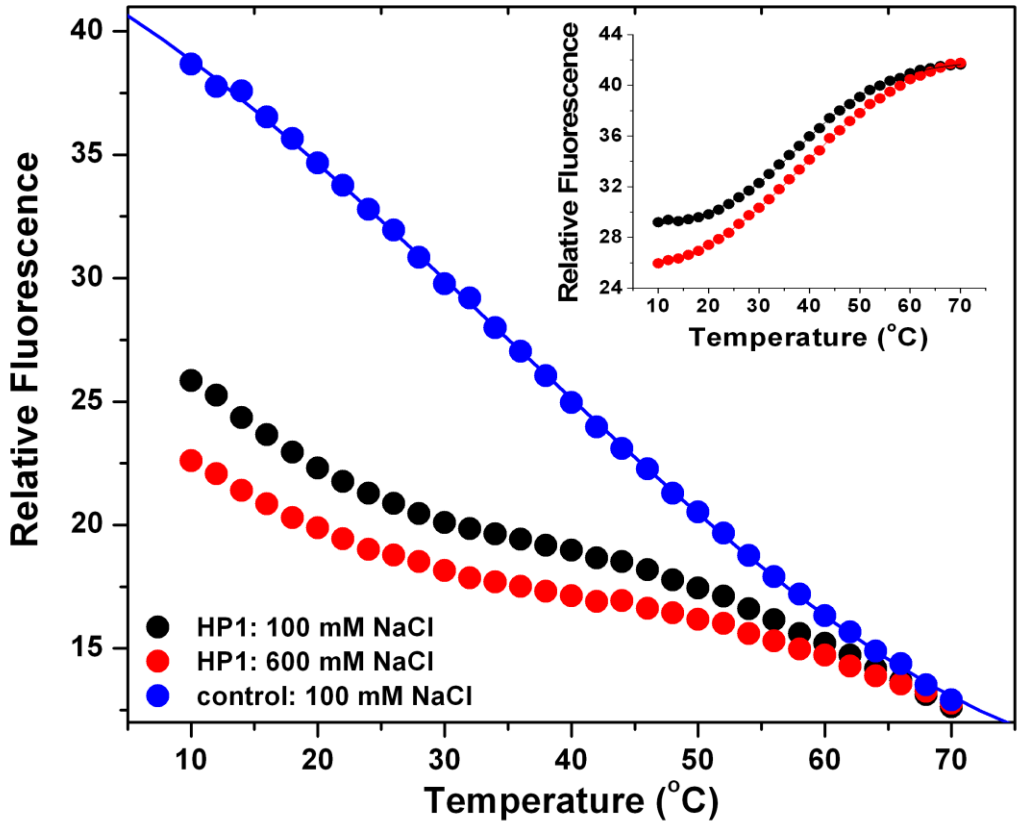

Figure 3-4: The temperature dependence of the fluorescence of HP1 in 10 mM phosphate buffer with 100 mM NaCl (black) and 600 mM NaCl (red). The blue points correspond to the dye response of the control, which was fitted with a third degree polynomial. The fitting parameters were then used to correct for the dye response to the temperature for HP1. *Inset:* The resulting melting profiles. The midpoints of the transitions were 38.2 °C for 100 mM NaCl, and 38.9 °C for 600 mM NaCl, respectively.

After establishing that HP1 has a clear conformational transition at higher temperatures, we studied the kinetics of this process using our T-jump setup. Fig. 3-5 shows the outcome of the experiment, demonstrating the utility of the device. During each cycle, the heating laser was turned on, with the sample channel experiencing a sudden jump (with a characteristic time of ~2 μs) to a high temperature (~70 °C), which was maintained for 100 μs. Then, the laser was turned off, resulting in a sudden jump (with a characteristic time of ~2 μs) back to room temperature (~22 °C), which was maintained for 100 μs. The response of the HP1 to these non-equilibrium perturbations was monitored by recording the temporal changes in the fluorescence of TMR. The HP1 control exhibited a single-exponential decay of the TMR dye fluorescence in response to the temperature jumps with a characteristic time of ~2.5 μs, which can be considered as the device response time (as in Fig. 3-3 b).

Consequently, we observed a clear decoupling of the dye response from the conformational transition of HP1 due to the temperature jump. The fluorescence of the dye decreases to a minimum value in the first 2 μs, while thermal unfolding of the HP1 accompanies an increase in the fluorescence thereafter. The inverse phenomenon was observed during cooling as well. Notably, the observed change in the absolute value of the fluorescence due to hairpin unfolding and refolding is significantly smaller than the dye response to temperature change. The weak response to

conformation changes could be due to either a low quenching efficiency of TMR by guanosine, or the equilibrium distribution of HP1 containing a much higher fraction of unfolded rather than folded hairpins. We think the latter possibility is more likely, since conformational fluctuations of similar hairpins have been studied by others[30] at room temperature, assuming spontaneous kinetics at 20 °C.

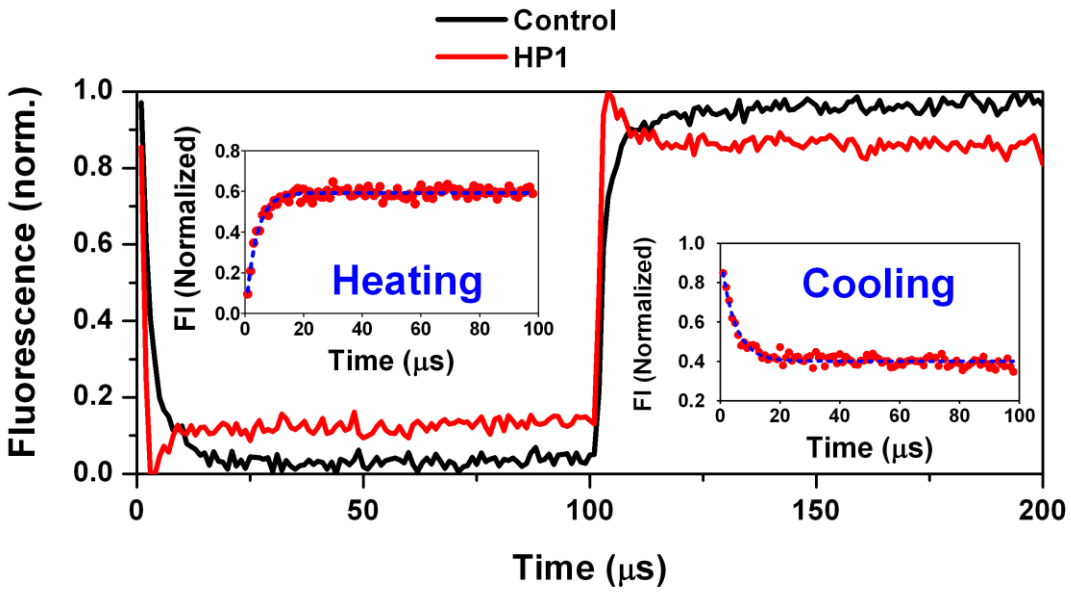

Figure 3-5: Unfolding and refolding of HP1 (red line) in 10 mM phosphate buffer containing 600 mM NaCl during rapid heating and cooling in the T-jump device. The IR laser (heating pulse) was on and off for 100 μs, respectively. The *insets* show the single exponential fits of the unfolding (left) and refolding (right) kinetics data. The black line corresponds to the dye response to the temperature change in the HP1 control under identical conditions. The characteristic decay times of the control were 2.5 μs for both heating and cooling.

The insets of Fig. 3-5 show the fitting of the observed kinetics for HP1 during unfolding and refolding. Both processes could be fitted with a

two state model, with a characteristic time of 3.7 μs for unfolding and 4.7 μs for refolding. We further explored the effect of varying the NaCl concentration on the opening and closing rates and found no significant change between 100 mM and 600 mM NaCl, in agreement with our observations of the thermal melting of HP1 under identical conditions. The data of various rates is summarized in Table 3-1.

Table 3-1: Thermal unfolding and refolding rates of HP1

[NaCl] (mM)	k_{unfold} (10^5 s^{-1})	τ_{unfold} (μs)	k_{refold} (10^5 s^{-1})	τ_{refold} (μs)
100	2.84 ± 0.16	3.5 ± 0.2	2.33 ± 0.15	4.3 ± 0.3
600	2.70 ± 0.10	3.7 ± 0.1	2.14 ± 0.15	4.7 ± 0.3

Conformational Fluctuations in HP2

Hairpin-2, representing a well-studied group of hairpins with at least five base-pairs in the stem,[16,26-28,35,36] was our second model hairpin for studying temperature-induced conformational transitions. HP2 was labeled with an Alexa488 – Cy5 FRET pair for monitoring the kinetics of folding and unfolding. Fig. 3-6 shows the temperature dependence of Alexa488 fluorescence in the Alexa488-HP2 (lacking Cy5) control at various NaCl concentrations. The dye fluorescence was best fitted with a third order polynomial, as observed for TMR in HP1. It was also noted that increased NaCl concentrations lead to a slight decrease of Alexa488

fluorescence. Similarly, the temperature dependence of the Cy5 dye in Cy5-HP2 control (lacking Alexa488) was studied at different salt concentrations and shown in Fig. 3-7 for 100 mM and 600 mM NaCl. Once again, a cubic temperature dependence was observed, but unlike Alexa488, Cy5 showed a sharp decrease in the fluorescence when temperature was increased from 25 °C to 75 °C.

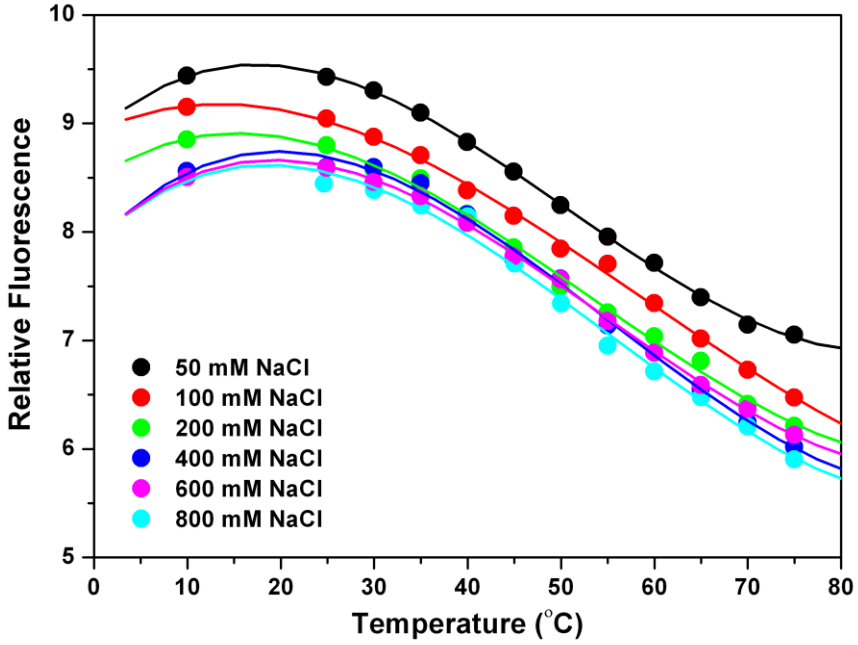

Figure 3-6: The temperature dependence of the fluorescence of A488-HP2 control in 10 mM phosphate buffer with various concentrations of NaCl. The dye response to the temperature was fitted with a third degree polynomial. The fluorescence decreases ~25% from 25 °C to 75 °C, and ~12% due to increasing NaCl from 50 mM to 800 mM.

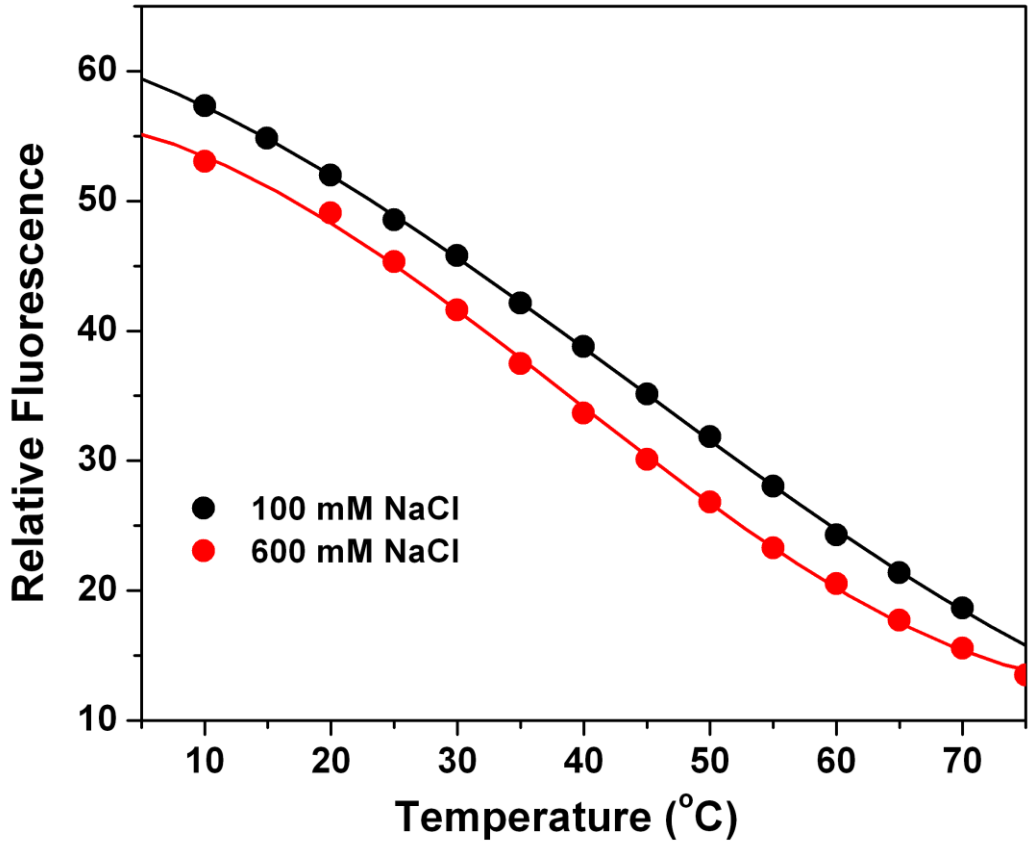

Figure 3-7: The temperature dependence of the fluorescence of Cy5-HP2 control in 10 mM phosphate buffer with various concentrations of NaCl. The dye response to the temperature was fitted with a third degree polynomial. The fluorescence decreases ~66% from 25 °C to 75 °C, and ~8% due to increasing NaCl from 100 mM to 600 mM.

Fig. 3-8 shows the thermal stability of the HP2 at various NaCl concentrations. The melting of HP2 was effectively monitored by the increase in the Alexa488 (donor) fluorescence, with a concomitant decrease in the Cy5 (acceptor) fluorescence, resulting in a net decrease of the FRET efficiency. Our data showed a FRET efficiency higher than 0.8 for the folded state of HP2, and ~0 for the unfolded state, demonstrating the

effectiveness of FRET as a tool for studying the kinetics. Since the change in donor fluorescence was sufficient to estimate the melting temperatures, we did not attempt to estimate the FRET efficiency for each temperature. Fig. 3-8 shows that the T_m was observed to increase by ~20 °C when the NaCl concentration increased from 50 mM to 800 mM.

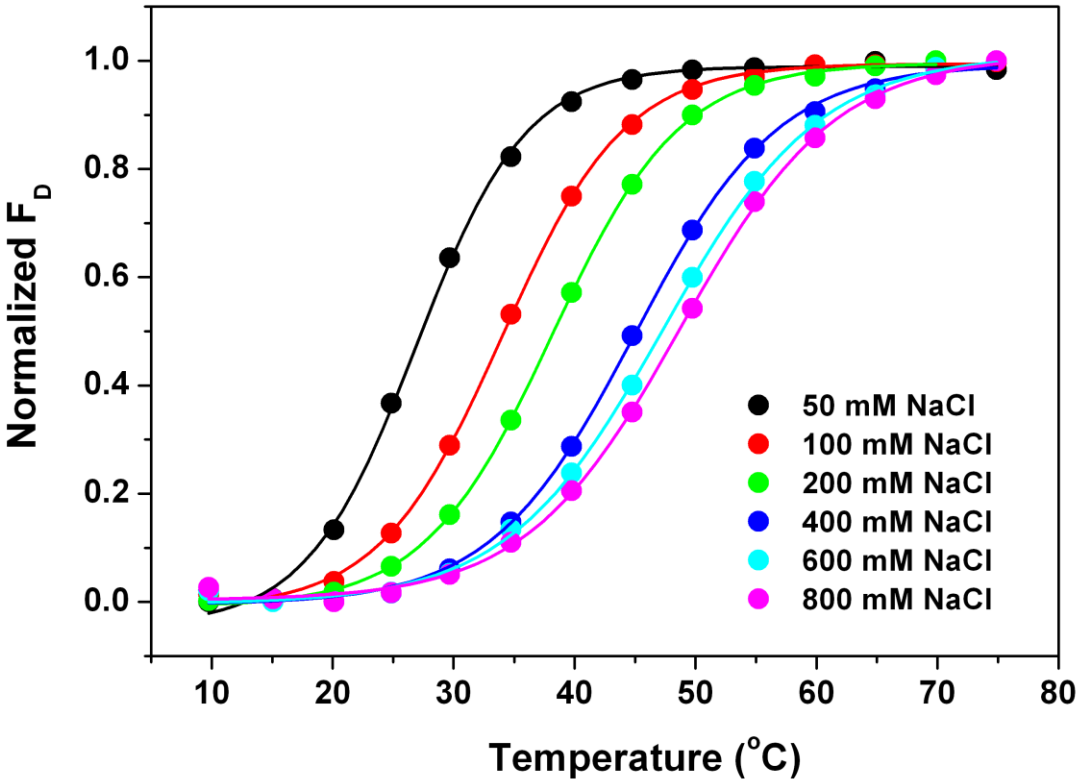

Figure 3-8: Thermal melting of HP2 as monitored by a change in the donor (Alexa488) fluorescence. The corresponding FRET efficiency (E_{FRET}) changes from 0.8 at 10 °C to ~0 at 70 °C. The fitted parameters from Fig. 3-6 were used to correct for the fluorescence change of the dye as a function of temperature.

Since, the concentration of NaCl was found to have a significant effect on the stability of HP2, we decided to study the folding and unfolding kinetics of HP2 in our T-jump device at various NaCl concentrations. A representative time-trace in the presence of 100 mM NaCl is shown in Fig. 3-9. The kinetics of HP2 unfolding were recorded during a 400 µs IR heating pulse, after an initial temperature jump from ~22 °C to ~75 °C. The refolding kinetics were monitored for the next 9600 µs by a jump back to ~22 °C, after the laser was switched off. As before, the temperature jumps had a timescale of ~2 µs (Fig. 3-10). These cycles were typically repeated 10^4 times to achieve a high signal-to-noise ratio. It is important to mention again that we observed a large fluorescence background above 630 nm when exciting with blue or green light, due to the sapphire. This background fluorescence was also found to fluctuate with temperature, thus making it difficult to estimate the real changes in Cy5 fluorescence from temperature-induced conformational fluctuations of HP2. This effect of the background signal, in addition to the strong temperature dependence of the Cy5 fluorescence, forced us to eliminate the acceptor fluorescence from further data analysis, fitting, and calculations. Hence, we used only the donor fluorescence (F_D) for our data analysis, without loss of information on the hairpin kinetics.

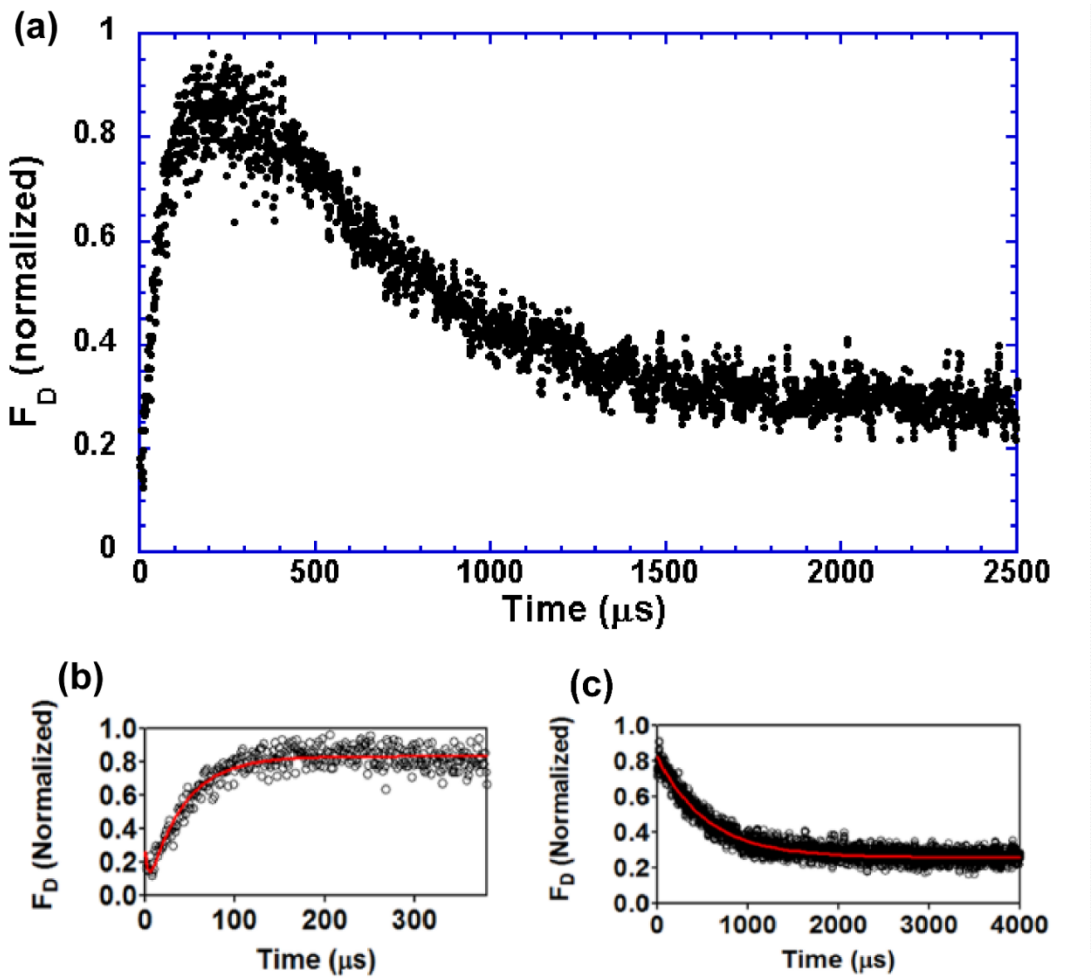

Figure 3-9: Unfolding and refolding of HP2 in 10 mM phosphate buffer containing 100 mM NaCl. The IR heating pulse was on for 400 μs to unfold the hairpin and off for 9600 μs to allow for refolding. (a) Representative time-trace for unfolding, and then refolding of HP2, shown here for 2500 μs for better clarity, (b) single exponential fitting of the unfolding kinetics, and (c) single exponential fitting of the refolding data. The fitting was performed using the data points for 9600 μs, but shown here for 4000 μs for better clarity.

Fig. 3-9 shows that both the unfolding and refolding processes can be fitted as a two state processes with no indication of intermediate species. Also, we observed Alexa488 fluorescence changes in the first few

microseconds after turning the IR laser on or off, due to changes in the dye properties with temperature (Fig. 3-10), akin to the observations of TMR in HP1. These occurred before changes in fluorescence intensity due to actual hairpin kinetics could be seen, and were in the opposite direction. We attempted to fit the unfolding and refolding kinetics with a pseudo two-step process, where the first step corresponds with the dye response to the temperature, completed in ~2 μs, and the second step corresponds to the actual hairpin kinetics, which are at least an order of magnitude slower than the dye response.

Increasing the concentration of NaCl had a dramatic effect on the refolding rate of HP2, similar to what we observed during the melting of HP2. The rate of refolding of HP2 increased almost 20 times, in a nonlinear fashion, as NaCl concentration increased from 50 mM to 800 mM. However, no obvious changes were observed in the unfolding rate. Table 3-2 summarizes the kinetic data and Fig. 3-11 shows a correlation between changes in T_m with changes in the refolding rate as a function of NaCl concentration: the more stable the hairpin (higher T_m), the faster the refolding.

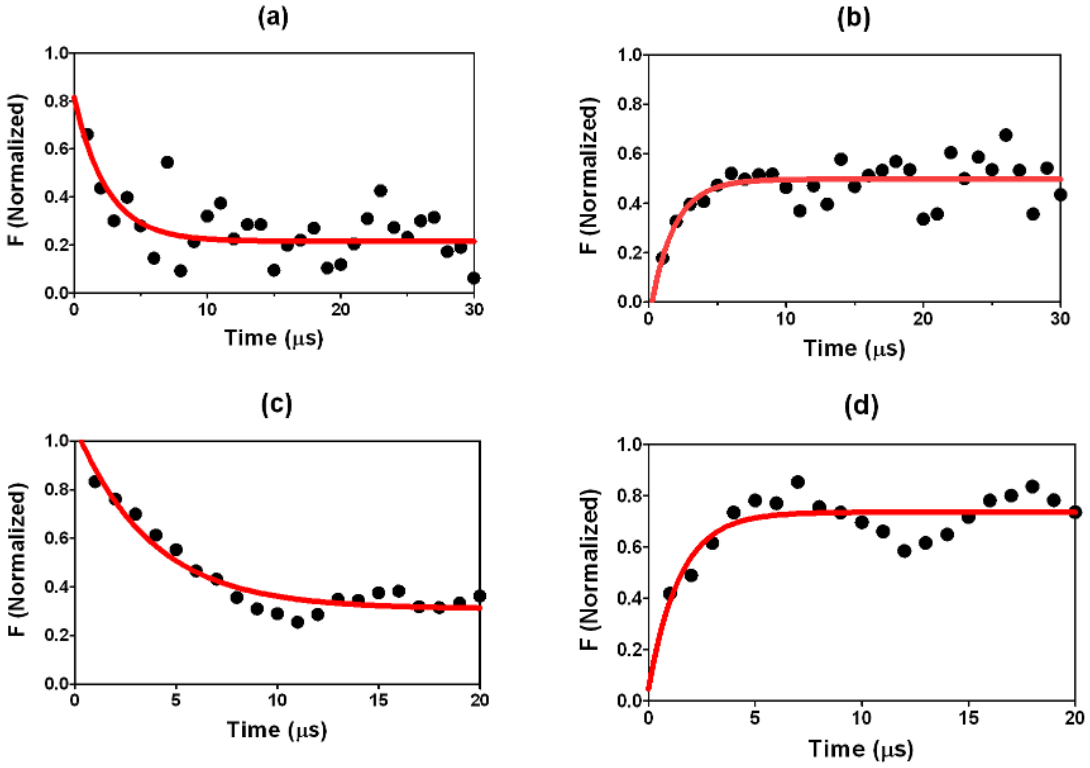

Figure 3-10: Representative dye response kinetics during T-jump of the A488-HP2 control. (a) Heating and, (b) cooling in presence of 100 mM NaCl, and (c) heating and, (d) cooling in presence of 600 mM NaCl. The NaCl concentration has little effect on the dye response over a wide range. The average observed decay time for repeated measurements in response to the heating was 2.5 μs, and that for the cooling was 1.6 μs.

Table 3-2: Thermal unfolding and refolding rates of HP2

[NaCl] (mM)	k_{unfold} (10^4 s^{-1})	τ_{unfold} (μs)	k_{refold} (10^3 s^{-1})	τ_{refold} (μs)
50	2.55 ± 0.10	39 ± 2	0.58 ± 0.03	1720 ± 90
100	2.62 ± 0.12	38 ± 2	1.87 ± 0.01	535 ± 3
200	2.71 ± 0.14	37 ± 2	3.06 ± 0.03	326 ± 3
300	2.65 ± 0.18	38 ± 3	5.01 ± 0.08	200 ± 3
450	2.88 ± 0.26	35 ± 3	6.17 ± 0.15	162 ± 4
600	2.39 ± 0.16	42 ± 3	9.18 ± 0.23	109 ± 3
800	2.82 ± 0.24	35 ± 3	10.40 ± 0.22	96 ± 2

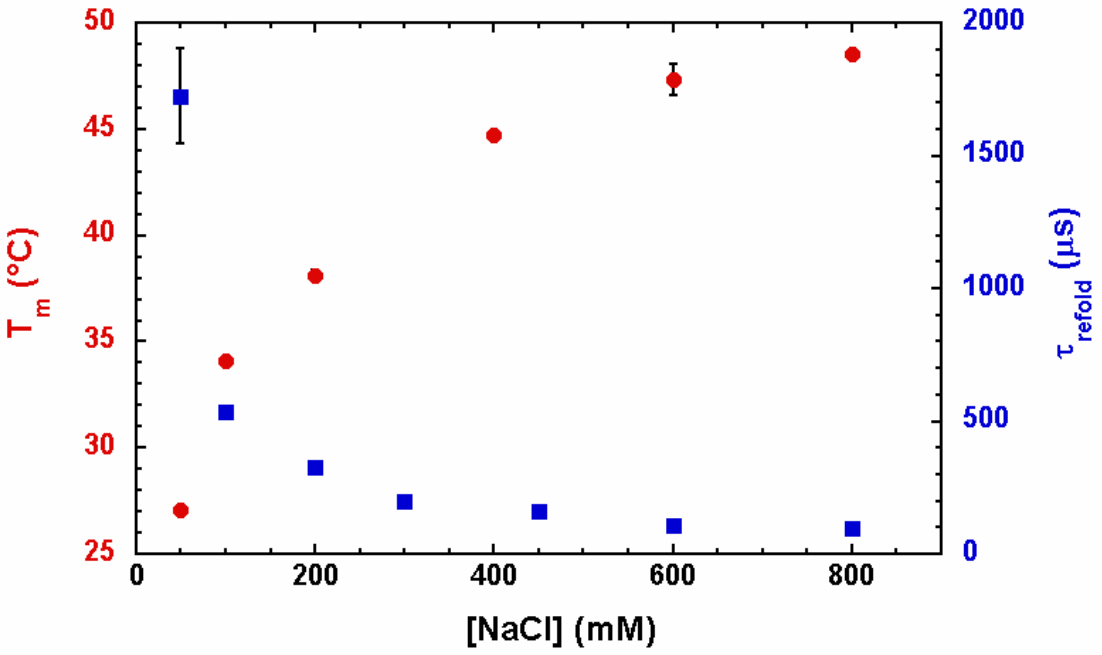

Figure 3-11: Effect of salt concentration on the stability of HP2, measured by the melting of the hairpin and its rate of refolding. *Left axis (red):* The melting temperatures, and *Right axis (blue):* The observed refolding time-scale ($1/k_{refold}$), at several NaCl concentrations. It should be noted that the unzipping rate (k_{unfold}) was observed to be insensitive to the changes in salt concentration (see Table 3-2, and the text for details).

Discussion

Several laboratories have investigated the conformational fluctuations of DNA hairpins of different stem and loop sizes, and with varying sequences, in order to understand the underlying kinetics and thermodynamics.[16,26,27,29,33,36,40] These studies most commonly explored the effects of changes in ionic strength and temperature on the folding landscapes of hairpins. Despite so many studies, there are still many open questions, and a global picture is yet to emerge, due to the lack of agreement between the experimental results and theoretical models.[21,22,24,37] Some of the studies involved laser temperature-jump methods where a jump of approximately 7 to 10 °C was achieved on a timescale of picoseconds to nanoseconds.[22,35,36] Since a jump of 10 °C is not always adequate to unfold the molecules of interest (proteins, nucleic acids) completely under physiological conditions (initial temperatures of 25 to 37 °C), a common strategy uses starting temperatures near the melting points of the biomolecules. However, this approach may have some limitations. The "cooling" of the samples to the native state cannot be achieved to study the associated kinetics if the starting conditions do not favor the native state. Further, the cooling takes hundreds of microseconds, precluding the study of the reverse processes (the molecules' refolding). As mentioned in Section 3.1, our T-jump system overcomes these limitations.

Shorter DNA hairpins, similar to HP1, were studied by Kim, *et al.*[40] and short RNA hairpins were investigated by others.[35,41] We observed that the closing is ~1 μs slower than the opening of the hairpin, both under "high" (600 mM) and "low" salt (100 mM) conditions. Also, our observed rate constants for folding and unfolding of HP1 agree with the reported value for a similar hairpin length and sequence by Kim, *et al.*[40] where they have explored the kinetics of several related short DNA hairpins using Fluorescence Correlation Spectroscopy (FCS). However, in contrast to other studies on short hairpins which indicated intermediate species in the folding pathway,[35] we observed the conformational transition to be a two-state process without any evidence of an intermediate species. It is also interesting to note that increasing NaCl concentration from 100 mM to 600 mM has very little effect both on the stability (T_m) (Fig. 3-4) and the unfolding and refolding kinetics (Table 3-1) of the hairpin. This observation is supported by the theoretical model proposed by Tan, *et al.*, suggesting that 100 mM NaCl is sufficient to screen the backbone charges, minimizing the electrostatic repulsions for a short hairpin like HP1.[34] Significantly, the observed refolding timescale of ~4 μs, which cannot be resolved by conventional T-jump methods, demonstrates the effectiveness of our T-jump device.

Hairpin-2, on the other hand, shows conformational fluctuations on a slower timescale than HP1. The observed unfolding takes place in

~38 μs, while the fastest refolding timescale of the HP2 was observed to occur in ~100 μs (in the presence of 800 mM NaCl). Unlike for HP1, a strong salt dependence on the stability, measured by the melting of the hairpin and the refolding rate, was observed for HP2, as shown in Fig. 3-11. No significant effect of the NaCl concentration on the unfolding kinetics was observed, which agrees well with the observations by Bonnet, *et al.*[16] for a hairpin similar in length and sequence. In addition, the pronounced effect of the salt concentration on the hairpin closing rates is supported by the theoretical model proposed by Tan, *et al.*[34] As with the HP1 kinetics, we did not observe any intermediate species in the folding pathway, in direct contrast with the study reported by Van Orden and co-workers,[27,29] although part of their method involved salt-induced folding and unfolding of hairpins. It is also important to note that the observed timescales for the conformational fluctuations of HP2 are similar to several previous reports,[16,22,26,27] although one suggested a slower timescale for the hairpin folding.[29]

For both HP1 and HP2, we have observed a two-state process of folding and unfolding, similar to the reports by Woodside, *et al.*[32] in their study of mechanical unfolding of DNA hairpins. Our data supports the view that the hairpin unfolding would occur through a single transition state by an input of thermal energy sufficient for crossing the energy barrier. The position of the transition state, and hence the energy barrier,

would be somewhat insensitive to the loop and stem sizes, the nucleic base sequence, and the ionic strength of the medium.[16] In our case, the insensitivity of the unfolding to the properties of the system depends on the temperature reached during heating. If the temperature is high enough to break the hydrogen bonds of the base-pairs, the hairpin will unfold. In contrast, refolding would require the two ends with complementary sequences to move into close proximity, to facilitate optimized base-pairing. Unlike in the unfolding process, we would expect the folding to have a strong dependence on the associated variables, as noted above. As proposed by Ansari and coworkers, the optimal search might result in a heterogeneous group of transient structures, the so called "ensemble transition states".[22]

Conclusion

We have built a novel T-jump setup, which helped to reveal some key aspects of both folding and unfolding of different DNA hairpins. The device combines the unprecedented capabilities of a five-fold larger jump in temperature than in previous methods with ultrafast cooling of the sample in under 2 μs. We propose that our device can be used to study the folding and unfolding of not only nucleic acids, but also proteins and polypeptides to discover the complex features of their folding landscapes.

Chapter 3, in full, is in preparation for publication as "Novel temperature jump system for studying conformation changes of biological molecules on a microsecond timescale", Polinkovsky, Mark*; Gambin, Yann*; Banerjee, Priya; Erickstad, Michael; Deniz, Ashok; and Groisman, Alex. The dissertation author is a co-first author and a leading contributor to this paper.

REFERENCES

Chapter 1

1. G. M. Whitesides, *Nature*, 2006, **442**, 368-373.

2. W. G. Lee, Y.-G. Kim, B. G. Chung, U. Demirci and A. Khademhosseini, *Advanced Drug Delivery Reviews*, 2010, **62**, 449-457.

3. Y. Gambin, V. Vandelinder, A.C.M. Ferreon, E. A. Lemke, A. Groisman and A. A. Deniz, *Nature Methods*, 2011, **8**, 239-244.

4. S. Einav, D. Gerber, P. D. Bryson, E. H. Sklan, M. Elazar, S. J. Maerkl, J. S. Glenn and S. R. Quake, *Nature Biotech,* 2008, **26**, 1019-1027.

5. N. Blow, *Nature Methods*, 2009, **6**, 683-686.

6. H. Bruus. *Theoretical Microfluidics*. New York: Oxford University Press, 2008.

7. T. C. Merkel, V. I. Bondar, K. Nagai, B. D. Freeman and I. Pinnau, *Journal Of Polymer Science Part B-Polymer Physics*, 2000, **38**, 415-434.

8. B. Herman. *Fluorescence Microscopy*. 2nd ed. Oxford: BIOS Scientific Publishers Ltd., 2001.

9. E. A. Lemke, Y. Gambin, V. Vandelinder, E. M. Brustad, H. W. Liu, P. G. Schultz, A. Groisman and A. A. Deniz. *J Am Chem Soc*, 2009, **131**, 13610-13612.

10. E. M. Brustad, E. A. Lemke, P. G. Schultz and A. A. Deniz, *J Am Chem Soc*, 2008, **130** (52):17664–5.

11. V. Vandelinder, A. C. M. Ferreon, Y. Gambin, A. A. Deniz and A. Groisman, *Anal Chem.*, 2009, **81** (16): 6929–6935.

Chapter 2

1. M. W. Covert, E. M. Knight, J. L. Reed, M. J. Herrgard and B. O. Palsson, *Nature*, 2004, **429**, 92-96.

2. E. Dekel and U. Alon, *Nature*, 2005, **436**, 588-592.

3. I. Tagkopoulos, Y. C. Liu and S. Tavazoie, *Science*, 2008, **320**, 1313-1317.

4. A. Groisman, C. Lobo, H. Cho, J. K. Campbell, Y. S. Dufour, A. M. Stevens and A. Levchenko, *Nature Meth.*, 2005, **2**, 685 - 689.

5. T. C. Merkel, V. I. Bondar, K. Nagai, B. D. Freeman and I. Pinnau, *Journal Of Polymer Science Part B-Polymer Physics*, 2000, **38**, 415-434.

6. T. Saito, C. C. Wu, H. Shiku, T. Yasukawa, M. Yokoo, T. Ito-Sasaki, H. Abe, H. Hoshi and T. Matsue, *Analyst*, 2006, **131**, 1006-1011.

7. S. M. Mitrovski and R. G. Nuzzo, *Lab On A Chip*, 2006, **6**, 353-361.

8. C. C. Wu, T. Yasukawa, H. Shiku and T. Matsue, *Sensors And Actuators B-Chemical*, 2005, **110**, 342-349.

9. M. A. Unger, H. P. Chou, T. Thorsen, A. Scherer and S. R. Quake, *Science*, 2000, **288**, 113-116.

10. A. P. Vollmer, R. F. Probstein, R. Gilbert and T. Thorsen, *Lab On A Chip*, 2005, **5**, 1059-1066.

11. E. Leclerc, Y. Sakai and T. Fujii, *Biotechnology Progress*, 2004, **20**, 750-755.

12. D. Sud, G. Mehta, K. Mehta, J. Linderman, S. Takayama and M. A. Mycek, *Journal Of Biomedical Optics*, 2006, **11**.

13. G. Mehta, K. Mehta, D. Sud, J. W. Song, T. Bersano-Begey, N. Futai, Y. S. Heo, M. A. Mycek, J. J. Linderman and S. Takayama, *Biomedical Microdevices*, 2007, **9**, 123-134.

14. J. M. Gray, D. S. Karow, H. Lu, A. J. Chang, J. S. Chang, R. E. Ellis, M. A. Marletta and C. I. Bargmann, *Nature*, 2004, **430**, 317-322.

15. S. K. W. Dertinger, D. T. Chiu, N. L. Jeon and G. M. Whitesides, *Analytical Chemistry*, 2001, **73**, 1240-1246.

16. K. Campbell and A. Groisman, *Lab on a Chip*, 2007, **7**, 264-272.

17. P. J. Hung, P. J. Lee, P. Sabounchi, R. Lin and L. P. Lee, *Biotechnology and Bioengineering*, 2005, **89**, 1-8.

18. N. L. Jeon, H. Baskaran, S. K. W. Dertinger, G. M. Whitesides, L. Van de Water and M. Toner, *Nature Biotechnology*, 2002, **20**, 826-830.

19. P. Herzmark, K. Campbell, F. Wang, K. Wong, H. El-Samad, A. Groisman and H. R. Bourne, *PNAS*, 2007, **104**, 13349-13354.

20. J. O. Hirschfelder, R. B. Bird and E. L. Spotz, *Chemical Reviews*, 1949, **44**, 205-231.

21. H. J. Cho, H. Jonsson, K. Campbell, P. Melke, J. W. Williams, B. Jedynak, A. M. Stevens, A. Groisman and A. Levchenko, *PLoS Biology*, 2007, **5**, 2614-2623.

22. J. B. Andersen, A. Heydorn, M. Hentzer, L. Eberl, O. Geisenberger, B. B. Christensen, S. Molin and M. Givskov, *Applied And Environmental Microbiology*, 2001, **67**, 575-585.

23. J. de Jong, P. W. Verheijden, R. G. H. Lammertink and M. Wessling, *Analytical Chemistry*, 2008, **80**, 3190-3197.

24. C. Merlin, M. Masters, S. McAteer and A. Coulson, *Journal Of Bacteriology*, 2003, **185**, 6415-6424.

25. G. L. Wang, B. H. Jiang, E. A. Rue and G. L. Semenza, *PNAS*, 1995, **92**, 5510-5514.

26. M. Polinkovsky, E. Gutierrez, A. Levchenko and A. Groisman, *Lab On A Chip*, 2009, **9**, 1073-1084.

27. K. Campbell, Y. Fainman and A. Groisman, *Applied Physics Letters*, 2007, **91**.

28. G. L. Semenza, *Current Opinion In Cell Biology*, 2001, **13**, 167-171.

29. P. Carmeliet, Y. Dor, J. M. Herbert, D. Fukumura, K. Brusselmans, M. Dewerchin, M. Neeman, F. Bono, R. Abramovitch, P. Maxwell, C. J. Koch, P. Ratcliffe, L. Moons, R. K. Jain, D. Collen and E. Keshet, *Nature*, 1998, **394**, 485-490.

30. K. J. Banasiak and G. G. Haddad, *Brain Research*, 1998, **797**, 295-304.

31. J. A. Dempsey, S. C. Veasey, B. J. Morgan and C. P. O'Donnell, *Physiological Reviews*, 2010, **90**, 47-112.

32. A. Mohyeldin, T. Garzon-Muvdi and A. Quinones-Hinojosa, *Cell Stem Cell*, 2010, **7**, 150-161.

33. C. B. Allen, B. K. Schneider and C. W. White, *American Journal Of Physiology-Lung Cellular And Molecular Physiology*, 2001, **281**, L1021-L1027.

34. S. G. Lynn, J. J. LaPres and K. Studer-Rabeler, *Genetic Engineering & Biotechnology News*, 2011, **31**, 52-53.

35. J. W. Allen and S. N. Bhatia, *Biotechnology and Bioengineering*, 2003, **82**, 253-262.

36. A. P. Vollmer, R. F. Probstein, R. Gilbert and T. Thorsen, *Lab On A Chip*, 2005, **5**, 1059-1066.

37. R. H. W. Lam, M.-C. Kim and T. Thorsen, *Analytical Chemistry*, 2009, **81**, 5918-5924.

38. J. F. Lo, E. Sinkala and D. T. Eddington, *Lab On A Chip*, 2010, **10**, 2394-2401.

39. J. S. Mohammed, Y. Wang, T. A. Harvat, J. Oberholzer and D. T. Eddington, *Lab On A Chip*, 2009, **9**, 97-106.

40. S. C. Oppegard, K. H. Nam, J. R. Carr, S. C. Skaalure and D. T. Eddington, *PLoS One*, 2009, **4**.

41. M. Adler, M. Polinkovsky, E. Gutierrez and A. Groisman, *Lab On A Chip*, 2010, **10**, 388-391.

42. K. Kalischewski and K. Schugerl. *Colloid and Polymer Science*, 1979, **257**, 1099-1110.

43. L. K. Massey, *Permeability Properties of Plastics and Elastomers,* 2nd Ed., William Andrew Publishing, 2003.

44. E. Metzen, M. Wolff, J. Fandrey and W. Jelkmann, *Respiration Physiology*, 1995, **100**, 101-106.

45. E. Metzen and P. J. Ratcliffe, *Biological Chemistry*, 2004, **385**, 223-230.

46. E. Berra, G. Pages, and J. Pouyssegur, *Cancer and Metastasis Reviews*, 2000, **19**, 139-145.

47. D. J. Pinsky, H. Liao, C. A. Lawson, S. F. Yan, J. Chen, P. Carmeliet, D. J. Loskutoff and D. M. Stern, *Journal Of Clinical Investigation*, 1998, **102**, 919-928.

48. Y. Q. Wang, Z. Y. Tang, R. Y. Xue, G. K. Singh, W. Q. Liu, Y. G. Lv and L. Yang, *Molecular And Cellular Biochemistry*, 2012, **360**, 235-242.

49. M. Hollborn, C. Stathopoulos, A. Steffen, P. Wiedemann, L. Kohen and A. Bringmann, *Investigative Ophthalmology & Visual Science*, 2007, **48**, 4360-4367.

50. M. D. Sternlicht and Z. Werb, *Annual Review Of Cell And Developmental Biology*, 2001, **17**, 463-516.

51. Y. S. Shin, K. Cho, S. H. Lim, S. Chung, S. J. Park, C. Chung, D. C. Han and J. K. Chang, *Journal of Micromechanics And Microengineering*, 2003, **13**, 768-774.

Chapter 3

1. J. Kubelka, *Photochem. Photobiol. Sci.*, 2009, **8**, 499–512.

2. M. Sadqi, L. J. Lapidus and V. Muñoz, *PNAS*, 2003, **100** (21), 12117–12122.

3. R. M. Ballew, J. Sabelko, C. Reiner and M. Gruebele, *Rev. Sci. Instrum.*, 1996, **67** (10), 3694-3699.

4. B. Nölting, R. Golbik, J. L. Neira, A. S. Soler-Gonzalez, G. Schreiber and A. R. Fersht, *PNAS*, 1997, **94**, 826-830.

5. J. Sabelko, J. Ervin and M. Gruebele, *PNAS*, 1999, **96**, 6031-6036.

6. *CRC Handbook of Chemistry and Physics,* 81st Ed.; CRC Press, LLC: New York, 2001.

7. Y. Gambin, V. VanDelinder, A. C. M. Ferreon, E. A. Lemke, A. Groisman and A. A. Deniz, *Nature Methods*, 2011, **8** (3), 239-241.

8. Z. Zhujun and W. R. Seitz, *Analytica Chimica Ada*, 1984, **160**, 47-55.

9. M. J. Erickstad, L. Tadrist and A. Groisman, *Biophysical Journal*, 2012, **102** (3), 151a.

10. C. S. Venkateswaran, *Proceedings Mathematical Sciences*, 1935, **2** (5), 459-465.

11. M. A. Glucksmann-Kuis, X. Dai, P. Markiewicz and L. B. Rothman-Denes, *Cell*, 1996, **84**, 147-154.

12. E. Zazopoulos, E. Lalli, D. M. Stocco and P. Sassone-Corsi, *Nature*, 1997, **390**, 311-315.

13. S. J. Froelich-Ammon, K. C. Gale and N. Osheroff, *J Biol Chem*, 1994, **269**, 7719-7725.

14. G. Varani, *Annu Rev Biophys Biomol Struct*, 1995, **24**, 379-404.

15. M. Gellert, *Annu Rev Biochem*, 2002, **71**, 101-132.

16. G. Bonnet, O. Krichevsky and A. Libchaber, *PNAS*, 1998, **95**, 8602-8606.

17. J. Volker, N. Makube, G. E. Plum, H. H. Klump and K. J. Breslauer, *PNAS*, 2002, **99**, 14700-14705.

18. M. I. Wallace, L. Ying, S. Balasubramanian and D. Klenerman, *PNAS*, 2001, **98**, 5584-5589.

19. P. C. Bevilacqua and J. M. Blose, *Annu Rev Phys Chem*, 2008, **59**, 79-103.

20. S. J. Chen, *Annu Rev Biophys*, 2008, **37**, 197-214.

21. N. L. Goddard, G. Bonnet, O. Krichevsky and A. Libchaber, *Phys Rev Lett*, 2000, **85**, 2400-2403.

22. A. Ansari, S. V. Kuznetsov and Y. Shen, *PNAS*, 2001, **98**, 7771-7776.

23. S. V. Kuznetsov, C. C. Ren, S. A. Woodson, and A. Ansari, *Nucleic Acids Res*, 2008, **36**, 1098-1112.

24. S. V. Kuznetsov, Y. Shen, A. S. Benight and A. Ansari, *Biophys J*, 2001, **81**, 2864-2875.

25. Y. Q. Shen, S. V. Kuznetsov and A. Ansari, *Biophys J*, 2001, **80**, 481a.

26. J. Jung, R. Ihly, E. Scott, M. Yu and A. Van Orden, *J Phys Chem B*, 2008, **112**, 127-133.

27. J. Jung and A. Van Orden, *J Am Chem Soc*, 2006, **128**, 1240-1249.

28. J. Jung and A. Van Orden, *J Phys Chem B*, 2005, **109**, 3648-3657.

29. R. K. Nayak, O. B. Peersen, K. B. Hall and A. Van Orden, *J Am Chem Soc*, 2012, **134**, 2453-2456.

30. A. Van Orden and J. Jung, *Biopolymers*, 2008, **89**, 1-16.

31. M. T. Woodside, P. C. Anthony, W. M. Behnke-Parks, K. Larizadeh, D. Herschlag and S. M. Block, *Science*, 2006, **314**, 1001-1004.

32. M. T. Woodside, W. M. Behnke-Parks, K. Larizadeh, K. Travers, D. Herschlag and S. M. Block, *PNAS*, 2006, **103**, 6190-6195.

33. J. R. Grunwell, J. L. Glass, T. D. Lacoste, A. A. Deniz, D. S. Chemla and P. G. Schultz, *J Am Chem Soc*, 2001, **123**, 4295-4303.

34. Z. J. Tan and S. J. Chen, *Biophys J*, 2008, **95**, 738-752.

35. H. Ma, D. J. Proctor, E. Kierzek, R. Kierzek, P. C. Bevilacqua and M. Gruebele, *J Am Chem Soc*, 2006, **128**, 1523-1530.

36. H. Ma, C. Wan, A. Wu and A. H. Zewail, *PNAS*, 2007, **104**, 712-716.

37. A. Ansari, Y. Shen and S. V. Kuznetsov, *Phys Rev Lett*, 2002, **88**, 069801.

38. E. J. Sorin, M. A. Engelhardt, D. Herschlag and V. S. Pande, *J Mol Biol*, 2002, **317**, 493-506.

39. T. Heinlein, J. P. Knemeyer, O. Piestert and M. Sauer, *Journal of Physical Chemistry B*, 2003, **107**, 7957-7964.

40. J. Kim, S. Doose, H. Neuweiler and M. Sauer, *Nucleic Acids Res*, 2006, **34**, 2516-2527 (2006).

41. I. Hirao, G. Kawai, S. Yoshizawa, Y. Nishimura, Y. Ishido, K. Watanabe and K. Miura, *Nucleic Acids Res*, 1994, **22**, 576-582.